ABSTRACT

Title of Dissertation: QUANTIFYING THE EMISSIONS OF CARBON DIOXIDE (CO_2), CARBON MONOXIDE (CO), AND NITROGEN OXIDES (NO_x) FROM HUMAN ACTIVITIES: TOP-DOWN AND BOTTOM-UP APPROACHES

Doyeon Ahn, Doctor of Philosophy, 2021

Dissertation directed by: Professor Ross J. Salawitch, Department of Chemistry and Biochemistry, Department of Atmospheric and Oceanic Science, Earth System Science Interdisciplinary Center

Professor Russell R. Dickerson, Department of Atmospheric and Oceanic Science

This dissertation encompasses three projects that quantify the emissions of greenhouse gases and air pollutants from human activities. In the first project, we use the aircraft-based mass balance (MB) approach to quantify the emission of CO_2 from the Baltimore, MD-Washington, D.C. (Balt-Wash) area during winter 2015. Based on analysis of aircraft observations using the MB-based top-down approach, we estimate the emission of 1.9 ± 0.3 million metric tons (MtC) of CO_2 due to the combustion of fossil fuels ($FFCO_2$) from the Balt-Wash region February 2015. Our value is 14% lower than the 2.2 ± 0.3 MtC mean estimate of $FFCO_2$ from four bottom-up inventories often used to drive climate policy.

In the second project, we investigate the declines in the emissions of CO_2 and CO from the Balt-Wash area during the COVID-19 pandemic. We estimate using the MB approach applied to aircraft data that the emission of CO_2 and CO declined by 29–32% and by 27–37%, respectively, from February 2020 (prior to COVID-19 lockdowns) to April – May 2020 (in the midst of COVID-19 pandemic). We show that for February 2020, two bottom-up emission inventories (EDGARv50 and the state of Maryland inventory) underestimate CO_2 emissions by 13–18%, whereas two bottom-up inventories (EDGARv50 and NEI2017) overestimate the emission of CO by 54–66%. We show that the major contributor to the overestimation of the emission of CO in the bottom-up inventory is due to the mobile (i.e., cars and trucks) sector.

The third project examines the emissions of CO_2 and NO_x from the U.S. power sector. We quantify reductions in the emissions due to the direct impact of COVID-19 and changes in the fuel-mix profile during 2015-2020 (i.e., switching from coal to natural gas). For the contiguous U.S., we estimate the impact of COVID-19 in April 2020 to be a decline of 18 ±4% on the emission of CO_2 and of 22 ± 5% on the emission of NO_x. For the same month, we estimate the impact of the fuel-mix transition to be declines of 26% on the emission of CO_2 and 42% on the emission of NO_x.

QUANTIFYING THE EMISSIONS OF CARBON DIOXIDE (CO_2), CARBON MONOXIDE (CO), AND NITROGEN OXIDES (NO_x) FROM HUMAN ACTIVITIES: TOP-DOWN AND BOTTOM-UP APPROACHES

by

Doyeon Ahn

Dissertation submitted to the Faculty of the Graduate School of the
University of Maryland, College Park, in partial fulfillment
of the requirements for the degree of
Doctor of Philosophy
2021

Advisory Committee:
Professor Ross J. Salawitch, Chair
Professor Russell R. Dickerson, Co-chair
Professor Akua Asa-Awuku, Dean's representative
Dr. Xinrong Ren
Professor Neil V. Blough
Professor Alice C. Mignerey

Dedication

To my grandfather, 안중길 (Jung-gil Ahn, 1931 – 2018), who passed away while I was pursuing a PhD degree in the U.S.

Acknowledgements

This body of work results from the collaborative efforts of the Atmospheric Chemistry group members at the University of Maryland.

I would like to thank my advisors, Dr. Ross Salawitch and Dr. Russell Dickerson, for giving me guidance and resources to help me grow as a scientist. They accepted me when I had contacted them with a passion for the research while lacking expertise in the field. I would like to thank Dr. Xinrong Ren for his willingness to share valuable datasets. I acknowledge that most of the work presented in this dissertation would not have been possible without the data you collected. I am thankful to Dr. Timothy Canty and Dr. Hao He for providing me scientific guidance and comments throughout the years. I would like to thank Jeffrey Henrikson for helping me out whenever I had technical issues.

I am thankful to the members of the atmospheric chemistry group, Allison Ring, Daniel Anderson, Daniel Goldberg, Julie Nicely, Austin Hope, Pamela Wales, Margaret Marvin, Courtney Grimes, Sayatan Sahu, Walter Tribett, Sandra Roberts, Dolly Hall, Brian Bennett, Sarah Benish, Phil Stratton, and Laura McBride. They were supportive colleagues and good friends throughout the years.

I would like to thank my parents, Jinchul Ahn, Minyoung Cha, and my brother, Jaeyeon Ahn, for supporting me while I was pursuing PhD degree far away from home. I sincerely appreciate the sacrifices that my family made throughout the years. I am thankful to Suyoung Bae, who went through many ups and downs with me while both of us were pursuing PhD degrees.

I would like to acknowledge the support from the National Institute of Standards and Technology (NIST) and the Maryland Department of the Environment (MDE). The Fluxes of Greenhouse Gases in Maryland (FLAGG-MD) project was funded and supported by NIST's Greenhouse Gas Measurements program. I appreciate the helpful comments provided by Joel Dreessen at MDE and Anna Karion and Israel Lopez-Coto at NIST on my research throughout the years.

Table of Contents

List of Figures

List of Tables

List of Abbreviations

ACES	Anthropogenic Carbon Emissions System
BAU	Business As Usual
CDD	Cooling Degree Days
CEMS	Continuous Emissions Monitoring System
CPC	Climate Protection Center
CRDS	Cavity Ring-Down Spectroscopy
DOEE	Department of Energy and Environment
EDGAR	The Emissions Database for Global Atmospheric Research
EIA	Energy Information Administration
EPA	Environmental Protection Agency
FLAGG-MD	Fluxes of Atmospheric Greenhouse-Gases in Maryland
$FFCO_2$	Fossil Fuel CO_2
FFDAS	Fossil Fuel Data Assimilation System
GHG	Greenhouse Gas
GPP	Gross Primary Productivity
HDD	Heating Degree Days
HRRR	High-Resolution Rapid Refresh
HYSPLIT	Hybrid Single-Particle Lagrangian Integrated Trajectory
IPCC	Intergovernmental Panel on Climate Change
INFLUX	Indianapolis Flux Experiment
ODIAC	Open-Source Data Inventory for Anthropogenic CO_2
MAPE	Mean Absolute Percentage Error
MARS	Multivariate Adoptive Regression Splines
MDE	Maryland Department of the Environment
MDOT	Maryland Department of Transportation
MOVES	MOtor Vehicle Emission Simulator
MPE	Mean Percentage Error
NAM	North American Mesoscale Forecast System
NDVI	Normalized Difference Vegetation Index
NEI	National Emissions Inventory
NIST	National Institute for Standards and Technology
NOAA	National Oceanic and Atmospheric Administration
OCO-2	Orbiting Carbon Observatory 2
OMI	Ozone Monitoring Instrument
RCI	Residential/Commercial/Industrial
RF	Research Flight
SCIAMACHY	SCanning Imaging Absorption SpectroMeter for Atmospheric CHartographY
STILT	Stochastic Time Inverted Lagrangian Transport
TROPOMI	Tropospheric Monitoring Instrument
UMD	University of Maryland
WRF-Chem	Weather Research and Forecasting (WRF) coupled with Chemistry

Chapter 1: Introduction

1.1 Background

1.1.1 Atmospheric Carbon Dioxide and Climate Change

Arrhenius (1896) provide the first quantitative description of the greenhouse effect of the atmospheric carbon dioxide (CO_2). This paper, written more than a century ago, discussed the role of CO_2 in the long-term variations of Earth's climate. Molecules of CO_2 exert the greenhouse effect with Earth's atmosphere by absorbing and emitting infrared (IR) radiation at the wavelengths around 15 μm, which lies in Earth's outgoing IR radiation range of 6 – 22 μm (Jacob, 1999). Since the industrial revolution, which began around 1860, the global CO_2 emissions from burning of fossil fuels have rapidly increased (Keeling, 1973; Tribett et al., 2017).

In 2020, the annual mean dry-air mole fraction of CO_2 measured at the Mauna Loa site was 414.24 ppm, which is 98.26 ppm larger than the value measured in 1959 (315.98 ppm) (Tans & Keeling, 2021). This rapid increase in the atmospheric abundance of CO_2 induced a rise of global mean surface temperature of about 1°C over the past century (Salawitch et al., 2017). Among the major greenhouse gases (GHGs), atmospheric CO_2 was the largest contributor to the total radiative forcing of climate (RF), accounting for 61% of the increase in RF from 1990 to 2019 (NOAA, 2020b). A large number of studies have reported the detrimental impact of global warming and resulting climate change on Earth's ecosystem (Stocker et al., 2013). On 12 December 2015, a total of 196 state-parties (i.e., countries adhered to the UNESCO World

Heritage Convention) adopted the Paris Climate Agreement, by consensus, to reduce GHG emissions "as soon as possible" and to do their best to keep global warming well below 2°C (UNFCCC, 2015).

1.1.2 Greenhouse Gas Emissions from Cities

Cities are major contributors to the global emission of GHGs. Cities consume about 70% of global energy, while they occupy only 2% of Earth's surface (O'Shaughnessy et al., 2016). As a result of this large energy consumption in the world's cities, which is generally accompanied by the burning of fossil-fuels, cities contribute more than 70% of the global energy-related emissions of GHGs (UN-Habitat, 2011). For most countries in the world, the top three largest urban areas contribute more than 25% of their national total carbon footprint (Moran et al., 2018). The importance of urban GHG emissions is projected to increase in the future. By 2050, about 68% of the world population is projected to live in cities, a 13% increase from the 2015 level of 55% of total population (UN, 2018).

With the increasing awareness of the importance of urban emissions of GHGs, cities and local governments have been taking actions to reduce their emissions. As of 2020, a total of 88 cities around the globe have joined the C40 Cities Climate Leadership Group (C40) and pledged to take climate actions and reduce their emissions of GHGs (C40, 2020). In the United States (U.S.), as of 9 March 2021, at least 16 states plus Puerto Rico have enacted legislation to set requirements for reducing state-wide emissions of GHGs (NCSL, 2021). Many of these states have not only set reduction targets, but have also implemented mandatory reporting requirements. For example,

the state of Maryland has set a GHG reduction target of 50% below 2006 levels by 2030 (MDE, 2021). Also, the Maryland Department of Environment is required to publish a statewide GHG emissions inventory every three years, starting 2011. Washington, D.C. has set the reduction target of 50% below 2006 levels by 2032 and has plans to reach net-zero emissions of GHGs by 2050 (DOEE, 2018).

1.1.3 Quantifying Greenhouse Gas Emissions: The Bottom-up Approach

Many states and cities that have set the GHG emission reduction targets rely on self-generated bottom-up emission inventories to track progress and evaluate the efficacy of their climate policies and regulations (Gurney et al., 2021). In the context of quantifying GHG emissions, the bottom-up approach refers to accounting methodologies that utilize both activity metric data and corresponding emission factors for various source sectors (Liu et al., 2020). For example, the state of Maryland GHG inventory calculates the on-road transportation sector emissions of CO_2 by multiplying fuel consumption data (i.e., gasoline, diesel, compressed natural gas, ethanol) with various emission factors (i.e., the amount of CO_2 emitted per unit consumption of each fuel) (MDE, 2017).

The emission factors are the key components to develop reliable bottom-up emission inventories. The accuracy of emission factors for various source sectors has been evaluated in previous studies. McDonald et al. (2018) found that on-road gasoline emission factors in the EPA's MOtor Vehicle Emission Simulator (MOVES) model are 2.5 times greater for carbon monoxide (CO) emissions in comparison to a emission factor determined from near-roadway measurements. Gately et al. (2015) reported that the Emissions Database for Global Atmospheric Research (EDGAR) model uses a

single emission factor (i.e. emissions per km) for both low-traffic and high-traffic road, inducing geographical allocation errors for the CO_2 emission estimates. Anderson et al. (2014) analyzed aircraft data obtained over the Baltimore Washington region and found that the national emissions inventory (NEI) overestimates mobile NO_x emissions by 51-70%. This study suggested that the MOVES model's inaccurate treatment of vehicle ages and corresponding NO_x emission factors could be a potential source of the model-observation discrepancy. Hall et al. (2020) found that the sensitivity of vehicular NO_x emissions to the outdoor temperature is significantly underpredicted in the EPA's MOVES model, in comparison to the estimate from the ambient measurements at the I-95 highway near-road site. Yu et al. (2021) used a deep learning approach to predict NO_x emissions from diesel vehicles, and showed improved prediction performance relative to seven other models used in the study. Zhao et al. (2011) found that a single emission factor is applied for almost the entire industrial sector, regardless of combustion technology or fuel type, in the China's national emission inventory, which leads to a large uncertainty in the estimated emissions. Recently, Solazzo et al. (2021) estimated the complete structural uncertainty for the EDGAR emission inventory, by propagating uncertainties associated with individual activity data and emission factors.

Reliable activity data are also important components of the bottom-up emissions inventory. Guan et al. (2012) calculated two sets of China's annual CO_2 emissions, one from the national energy statistics data and another from the provincial energy statistics. They found that the two sets of CO_2 emissions for 2010 differ by 1.4 gigatonnes (the difference is similar to Japan's annual emissions of CO_2), while both the national and the provincial energy data are officially distributed to the public. Liu

et al. (2015) used harmonized energy consumption data and showed that the total energy consumption in China during 2000-2012 was 10% larger than the value reported by China's national statistics. Liu et al. (2015) also found that emission factors for Chinese coal are 40% lower than the default value recommended by the Intergovernmental Panel on Climate Change (IPCC). By combining updated energy statistics and emission factors, Liu et al. (2015) estimated that 2.49 gigatonnes (2σ: ±7.3%) of CO_2 were emitted from China in 2013, 14% lower than the emissions reported by other bottom-up inventories.

The bottom-up inventory cannot be completed until activity data and emission factors for specific source sectors are all available. Substantial resources are needed to collect activity data and emission factors that are differentiated by fuel type (i.e., natural gas, gasoline, diesel), technology type (i.e., gas-fired gas turbines, boilers, combined cycle), and ambient conditions (i.e., outdoor temperature, relative humidity) (EEA, 2019). Emission factors for the leakage of methane (CH_4) from various sources, such as coal mines, shale-gas wells, landfills, natural gas pipelines, and behind-the-meter home appliances, are often limited or unavailable (Alvarez et al., 2018; McKain et al., 2015; Merrin & Francisco, 2019; Plant et al., 2019; Ren et al., 2018). Furthermore, Ibarra-Espinosa & Ynoue (2016) reported that the lack of data (i.e., activity data and emission factors) is the biggest challenge to construct the bottom-up emissions inventory for South American cities. The process of data collection (i.e., activity metric and emission factors), data processing (i.e., aggregating data by source sector categories), and evaluation (i.e., comparison to estimates from atmospheric

observations) should be conducted with transparency to develop reliable bottom-up emission inventories for policy makers and stakeholders.

1.1.4 Quantifying Greenhouse Gas Emissions: The Top-down Approach

In the context of quantifying the emission of GHGs, the top-down approach refers to methodologies that utilize atmospheric observations of GHGs and atmospheric transport models. Common types of atmospheric observations used for the top-down approach include ground-tower observations (Karion et al., 2020), in-situ aircraft measurements (Ren et al., 2018), flask sampling (Turnbull et al., 2011), a network of low-cost sensors (Martin et al., 2017), and satellite remote sensing (Crisp et al., 2017). The atmospheric transport models are used to convert the atmospheric mole fraction of a GHG, measured from various platforms, to the emission flux (i.e., $kgCO_2\ km^{-2}\ hr^{-1}$) by simulating the horizontal and vertical movements of air parcels. Common type of atmospheric transport models used for the top-down method are Hybrid Single-Particle Lagrangian Integrated Trajectory (HYSPLIT) (Draxler et al., 1997; Stein et al., 2015), Stochastic Time Inverted Lagrangian Transport (STILT) (Lin et al., 2003), GEOS-Chem (Bey et al., 2001), and Weather Research and Forecasting coupled with Chemistry (WRF-Chem) (Grell et al., 2005).

The mass balance method is a conceptually simple approach that translates observed mole fractions of a GHG to emission fluxes (Trainer et al., 1995; White et al., 1983). White et al. (1983) presented a series of mathematical formula that show the horizontal flux of CO_2 downwind of an emission source is equal to the vertical flux of CO_2 over the emission source under steady wind conditions. The mass balance method relies on the principle of mass conservation with several important, implicit

assumptions: 1) a steady state wind is assumed over the geographical domain of interest, 2) there must be zero net flux through either horizontal (i.e., two sides of the box parallel to wind direction) and vertical boundaries (i.e., planetary boundary layer) of the geographical domain. Once these implicit assumptions are justified via atmospheric measurements, the mass balance method can be quickly adopted to assess the emission of GHGs from cities. A complete mathematical formula and descriptions of the mass balance method are provided in section 2.2.5. These top-down estimates can either provide flux information for cities lacking a bottom-up inventory or, as examined in this dissertation, serve as an important constraint for the accuracy of existing bottom-up inventories.

In comparison to the mass balance method, the atmospheric inversion technique is a relatively sophisticated method that relies on numerical modeling of atmospheric transport. Hypothetical observations of atmospheric CO_2 (or any other GHG) are simulated using an atmospheric transport model that disperses the prior emissions of CO_2, which are obtained from bottom-up gridded products (Kort et al., 2013). The bottom-up gridded products used for the inversion technique include the CarbonTracker (Global, 1° lat/lon resolution, (Peters et al., 2007)), EDGAR (global, 0.1°, (Janssens-Maenhout et al., 2017)), Fossil Fuel Data Assimilation System (FFDAS, global, 0.1°, (Asefi-Najafabady et al., 2014; Rayner et al., 2010)), Open-Source Data Inventory for Anthropogenic CO_2 (ODIAC, Global, 1 km, (Oda et al., 2018; Oda & Maksyutov 2011, 2015)), Anthropogenic Carbon Emissions System v1 (ACESv1, Northeast U.S., 1 km, (Gately & Hutyra, 2017, 2018)). The simulated mole fractions of atmospheric CO_2 are compared to actual mole fractions of CO_2 measured from

various platforms (i.e., ground-based towers (Mueller et al., 2018), aircraft (Lopez-Coto et al., 2020), satellites (Crowell et al., 2019; Maasakkers et al., 2021)). The cost function is defined as the sum of the difference between simulated and observed CO_2 mole fractions and the difference between prior and posterior emissions of CO_2, both weighted by the uncertainty covariance matrix (Kort et al., 2013). The optimized (posterior) CO_2 emissions are computed using a Bayesian framework to minimize the cost function (Chevallier et al., 2006).

The tracer-to-tracer ratio method is another common type of the top-down approach used to quantify GHG emissions. The tracer-to-tracer correlation slope (i.e., CH_4:CO_2, CH_4:CO, CO_2:NO_x) is often calculated from atmospheric observations of two trace gases attributed to a specific source of interest. Ren et al. (2018) multiplied the slopes of CH_4:CO and CH_4:CO_2, determined from in-situ aircraft observations by the bottom-up emission inventories (EDGAR2010 for CO and NEI2014 for CO_2) to estimate the emissions of CH_4 from the Baltimore, MD-Washington, D.C. area. Plant et al. (2019) multiplied the slopes of CH_4:CO and CH_4:CO_2, again computed from in-situ aircraft observations, by bottom-up inventories of CO and CO_2 to estimate the emission of CH_4 from numerous cities along the U.S. East Coast. Furthermore, Plant et al. (2019) used the slope of C_2H_6:CH_4 to quantify fugitive natural gas losses in the domain. Goldberg et al. (2019) estimated fossil-fuel CO_2 emissions for the major U.S. cities using the CO_2:NO_x ratio determined from bottom-up inventories. The city-specific CO_2:NO_x ratios are combined with the urban NO_x emissions estimated from column NO_2 measured by the Ozone Monitoring Instrument (OMI) instrument onboard the National Aeronautics and Space Administration (NASA)'s Aura satellite. The

tracer-to-tracer ratio method provides GHG emission estimates without having to rely on a numerical transport model or extensive statistical analysis. For reliable results of the tracer-to-tracer ratio method, the emission estimate of the trace gas in the denominator of the ratio needs to be well-established.

One of the main advantages of the top-down approach is the ability to detect previously unknown or underestimated emission hot spots. Schneising et al. (2014) used satellite remote sensing data to detect and quantify fugitive methane emissions from oil and gas production sites in the North America. Kort et al. (2014) found anomalously high CH_4 levels over the U.S. Four Corners region by analyzing column averaged CH_4 mole fractions retrieved from the SCanning Imaging Absorption SpectroMeter for Atmospheric CHartographY (SCIAMACHY) instrument onboard the European Space Agency's (ESA) Environmental Satellite (ENVISAT). Ren et al. (2018) attributed a number of CH_4 plumes observed during aircraft flights to individual landfills in Maryland using HYSPLIT back trajectories. By applying the mass balance approach to these landfill plumes Ren et al. (2018) estimated that landfill emission of CH_4 for the state of Maryland is 1.50 ± 0.80 kgCH_4/s (mean $\pm$ 1σ), a factor of two greater than the state's inventory estimate of 0.747 kgCH_4/s. Viatte et al. (2017) quantified the methane emissions from the largest dairies in the Southern California region using solar-viewing ground-based spectrometers (EM27/SUN) and carbon isotope measurements (i.e., $^{13}CH_4$ and $^{12}CH_4$) from a Cavity Ring-Down Spectroscopic (CRDS) analyzer. Their top-down estimates of the emission of CH_4 from these dairies showed a wide range of values, suggesting significant heterogeneity in the emission of CH_4 from this source.

Several limitations and challenges remain in the top-down approach. First, the accuracy and precision of the top-down emission estimate are subject to the uncertainties associated with atmospheric measurements and numerical transport modeling. One of the largest sources of uncertainty is the true value of the background mole fraction of the trace gas (Ahn et al., 2020; Cambaliza et al., 2014). The background mole fraction is defined as the mole fraction of the trace gas that would have been measured downwind of the emission source if there were no emissions from the source being quantified (Turnbull et al., 2018). For cities, this quantity is physically impossible to measure because both urban emissions and meteorological conditions over cities (i.e., wind speed, wind direction, PBL height) constantly change. Therefore, background mole fractions used to quantify urban emissions of CO_2 emissions are often determined from various proxies, such as the CO_2 mole fraction measured upwind of cities (Klausner et al., 2020), mole fractions measured at the edges of a downwind flight track (Heimburger et al., 2017), or hypothetical CO_2 mole fractions simulated using emissions of CO_2 only upwind of the source region of interest along with a numerical transport model (Lopez-Coto et al., 2020). Another important source of uncertainty is the measurement of meteorological parameters (i.e., wind speed, wind direction, planetary boundary layer height) used for atmospheric transport modeling. Ahn et al. (2020) assessed the accuracy of aircraft measurements of wind speed and wind direction by making a comparison to the North American Mesoscale Forecast System 4 km (NAM4) model estimates and wind profiler observations at the Beltsville, Maryland (see section 2.5.3). Deng et al. (2017) assimilated meteorological observations by running numerical weather prediction (NWP) model in reanalysis

mode, and reduced the mean absolute error (MAE) of wind speed (from 2.0 to 1.2 m/s), wind direction (from 26° to 14°), and PBL height by ~10%.

The source sector attributions of the observed GHG emissions are often challenging to determine using the top-down approach. In many cities, different types of emission source sectors (i.e., residential, commercial, industrial, transportation) are located in close proximity. While the urban plumes of CO_2 observed from aircraft in-situ measurements or satellite remote sensing can be attributed to specific point source (i.e., power plants, landfills, oil and natural gas wells) by running atmospheric transport models (Ahn et al., 2020; Nassar et al., 2017; Ren et al., 2018), unambiguous attribution usually requires either obtaining measurements (from aircraft) in close proximity to the source or a very large point source (for satellite observations). Jackson et al. (2014) drove a car equipped with a CRDS instrument (Picarro G2301) measuring CH_4 mole fractions across 1500 road miles over the Washington, D.C, and found total of ~5900 natural gas leaks across the city. Mitchell et al. (2018) presented public transit light-rail vehicles, equipped with instruments which measure GHGs and meteorological parameters, in the Salt Lake Valley, Utah. Continuous measurements obtained from the light-rail vehicles, traversing across the city throughout the day, provided source-specific enhancement signals of CO_2 and CH_4. These types of source sector determination from atmospheric observations are more the exception than the rule, given the laborious nature of the necessary data collection.

1.2 Outline

In this dissertation, I investigate the emissions of CO_2 from two distinct, yet related, emission sources: Cities (i.e., the Baltimore, MD-Washington, D.C.

metropolitan area) and the U.S. power sector (i.e., electricity generating units in the contiguous U.S.). Throughout this work, I analyze various types of atmospheric measurement data (i.e., aircraft measurement data, wind profiler, power plant stack monitoring) using the HYSPLIT atmospheric transport model, via the top-down mass balance method. Various statistical approaches such as regression spline models are also used. The resulting top-down emission of CO_2 estimates are compared to bottom-up estimates (i.e., state inventory, gridded bottom-up product) throughout this dissertation.

In Chapter 2, I focus on the emissions of CO_2 from the Baltimore, MD-Washington, D.C. area. I use in-situ aircraft research flight data, obtained during February 2015, and the mass balance method to quantify urban CO_2 emissions. Resulting top-down estimate of CO_2 emissions are interpreted with various models (i.e., HYSPLIT atmospheric transport model, VEGAS biogenic CO_2 model) and bottom-up estimates (i.e., state GHG inventory, bottom-up gridded product). The main goals of the Chapter 2 are:

1. Assessing the accuracy and precision of the aircraft-based mass balance method adopted to quantify CO_2 emissions from the Baltimore, MD-Washington, D.C. area.
2. Quantifying CO_2 emissions from the Baltimore, MD-Washington, D.C. area during February 2015.
3. Comparing top-down CO_2 emission estimate to various bottom-up estimates, including state GHG inventory and global/regional gridded products.

Chapter 2 was published on 14 April 2020 in the Journal of Geophysical Research - Atmospheres (Ahn et al., 2020).

In Chapter 3, I investigate the emissions of CO_2 and CO from the Baltimore, MD-Washington, D.C. area during the COVID-19 pandemic period. The aircraft-based mass balance method, presented and evaluated in Chapter 2, is applied to aircraft data obtained during the February-May 2020 period. Further, I extend the aircraft-based mass balance method by combining it with activity data for major source sectors (i.e., residential/commercial/industrial (RCI), transportation, power generation). By relating the reduced emissions of CO_2 and CO as a function of decline in major source sectors during COVID-19, top-down estimates of the CO_2 and CO emissions are attributed to specific source sectors. The main goals of Chapter 3 are:

1. Quantification of the emissions of CO_2 and CO before (i.e., February 2020) and after COVID-19 social lockdowns (i.e., April-May 2020) over the Baltimore, MD-Washington, D.C. area.
2. Source sector attributions of the emissions of CO_2 and CO from the Baltimore, MD-Washington, D.C. area (i.e., RCI, onroad transportation, off-road transportation, power generation, and others).
3. Evaluation of the bottom-up estimates for the total emissions and source sector compositions of CO_2 and CO (i.e., EDGAR, state inventory, and NEI).

The results of Chapter 3 are being prepared for journal submission, which will occur soon after the dissertation defense.

In Chapter 4, I focus on the emissions of CO_2 and NO_x from the U.S. power sector during COVID-19. I use power plant operation data for the contiguous U.S. (CONUS), publicly available from the Environmental Protection Agency (EPA) and the Energy Information Administration (EIA). The multivariate adaptive regression splines (MARS) model is adopted to estimate daily total electricity generation as a function of outdoor temperature and the type-of-day (i.e., weekdays, weekends, and holidays). The daily operation status of ~3,000 power units over the CONUS is analyzed to account for fuel-mix change (i.e., transition from coal to natural gas) seen in the U.S. power sector. The main goals of the Chapter 4 are:

1. Development and evaluation of the regression model which estimate daily total electricity generation in CONUS as a function of outdoor temperature and the type-of-day (i.e., weekdays, weekends, and holidays).
2. Quantification of the impact of COVID-19 on the U.S. power sector: electricity generation and concomitant emissions of CO_2 and NO_x.
3. Comparison of the two prominent factors affected the U.S. power sector emissions of CO_2 and NO_x: the impact of COVID-19 versus the impact of fuel-mix transition (i.e., transition from coal to natural gas).

The results of Chapter 4 are also being prepared for journal submission, which again will occur soon after the dissertation defense.

Finally, in Chapter 5 I briefly summarize the results of Chapters 2, 3, and 4. I then conclude by providing suggestions for future research.

Chapter 2: Fluxes of Atmospheric Greenhouse-Gases in Maryland (FLAGG-MD): Emissions of Carbon Dioxide in the Baltimore, MD-Washington, D.C. area

2.1 Introduction

A major increase in the atmospheric abundance of CO_2 since the industrial revolution—with significant positive perturbation to the radiative forcing of climate—has resulted in a rise of global mean surface temperature over the past century (Stocker et al., 2013). A large number of studies that clarified the detrimental impact of global warming and resulting climate change on Earth's ecosystem have spurred individual nations to mitigate greenhouse gas (GHG) emissions under the Paris Climate Agreement (Salawitch et al., 2017). Along with the efforts by most of the world's nations, the role of cities in GHG mitigation has become even more important given the recent U.S federal decision to pull back from the Paris Climate Agreement (UN, 2017). Currently, the state of Maryland is on track for reducing consumption-basis GHG emissions by 25% in 2020 and 40% in 2030 relative to emissions in 2006 (MDE, 2015). Washington, D.C. has set a plan to reduce consumption-basis GHG emissions by 50% in 2032 and by 100% in 2050 relative to 2006 emissions (DOEE, 2018).

With increasing GHG mitigation efforts, scientific research to improve the quantification and attribution of carbon sources in urban areas has become more important (Duren & Miller, 2012; Hutyra et al., 2014; Patarasuk et al., 2016).

According to UN-Habitat (2011), more than 70% of global CO_2 emissions related to energy usage comes from urban areas. Also, measuring CO_2 in urban areas is more tractable than measuring CO_2 in countries, because the CO_2 signal from cities is intense and localized (Gratani & Varone, 2005; Idso et al., 2001). Various measurement techniques, data analyses, and modeling methods have been collectively used to study CO_2 emission in urban areas. Among many U.S. cities, the Indianapolis area was chosen as one of the first testbed sites to develop and evaluate a framework to study urban GHG emissions, given its relatively simple topography and isolation from other large cities (Davis et al., 2017; Whetstone, 2018). The Indianapolis Flux Experiment (INFLUX, https://www.nist.gov/topics/greenhouse-gas-measurements/indianapolis-flux-experiment) has successfully developed and improved the mass-balance method and the inversion framework, called "Top-down" approaches, as well as inventory data-based emission models such as Hestia, a "Bottom-up" approach (Gurney et al., 2017; Lauvaux et al., 2016; Turnbull et al., 2015, 2018; Whetstone, 2018). Along with INFLUX, several projects with similar aims have been conducted in other cities. The Megacities Carbon Project was designed to quantify carbon emissions in some of the world's largest cities, including Los Angeles, Paris, and San Paulo (Bréon et al., 2015; Feng et al., 2016; Newman et al., 2016). Urban GHG emissions from the Boston area (Sargent et al., 2018) and Salt Lake City (McKain et al., 2012; Strong et al., 2011) have also been extensively investigated.

The Fluxes of Atmospheric Greenhouse-Gases in Maryland (FLAGG-MD) project is part of the National Institute for Standards and Technology (NIST) U.S. Northeast Corridor testbed which, in its first phase, is focused on the Baltimore,

Maryland (MD)-Washington, D.C. (Balt-Wash) area (Lopez-Coto et al., 2017; Mueller et al., 2018; https://www.nist.gov/topics/northeast-corridor-urban-test-bed). Taking a lead from the successful deployment of INFLUX, the FLAGG-MD project aims to understand and quantify emissions of CO_2, CH_4, and CO in the Balt-Wash area. While FLAGG-MD is similar in many ways to INFLUX, the geography of the Balt-Wash area engenders the following complications. The Balt-Wash area is part of the U.S. Northeast Corridor, which includes other major cities such as Boston, New York City, and Philadelphia. Also, the Balt-Wash area is located southeast of the Appalachian Mountains and northwest of the Chesapeake Bay, such that mesoscale circulations complicate the atmospheric transport of urban GHG emissions. Several large power plants upwind of the Balt-Wash area can episodically increase the spatiotemporal variability of the background mole fractions of CO_2. The Balt-Wash urban testbed consists mainly of aircraft campaigns conducted in collaboration with Purdue University (Lopez-Coto et al., 2020; X. Ren et al., 2018; Salmon et al., 2017, 2018), along with several other assets: installations of low cost CO_2 sensors (Martin et al., 2017), meteorological data assimilation, modeling of tower-based observations (Martin et al., 2019; Mueller et al., 2018) and incorporation of data from the Orbiting Carbon Observatory 2 (OCO-2).

In this study, emissions of CO_2 from the Balt-Wash area are quantified using the FLAGG-MD aircraft campaign dataset obtained during the month of February 2015. Section 2.2 describes the aircraft campaign, the mass balance approach, and various models used in this study. In section 2.3.1, source apportionment of the plumes of CO_2 observed by the aircraft is presented. In section 2.3.2, the impact of plume transport

from out-of-state power plants on the aircraft observations is investigated. In section 2.3.3, the accuracy and precision of the aircraft-based mass balance estimates are evaluated using the Continuous Emissions Monitoring Systems (CEMS) records of two local power plants. Section 2.3.4 discusses the uncertainty from mass balance parameters. In section 2.3.5 – 2.3.7, differences in the CO_2 emission rate among our mass balance estimate, other previously published bottom-up/downscaling model estimates, and the state of Maryland emission inventory are investigated.

2.2 Materials and Methods

2.2.1 Instrumentation

The University of Maryland (UMD) Cessna 402B aircraft was equipped with a cavity ring-down spectroscopic (CRDS) analyzer (Picarro Model G2401-m) that is used to measure the dry air mole fraction of CO_2. Measurements of CO_2 were calibrated on the ground as well as during the flight using an onboard calibration system with two cylinders of standard gases certified by National Institute of Standards and Technology (NIST). These cylinders contained CO_2 of 369.19 and 445.78 μmol mol^{-1} (parts per million, or ppm). A diaphragm pump was installed to pull the ambient air from the nose of the Cessna through a rear-facing Perfluoroalkoxy alkanes (PFA) Teflon tube (O.D=0.95 cm and I.D=0.64 cm), at a total flow rate of 10 L/min. The CRDS analyzer was connected to the main sample line via a Tee connection, allowing air to be pumped continuously through the analyzer at a rate of 400 mL/min. We tested the stability of the analyzer by sampling a tank of breathing air continuously while the aircraft climbed from 50 to 3500 m altitude – the standard deviations of CO_2 were very small, near the

measurement precision limit of the Picarro instrument. The UMD aircraft was also equipped with instruments to measure SO_2, NO_2, NO, O_3, aerosols, and meteorological variables. A more detailed description on the instrumentation can be found in Ren et al. (2018). The Purdue Duchess aircraft was equipped with a CRDS analyzer (Picarro Model G2301-m) for measurements of CO_2 and a Best Air Turbulence (BAT) probe for measurements of the three-dimensional wind field. A more detailed description of the instrumentation on the Purdue Duchess aircraft can be found in Salmon et al. (2018).

To examine the sensitivity of our mass-balance emission estimation of CO_2 emissions (described in section 2.2.5) to the measurement uncertainties, 1σ uncertainties of the temperature, pressure, and CO_2 mole fraction measurements were propagated into the mass balance equation. The 1σ absolute uncertainty of temperature measurements from both UMD and Purdue flight instruments was determined to be2.0 K, based upon a comparison of temperature measurements made from the two aircraft during a wingtip-to-wingtip flight segment conducted on 19 February 2015. For the 1σ uncertainty of the pressure measurements for the UMD flights, the reported instrument uncertainty of 0.25 hPa was used. For the Purdue flights, 1σ uncertainty was determined to be 1.6 hPa based upon a comparison of measured pressure versus calculated barometric pressure. For the 1σ uncertainty of the CO_2 measurements, the reported instrument uncertainty of 0.1 ppm was used for data collected by both the UMD and Purdue instruments.

2.2.2 Aircraft research flight design

For this study, the Balt-Wash area is defined as a rectangularly-shaped region

enclosed by the four coordinates of 38.23°N 76.67°W, 39.46°N 75.86°W, 39.87°N 77.04°W, 38.63°N 77.86°W (154×111 km^2, see Figure 2.1). The defined study area consists of populated regions, within and surrounding the cities of Baltimore, MD and Washington, D.C. The total population within the study area was 8,153,000 in year 2015 based on Gridded Population of the World (GPWv4) data (CIESIN, 2018). Seven major power plants (all within either the states of Maryland or Virginia) and a dense road network including major highways such as the Capital Beltway ring (I-495), the Baltimore Beltway (I-695), and interstate highway I-95 all lie within the study area. According to the Maryland GHG inventory, total of 18.8 MtC (Million tons Carbon) of Fossil Fuel CO_2 ($FFCO_2$) was emitted from Maryland during year 2014 (MDE, 2016).

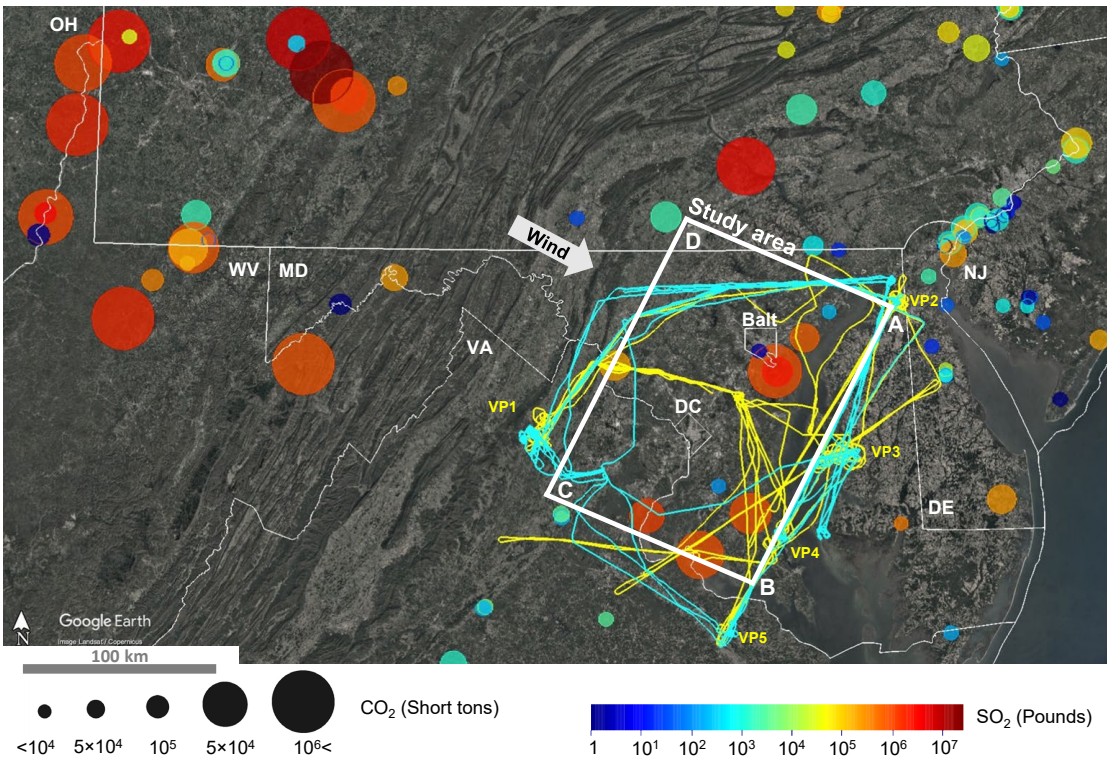

Figure 2.1. Overview of the FLAGG-MD aircraft campaign during February 2015 conducted in the Baltimore, MD and Washington, D.C. metropolitan areas; the white rectangle defines the Balt-Wash study area used throughout the analysis. Yellow and cyan lines indicate the UMD and Purdue aircraft flight tracks, respectively. The dominant wind direction during the campaign period is shown by the white arrow. Point emission sources are shown as circles; the size and color of these circles indicate the amount of CO_2 (size) and SO_2 (color) emitted from these sources in February 2015 (USEPA AMPD 2015). The VP labels indicate locations where vertical profile data were obtained. The points labeled A, B, C, and D denote the edge of the region for which the emission of CO_2 from the Balt-Wash region is found. The boundary of the vertical plane AB, for which transects at various altitudes were flown, is used to define the downwind study area to calculate the emission of CO_2 for all flights except UMD-RF9. The vertical plane BC is used to define the downwind boundary for UMD-RF9, since northeasterly winds were present on 26 February 2015.

The UMD aircraft conducted a total of nine research flights (UMD RF1-9) in February 2015. Figure 2.1 shows all of these flight tracks and Figure S2.1 shows individual flight tracks. During seven research flights (UMD RF1-6 and RF8) northwesterly winds prevailed, while a northeasterly wind was present on UMD RF9 and a southwesterly wind occurred on UMD RF7. For all flights, the UMD aircraft departed from the Tipton airport (located between Washington, D.C. and Baltimore) and first flew a horizontal transect upwind of the study area to sample the incoming air. For the downwind transects of UMD-RF1-6 and RF8, an imaginary vertical plane AB was defined at the location where polluted plumes from the major emission sources—power plants, the I-95 highway, and the Washington, D.C., and Baltimore, MD metropolitan areas—could be sampled separately under northwesterly wind condition (see Figure 2.1). The aircraft made multiple horizontal transects at different altitudes in the plane AB to capture the outgoing air. Several vertical profiles were taken to measure vertical distribution of trace gases and to estimate the planetary boundary layer (PBL) height. For UMD-RF9, the sampling at downwind transects at various altitudes was conducted along the plane BC, since this flight was conducted under northeasterly

winds. Data from UMD-RF7 are not used below because of the complex wind patterns prevalent in the study area on 24 February 2015.

The Purdue aircraft conducted a total of six research flights between 16 February to 11 March 2015 (Salmon et al., 2017, 2018) (Figure 2.1 and S2.1). Purdue flight tracks were designed in a similar manner to the UMD flights, aiming to measure mole fractions of CO_2 upwind and downwind of the Balt-Wash area. On 19 February 2015 (Purdue-RF3), the Purdue aircraft was coordinated with the UMD aircraft (UMD-RF4) to conduct direct comparisons of in-situ measurements of CO_2, other GHGs, and meteorological variables during a wingtip-to-wingtip segment that lasted about 40 minutes.

2.2.3 HYSPLIT transport modeling

In this study, the Hybrid Single Particle Lagrangian Integrated Trajectory (HYSPLIT) model was used to determine the sources of polluted plumes observed from the aircraft (Draxler et al., 1997; Stein et al., 2015). A series of back trajectories starting at the aircraft locations, at one second intervals, was computed using the default model configuration setup and NAM12 (North American Mesoscale Forecast System, 12 km horizontal resolution) as input meteorology. Forward transport modeling of power plant CO_2 plumes was conducted using HYSPLIT particle dispersion mode with NAM4 (4 km horizontal resolution). The number of particles released per cycle (variable name 'numpar') was set to 10^6. The output mass was divided by air density to obtain mole fraction (ichem=6). Horizontal grid spacing was specified as 0.1°, given that the objective of the modeling is to understand the inter-state transport of power

plant plumes in the eastern U.S. Vertical grid spacing was set at 100 m below 2000 m and at 500 m above 2000 m. All other configuration parameters were set at default values, as described in Draxler et al. (2014). As input emission sources, we used power plants listed in the Environmental Protection Agency's Clean Air Markets Division (EPA CAMD) datasets for Washington, D.C., Maryland, Pennsylvania, Virginia, West Virginia, and Ohio. The EPA CAMD emission dataset of facility-level hourly CO_2 emissions records was obtained from the Air Markets Program Data (AMPD) query system (USEPA AMPD, 2015).

2.2.4 VEGAS modeling and NDVI data

A VEgetation-Global Atmospheric-Soil (VEGAS) model simulation was used to calculate the biogenic flux of CO_2 over the Balt-Wash area during February 2015. VEGAS is a dynamic soil and vegetation model that simulates the growth of plant functional types based on meteorological data (Zeng et al., 2004, 2005). The model was run hourly at 9 km resolution using re-gridded NARR (North American Regional Reanalysis) data as meteorological input. The simulation was started in the year 1715 to provide a spin-up time for regional carbon pools.

In addition to the benefit of estimating the biogenic CO_2 flux for the study domain, gridded VEGAS biogenic CO_2 flux output was combined with the Normalized Difference Vegetation Index (NDVI) data to investigate the impact of biogenic CO_2 emissions on the background CO_2 that is needed for the mass balance calculation (see section 2.3.6). Since the VEGAS model was not specifically designed to compute biogenic emissions of CO_2 in regions with complex landscapes such as the Balt-Wash

study area, we have combined VEGAS output with NDVI data acquired within the study region during February 2015. First, gridded VEGAS output of net biogenic CO_2 flux was computed for the entire Balt-Wash study area. Next, version v1r12 NDVI data (4 km, weekly, https://www.star.nesdis.noaa.gov/smcd/emb/vci/VH/index.php) from the Visible Infrared Imaging Radiometer Suite (VIIRS) on the Suomi National polar-orbiting partnership (Suomi-NPP) was summed within each of the narrow grid boxes ($NDVI^{GRID\ BOX}$) perpendicular to line AB as shown in Figure S2.2. Then, the horizontal transect of the biogenic flux of CO_2 within the study region, along line AB, was found by multiplying the VEGAS output (i.e., a single number representative of the entire study region) by the value of $NDVI^{GRID\ BOX}$ for each specific grid box and dividing by the sum of $NDVI^{GRID\ BOX}$ for all grid boxes. In section 2.3.6, we describe the impact of biogenic CO_2 flux on the background CO_2 and the mass balance calculation.

2.2.5 Mass balance approach and sensitivity analysis

A mass balance approach was used to estimate the emission rate of CO_2 from the Balt-Wash area and from two local power plants. Under steady wind conditions, the horizontal flux of CO_2 crossing the vertical plane AB located downwind of an emission source can be considered as an approximation of the vertical flux of CO_2 over the emission source, while the air parcel was passing through the source (Trainer et al., 1995; White et al., 1983). A similar approach has been used in previous studies to estimate fluxes of trace gases such as CO_2, CH_4, CO, and NO_x from various emission sources (Cambaliza et al., 2014; Heimburger et al., 2017; Kalthoff et al., 2002; Karion et al., 2015; O'Shea et al., 2014; Peischl et al., 2016; Salmon et al., 2017, 2018). In this

study, the emission rate of CO_2 (F, mol/s) was calculated with the following equation:

$$F = \int_{z_i}^{z_f} \int_{x_i}^{x_f} \left([C]_{x,z} - [C_{bg}]_{x,z} \right) \cdot U_{x,z} \cdot k_x \, dxdz \quad (2.1)$$

where x is the horizontal and z is the vertical location in the plane AB. Variables x_i, x_f and z_i, z_f are the horizontal and vertical bounds of AB influenced by the emission source of interest, $[C]$ is the sampled number density of CO_2, and $[C_{bg}]$ is the computed background number density of CO_2. Also, U is the wind speed perpendicular to the aircraft heading and k is the scaling factor for U, defined as the ratio of the mean U during transport time over the emission source to the value of U measured at the downwind flights. A detailed description of each parameter is provided in the following sections.

2.2.6 Background mole fractions of CO_2

Previous studies have used the edge fitting method to estimate background CO_2 (Heimburger et al., 2017; Krautwurst et al., 2016; Salmon et al., 2018). For the Balt-Wash area, background regions within the downwind transects were designated at northern and southern edges. Then, the CO_2 background was defined by fitting a linear regression line to the mole fractions of CO_2 measured at both edges of the transects (Figure S2.3b, d, e, g). On 19 and 23 February 2015 the mole fractions of CO_2 measured between the Washington, D.C. and Baltimore, MD plumes along line AB in Figure 2.1 were lower than mole fractions of CO_2 measured at the edges of the downwind transect (Figure S2.3a, c, f). Our HYSPLIT transport modeling indicates that elevated CO_2 at the downwind transect edges on these dates was likely due to power plant plumes

transported from either Pennsylvania or West Virginia (see section 2.3.2). Therefore, an additional background region, approximately midway between the Washington, D.C. and Baltimore, MD plumes, was designated for the flights conducted on 19 and 23 February 2015. For the three flights (UMD-RF4, UMD-RF6, and Purdue-RF3) conducted on these two days, background CO_2 was determined by fitting two linear regression lines: one from the southern edge to the midway background flight segment and another from the midway segment to the northern edge. The background mole fractions of CO_2 were converted into background number density ($[C_{bg}]$) using in-situ measurements of temperature and the pressure, for use in Equation 2.1.

The accuracy of our estimate of the background CO_2 mole fraction was evaluated by conducting a comparison to upwind measurements of CO_2 (Figure 2.2). For the comparison, the CO_2 background value defined at each point of every downwind transect was examined for potential pairing to the upwind measurements of CO_2 conducted for the same flight. Forward HYSPLIT trajectories were computed every 1 sec of each upwind flight segment, which generally occurred along the line CD in Figure 2.1. For each forward trajectory, a successful pairing was determined if a trajectory crossed the downwind transect meeting the following conditions: 1) trajectory altitude was within the PBL at the crossing time of the downwind track, 2) the crossing time of the downwind track was within ±1 hour of the time the aircraft collected data. The upwind data were collected in early afternoon for all of the flights, and the downwind sampling occurred on average 2.5 hours later. Figure 2.2a shows a comparison of a 10 sec running mean of CO_2 within the PBL collected during the upwind portion of the indicated flights versus the background value of CO_2 computed

for the location at which the trajectory crossed the downwind track. The excellent agreement between the upwind measurements of CO_2 and our estimate background CO_2 (mean and standard deviation of 0.18±0.79 ppm) supports the validity of the carbon emissions computed using the mass balance approach. We are unable to compare upwind CO_2 to the estimate of background for UMD-RF9, because the aircraft flight track did not sample the composition of the atmosphere along line AD in Figure 2.1 that corresponds to the upwind location for this flight, due to the presence of northeasterly winds.

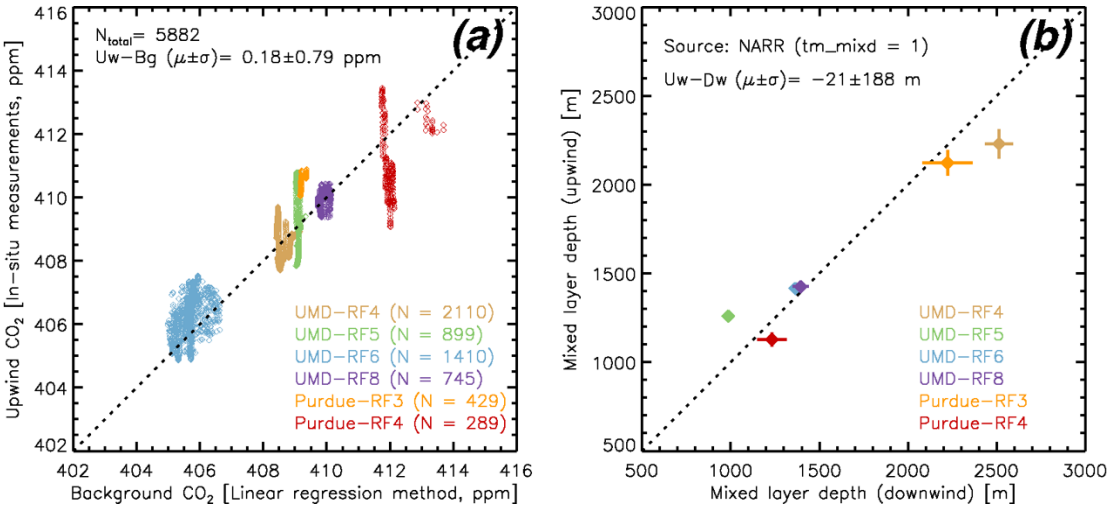

Figure 2.2. Scatter plot of the upwind CO_2 mole fraction (10 second running mean) versus the paired downwind, background estimate of CO_2. The number of paired data points for each flight is indicated on panel (a); the total number of paired points (5882) yields a mean and standard deviation of 0.18±0.79 ppm. Panel (b) shows the mixed layer depth extracted from HYSPLIT run using North American Regional Reanalysis (NARR) meteorological fields along the upwind aircraft flight track and the location of the paired, downwind data. Results are shown for six of the seven mass balance flights considered in the analysis, because upwind measurements of CO_2 were not obtained for UMD-RF9.

Figure 2.2b compares the depth of the mixed layer, for the upwind flight leg (ordinate) and downwind flight leg (abscissa). The values originate from the North

American Regional Reanalysis (NARR) meteorological fields for February 2015, because the depth of the PBL from NARR exhibits the closest agreement with the depth of the PBL inferred from our flight data. Figure 2.2 shows considerable variations in both the depth of the PBL and upwind CO_2, between the six flights for which such a comparison is possible. Undoubtedly, this variation in the depth of the PBL plays a role in value of CO_2 along the upwind leg. The fact that the depth of the PBL is stable between the upwind and downwind portions of the flight again supports the validity of the carbon emissions found using our mass balance approach.

For power plant plumes, the horizontal bounds of the plume were determined based on large, sharp gradients in the in-situ measurements of CO_2 as shown in Figure 2.3. The connection of these enhancements of CO_2 to local, nearby power plant emissions was confirmed based upon visual inspection of HYSPLIT back trajectories initialized every 1 s along the flight track, shown also in Figure 2.3. The CO_2 background for power plant plumes was defined as a linear function fit to the mole fractions of CO_2, measured by the Picarro (G2401-m) on board the aircraft, at the either side of the plume's bounds. All 16 power plant plumes considered below displayed large enhancements of CO_2 that could clearly be traced to a local, nearby power plant.

2.2.7 Wind

Recently, a systematic aircraft heading-dependent bias was identified in wind speed and direction recorded by the Garmin system onboard the UMD aircraft (Xinrong Ren et al., 2019). A series of bias correction methods was developed and applied to the wind measured by the UMD aircraft, utilizing a newly installed differential GPS

instrument, NAM4 wind data, and local wind profilers. Section 2.5.1 – 2.5.3 provide detailed descriptions on how the systematic bias in the aircraft wind measurements was corrected. The wind speed perpendicular to the aircraft heading (U) was calculated using the wind speed, wind direction, and true track angle of the aircraft measured downwind of the emission source of interest. Then, 10 second running means of U were used for the mass balance calculation. For the sensitivity analysis, the standard deviation of U during the downwind transect period was added/subtracted from the original U for the mass balance calculation.

From back trajectory analysis of seven mass balance flights (UMD RF4,5,6,8,9, Purdue RF3,4), we found that the average air transport time over the Balt-Wash area was ~5 hours, given the average wind speed of ~7 m/s across the study area. However, the value of U varies across the study area, which does have an impact on CO_2 emissions found using the mass balance approach. To account for the variability of U during the transport time of air across the study area, a scaling factor k was estimated in following manner. For each 0.1° × 0.1° horizontal grid, average U within the PBL (hereafter $\overline{\boldsymbol{U_{PBL}}}$) was derived from NAM4 for the hour closest to the mean aircraft observation time (Figure S2.4a). Then, the resulting values of $\overline{\boldsymbol{U_{PBL}}}$ were averaged within a series of diagonal latitudinal bins across the Balt-Wash study area (Figure S2.4b). For each latitudinal bin, the scaling factor k was calculated by dividing the mean of all $\overline{\boldsymbol{U_{PBL}}}$ with the $\overline{\boldsymbol{U_{PBL}}}$ at the downwind edge. Obtained k for latitudinal bins were interpolated and applied to individual wind measurements (U) (Figure S2.4c). We found that k values averaged for each of the seven mass balance flights range from 0.75 to 1.06 (Table 2.1). For the sensitivity analysis, k was calculated using the same method,

but for ±1 hour from the mean aircraft observation time. Then, the standard deviation of k within three hours span was added/subtracted from the original k for the mass balance calculation.

Table 2.1. Summary of the mass balance parameters used to estimate the emissions of CO_2 from the Balt-Wash area. For the boundary layer height (z_f), the best estimates and 1σ uncertainties are shown. For the mole fraction of CO_2 ($[CO_2]$), CO_2 background ($[CO_{2,bg}]$), perpendicular wind speed (U), and the wind variability during air transport across the study area (k), the mean and the standard deviation during the downwind flight period are shown (See section 2.2.5). The flux of CO_2 was calculated for each point in each transect, and thus the mean $[CO_2]$, $[CO_{2,bg}]$, U, and k values thus not directly translate into the mass balance estimate results.

Flight	Date 2015	Z_f [m]	$[CO_2]$ [ppm]	$[CO_{2,bg}]$ [ppm]	U [m/s]	k
UMD-RF4	Feb 19	1,372 ± 280	409.3 ± 0.8	408.5 ± 0.3	12.8 ± 1.6	0.95 ± 0.01
UMD-RF5	Feb 20	1,109 ± 139	411.2 ± 1.4	409.4 ± 0.2	5.6 ± 1.4	0.75 ± 0.04
UMD-RF6	Feb 23	1,013 ± 265	406.8 ± 1.1	405.7 ± 0.4	10.6 ± 1.5	1.06 ± 0.01
UMD-RF8	Feb 25	1,393 ± 137	410.1 ± 1.9	408.6 ± 0.9	5.3 ± 2.0	0.91 ± 0.05
UMD-RF9	Feb 26	896 ± 268	417.9 ± 2.5	414.2 ± 0.8	3.9 ± 1.1	0.90 ± 0.04
Purdue-RF3	Feb 19	1,372 ± 280	410.0 ± 0.5	409.2 ± 0.2	12.7 ± 1.3	1.00 ± 0.02
Purdue-RF4	Feb 27	1,626 ± 349	414.3 ± 2.4	412.6 ± 0.6	5.1 ± 1.6	0.98 ± 0.04

To address the impact of the scaling factor k on our determination of emissions of CO_2 from the Balt-Wash area, emissions were also estimated assuming consistent perpendicular wind speed throughout the transport time (k=1). When consistent wind (k=1) is assumed, the monthly total $FFCO_2$ emission was estimated to be 2.0 MtC, which is 5% larger than the estimate of 1.9 MtC that accounts for the variability of U during the air transport time. Further details are given in Figures S2.5 and S2.6. Given the relatively short transport time of power plant plumes between emission and aircraft

sampling, the scaling factor k =1 was used for the calculation of power plant emissions of CO_2.

2.2.8 Vertical and horizontal boundary

To include emissions of CO_2 transported above the PBL into our estimate of CO_2 emissions, the adjusted mixing height (z_{adj}) was determined and used as a vertical bound (z_f) of the mass balance equation. First, the well-mixed planetary boundary layer height (z_{pbl}, dashed line in Figure S2.7) and the entrainment height (z_e, dotted line in Figure S2.7), an altitude where mixing from the PBL has reached free tropospheric level, were determined from the vertical profiles of potential temperature and mole fractions of the trace gases (CO_2, CH_4, and H_2O). Then, the adjusted mixing height (z_{adj}) was calculated using $z_{adj} = (3z_{pbl} + z_e) / 4$, as described by Peischl et al. (2016). Also, $\pm 1\sigma$ uncertainty of z_{adj} was determined as $\pm (z_{pbl} - z_e) / 2$, again from Peischl et al. (2016). For flights that obtained multiple vertical profiles (UMD-RF4,5,8 and Purdue-RF3,4), the adjusted mixing height and its uncertainty ($z_{adj} \pm 1\sigma$) determined from each vertical profile were linearly fit as a function of the observation time. From this function, the vertical boundary of the PBL and its uncertainty ($z_f \pm 1\sigma$) were determined at the mid-point of the downwind flight period. For the flights with a single vertical profile in the downwind region (UMD-RF6,9), values of z_{adj} and their 1σ estimated from the only vertical profile were used to define $z_f \pm 1\sigma$. For the sensitivity analysis, values of $z_f \pm 1\sigma$ were used as the vertical boundary in the mass balance calculation.

Horizontal boundaries (x_i, x_f) were determined as the locations where the

HYSPLIT back trajectory passed through the southern and northern bounds of the Balt-Wash area (UMD-RF4,5,6,8 and Purdue-RF3,4). For UMD-RF9, horizontal boundaries were determined as the locations where the back trajectory went through the western or southern bound of the study area. To estimate the emission rate of CO_2, horizontal fluxes were calculated for each point in the downwind transects (unit: gC m^{-2} sec^{-1}). The calculated fluxes were averaged into a single value, then multiplied by the horizontal ($x_f - x_i$) and vertical boundary distances ($z_f - z_i$) (unit: gC sec^{-1}), as described by Equation 2.1.

2.3 Results and Discussions

2.3.1 Source identification and attribution: Baltimore, MD-Washington, D.C. area

During the aircraft campaign, spikes of CO_2 were often observed. For example, for UMD-RF5 on 20 February 2015, three spikes of CO_2 were recorded downwind of the Balt-Wash area (green shaded areas in Figure 2.3b). To determine the sources of these plumes, a series of HYSPLIT back trajectories were calculated. When the wind direction was consistent during the transport over the Balt-Wash area, which was the case for 20 February 2015, power plant plumes could be clearly isolated from the emissions of the surrounding urban region (Figure 2.3a). The first two spikes of CO_2 observed at 15:40 and 15:47 (EST) were attributed to the Morgantown (MT) and Chalk Point (CP) power plants, respectively. The spike of CO_2 observed downwind of the Baltimore, MD (16:05) was attributed to the Brandon Shores and H. A. Wagner (B&W) power plants, which are in close proximity. According to CEMS records, the B&W, MT, CP power plants emitted 1470, 980, 540 tons of CO_2 and 2.8, 0.8, 0.8 tons of SO_2

respectively, during a one-hour period from 14:00 PM to 15:00 PM on 20 February 2015. Simultaneous increases of the mole fractions of SO_2 for the three spikes of CO_2, showing ratios of SO_2/CO_2 mole fraction similar to those from CEMS records, confirm that the plumes were emitted from power plants. The B&W, MT, and CP power plants emitted total of 3.4 MtC in year 2015, contributing 75.4% of the annual total power plant emissions of CO_2 in Maryland (USEPA GHGRP, 2019).

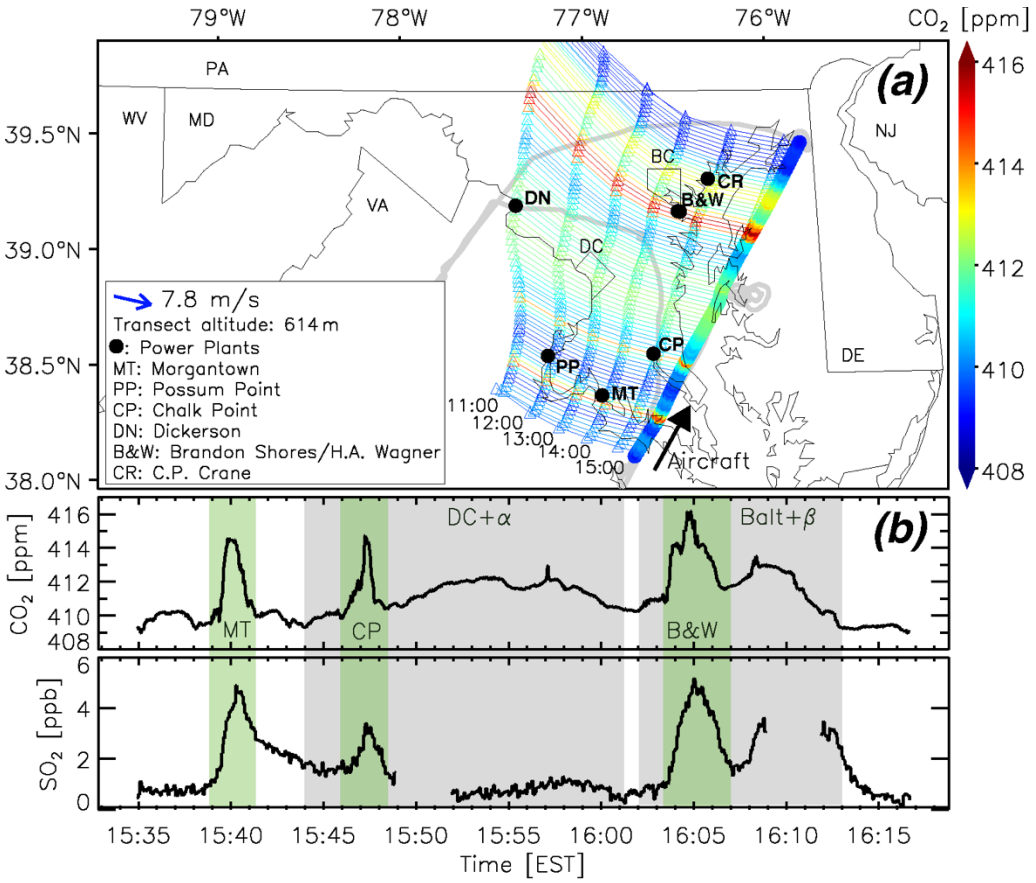

Figure 2.3. (a) Colored lines depict back trajectories initiated along the aircraft track, downwind of the Balt-Wash area on 20 February 2015 (UMD-RF5). Triangles indicate the locations of back trajectories at every hour. Black circles indicate the major power plants in the study area. Mean aircraft altitude and the wind speed and direction measured during the flight are shown in the left box. (b) Time series of mole fractions of CO_2 and SO_2 measured during the same flight track. Green shaded areas indicate the plumes partially attributed to local power plants while the grey shaded areas indicate urban plumes. The DC+α label indicates that the plume is attributed to Washington, D.C. and nearby Dickerson power plant. The Balt+β label indicates that the plume is

attributed to Baltimore, MD and to major power plants in Pennsylvania (labelled as PA in the map, see Figure 2.4 for further analysis). See section 2.3.6 for detailed spatial distribution of fossil-fuel CO_2 flux over the study area.

Along with the three spikes of CO_2 attributed to local power plants, broad areas of increased CO_2 were observed downwind of the Washington, D.C. and Baltimore, MD (grey shaded areas in Figure 2.3b). We argue that increased mole fractions of CO_2 downwind of the Washington, D.C. area were mostly induced by emissions from local fossil fuel combustion, while increased CO_2 downwind of Baltimore was induced by a mixture of plumes from that city and from several power plants in the state of Pennsylvania (See section 2.3.2).

2.3.2 Source identification and attribution: Inter-state transport of power plant plumes

During the aircraft campaign, several spikes in the mole fraction of SO_2 were observed both upwind and downwind of the Balt-Wash area. To find the sources of these plumes of SO_2, HYSPLIT back trajectories were calculated on six days (Figure 2.4a-f). These trajectories showed that some of the SO_2 plumes observed downwind of the Balt-Wash area are likely to be the same plumes observed on the upwind flight legs (Figure 2.4a, b, d, e). During UMD-RF8, the aircraft observed a broad increase of SO_2 north of Washington, D.C. due to advection from the westerly wind direction (Figure 2.4f). Figure 2.4g shows that several plumes of SO_2 observed downwind of the Balt-Wash area were transported from the mid-west Pennsylvania area where five large power plants are located. The total nameplate capacity of the five power plants was 6,444 MW (Coal: 90.3% Natural gas: 9.4%) according to USEIA (2016). The Homer City power plant was reported as one of the largest SO_2 emitting facility in the entire

U.S. for 2015 (USEPA AMPD, 2015). As the five power plants are geographically aligned from northwest to southeast in close proximity, a northwesterly wind is likely to merge the plumes from these power plants, leading to the inter-state transport of a highly polluted plume with relatively small horizontal width into the Balt-Wash area.

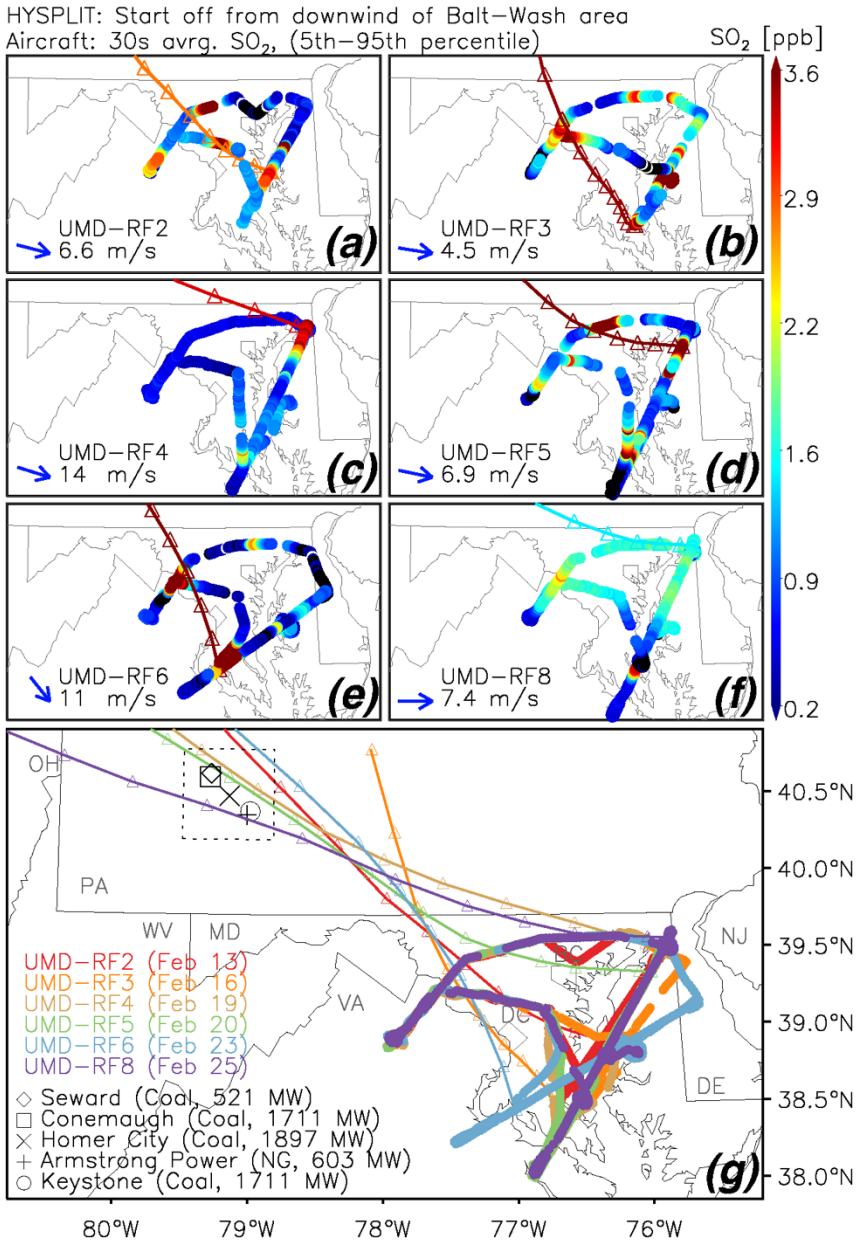

Figure 2.4. (a-f) Colored circles show mole fractions of SO_2 measured during six

flights in February 2015. Colored lines are back trajectories initiated at the location of the SO_2 plume observed downwind of the Balt-Wash area. Triangles on each trajectory show the location at every hour. Mean wind measured during the downwind flight is shown at the left-bottom corner of each panel. (g) A map showing same flight tracks and trajectories of (a-f) in a larger domain. The dashed box encloses the locations of five major power plants in Pennsylvania. The names of power plants, fuel, and their nameplate capacity are shown at the left-bottom corner (Source: USEIA, 2016).

To further investigate the impact of upwind power plant plumes on the aircraft measurements, forward transport modeling of power plant CO_2 was conducted for 19 and 20 February 2015 (UMD-RF4, 5). Figure 2.5 shows that airborne observations of the spikes in CO_2, induced by both local and upwind power plants, were well reproduced by the forward modeling (HYSPLIT CO_2). A contour map of HYSPLIT CO_2 shows that continuous flow of CO_2 from power plants in Pennsylvania (PA) and West Virginia (WV) sometimes passed through parts of the Balt-Wash area. According to the HYSPLIT analysis, CO_2 from power plants in PA passed downwind of Baltimore, MD and accounted for a significant portion of the total amount of CO_2 in the model grids (27.5% on UMD-RF4 and 35.4% on UMD-RF5). This forward modeling result agrees with the result from the SO_2 back trajectory analysis, which attributed some plumes of SO_2 observed downwind of Baltimore, MD to the power plants in PA (Figure 2.4c, d). However, CO_2 emitted by power plants in Ohio (OH) was relatively well distributed over a large horizontal distance when it reached the Balt-Wash area. This result implies that power plant emissions from OH and farther upwind states would have negligible impact on mass balance calculation for the Balt-Wash area. The emissions of CO_2 from power plants in PA and WV, however, must be considered in our analysis.

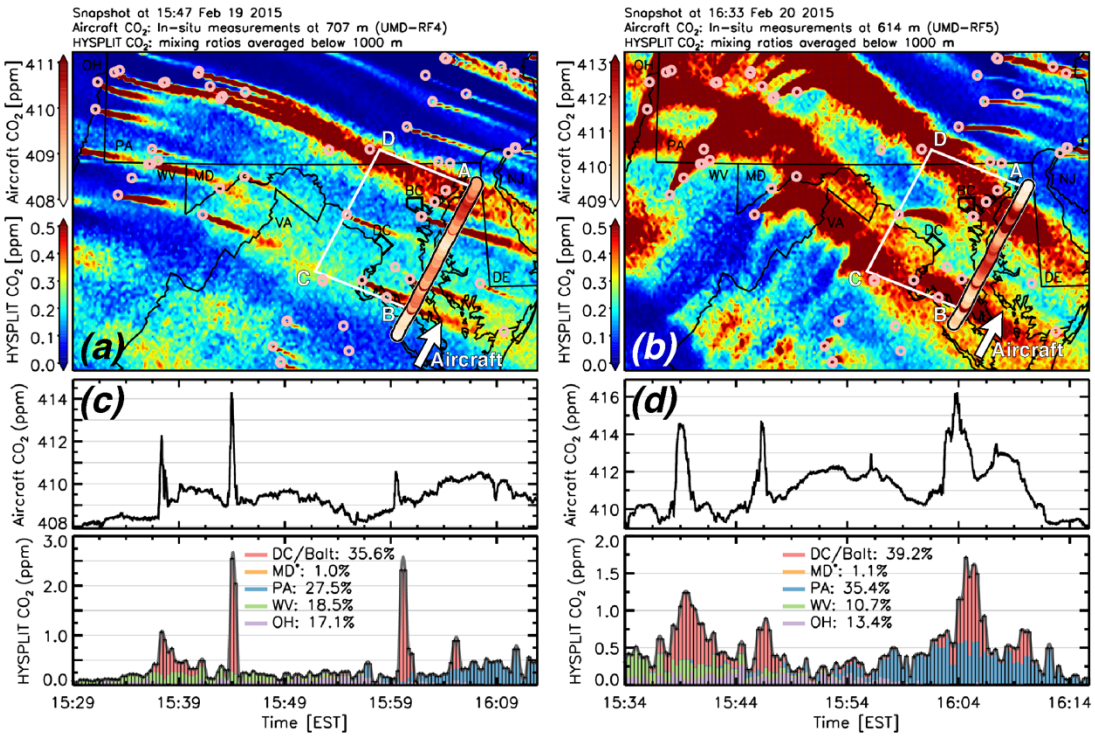

Figure 2.5. Maps showing HYSPLIT particle dispersion simulations of power plant emissions of CO_2 and flight tracks of (a) UMD-RF4 and (b) UMD-RF5. "HYSPLIT CO_2" labels (color bars and Y axes) indicate the enhancement of CO_2 due to power plant emissions averaged within the boundary layer. "Aircraft CO_2" labels indicate measured mole fractions of CO_2 for a single transect, along the line A at 707 m (UMD-RF4) and 614 m (UMD-RF5) altitude. The location of power plant point emission sources used for the modeling are shown as pink circles. (c, d) Time series of "Aircraft CO_2" at 707 m (UMD-RF4) and 614 m (UMD-RF5) altitude along the line AB and stacked bar plots of "HYSPLIT CO_2" that were sampled for aircraft locations of the in-situ data. Each color of the bar indicates the state or region where the sampled HYSPLIT CO_2 was emitted: i.e., emissions from the study area are denoted as DC/Balt. The percentage of power plant emissions from region, for the given transects, is also provided (numbers sum to 100%).

In summary, both the SO_2 back trajectory and CO_2 forward modeling results indicate that inter-state transport of power plant plumes can induce local increases of the mole fractions of CO_2 around the Balt-Wash area, especially when consistent northwesterly wind prevails. Accurate representation of the spatially varying CO_2 background is therefore needed to account for upwind power plant emissions of CO_2 in the mass flux calculation for the Balt-Wash area.

2.3.3 Power plant emissions: Evaluating the aircraft-based mass balance approach

Prior to applying the mass balance approach to the Balt-Wash area, the accuracy and precision of the technique was evaluated using the Continuous Emissions Monitoring Systems (CEMS) records for CO_2 from two local power plants. Several spikes of CO_2 could be attributed to either the CP or MT power plant (Figure 2.3), and were used for the mass balance calculation. The total uncertainty of the CEMS records was determined by propagating individual uncertainty in the following terms: volumetric flow rate/CO_2 concentration measurements by CEMS (USEPA, 2009), difference of CEMS records against fuel consumption based U.S. Energy Information Administration (EIA) datasets (Gurney et al., 2016; Quick & Marland, 2019), and atmospheric transport time of power plant plumes. A detailed description of this uncertainty propagation is given in Section 2.5.4.

In Figure 2.6a, colored symbols show the 16 aircraft-based mass balance estimates of emission rates of CO_2 for the CP and MT power plants. The black lines show the hourly emission record of each power plant reported to EPA CAMD. According to EPA CAMD, a total of 0.23 MtC was emitted by the two power plants during February 2015. Of the total emissions, 98.8% was measured directly by CEMS, while 1.2% was either calculated or went through substitution procedures. All emissions records during the mass balance flights period were solely from CEMS.

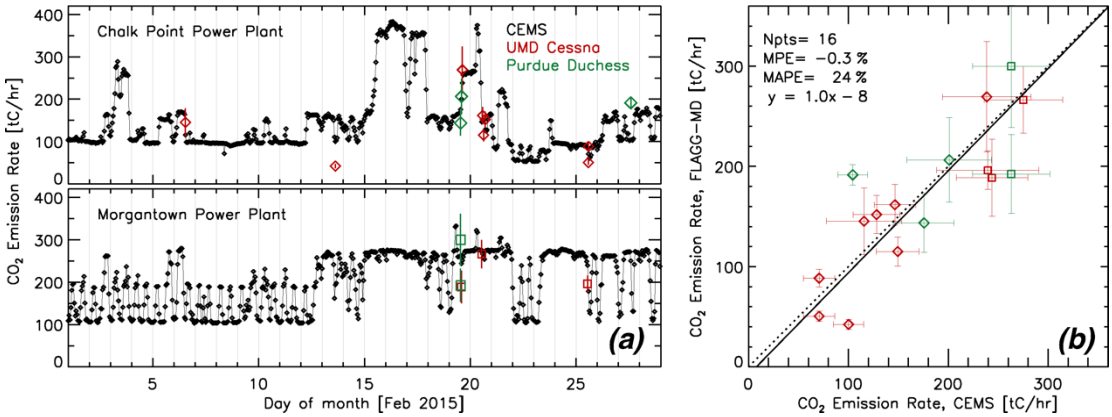

Figure 2.6. (a) Emission of CO_2 from the Chalk Point and Morgantown power plants in units of metric tons of carbon per hour. Black lines indicate the reported CEMS emission rates. Red and green diamonds represent the emission rates that we estimated using in-situ measurements from the UMD and Purdue aircraft, respectively. (b) Scatter plot showing the comparison of the same dataset in (a). Dotted and solid lines indicate 1 to 1 ratio and linear regression lines, respectively. Vertical error bars on each diamond indicate the 1σ uncertainty induced by the uncertainty in the adjusted mixing height (z_{adj}) (see section 2.5.3). Horizontal error bars indicate the combined uncertainty of the CEMS records and the plume transport time (see section 2.5.4).

The mean percentage error (MPE) and the mean absolute percentage error (MAPE) were –0.3% and 24%, respectively, for all 16 mass-balance estimates the CO_2 emission rate (FLAGG-MD) relative to that provided by CEMS (Figure 2.6b). The mean and standard deviation of the difference between the FLAGG-MD and CEMS emission values are –5±43 tC/hr. However, much larger differences, ranging from –58% to 84%, are observed for individual plume sampling comparisons. The large variation in these individual relative differences implies that the emission rate of CO_2 estimated from a single mass balance experiment may include significant random error. Such random error is most likely to be induced by incomplete mixing of power plant plumes within the boundary layer, causing the unrepresentative sampling of power plant plumes. The CO_2 background, often considered as a significant source of uncertainty in the mass balance approach for urban plumes (Cambaliza et al., 2014; Heimburger et al., 2017; J. Turnbull et al., 2018), is unlikely be a source of error for power plant

plumes given their narrow horizontal widths and a large value of the term ([C] – [C_{bg}]) that appears in Equation 2.1 (Figure 2.3). The mean value of ([C] – [C_{bg}]) at the peak of the spikes for the 16 sampled plumes was ~5.5 ppm. We also found that the combined error for multiple mass balance estimates of power plant emissions decreases approximately as the square root of the number of the plume crossings rises, which suggests the estimates are indeed influenced by random error. Our analysis suggests that power plants emissions can be estimated with MPE of ~10% (or less) when the total number of twelve (or more) plumes were sampled by aircraft for the mass balance calculation (95% confidence level). The importance of repeating mass balance experiments for the same emission source has been discussed in Heimburger et al. (2017).

2.3.4 The Baltimore, MD-Washington, D.C. area emissions: Sensitivity analysis

The emission rate of CO_2 from the Balt-Wash area was estimated based on the five UMD flights and two Purdue flights. Table 2.1 summarizes the mean and the standard deviation of the five mass balance parameters shown in Equation 2.1 for these seven flights.

Table 2.2 shows the baseline estimates of the emission rate of CO_2 that we consider to be the best estimates for the seven research flights. As the experimental period spans nine days in late February, the emission rate of CO_2 from the study area may be assumed to be constant during the sampling period. This assumption is supported by the fact that the emission rate of CO_2 derived from FFDAS shows small variation during the sampling period, having a relative standard deviation of 3% (See

section 2.3.7). Assuming a constant emission rate, the standard error of the mean at 95% confidence level (SEM95) can be calculated as a measure of the precision with the following equation: $\frac{t*\sigma}{\sqrt{n}}$, where t-student = 2.306, σ is the sample standard deviation of the seven mass balance estimates, and n is the number of the mass balance experiments (Heimburger et al., 2017). The mean of the seven baseline estimates and its SEM95 were 89,000±15,000 mol/s (3,870±630 tC/hr). This result indicates that the emission rate of CO_2 over the Balt-Wash area in the late February could be determined with the precision of 16% at 95% CL by repeating the mass balance experiments seven times within a nine-day span.

Table 2.2. Sensitivity test for the aircraft-based mass balance estimates of the emission of CO_2 from the Balt-Wash area. Baseline estimates from the seven flights are shown on the first row. Relative differences indicate the changes of the baseline estimate when the $\pm 1\sigma$ uncertainty of each mass balance parameter is used to calculate the emission of CO_2. The total 1σ uncertainty of each baseline estimate is shown as the relative standard deviation (RSD) at the bottom row. On the column labeled "Mean", the mean and SEM95 values of seven Baseline estimates were shown in the first row, and the mean values were shown for the remaining rows.

	UMD					Purdue		Mean
	RF4 Feb 19	RF5 Feb 20	RF6 Feb 23	RF8 Feb 25	RF9 Feb 26	RF3 Feb 19	RF4 Feb 27	
Baseline estimates [10^5 mol/s]	1.10	0.68	0.98	0.79	0.74	1.09	0.89	0.89 ± 0.15
Relative Differences (RD) [%]								
Wind Variability, Downwind	± 13	± 25	± 14	± 39	± 29	± 18	± 39	± 25
PBL height	± 20	± 13	± 27	± 10	± 30	± 20	± 21	± 20
CO_2 background	± 19	± 11	± 16	± 9	± 19	± 18	± 20	± 16
Instruments (Temp, Pres, CO_2)	± 8	± 3	± 6	± 4	± 2	± 11	± 5	± 5
Wind Variability, Transport	± 1	± 4	± 1	± 4	± 6	± 2	± 3	± 3
Total uncertainty [RSD, &]	± 32	± 31	± 34	± 41	± 49	± 33	± 49	± 38

The sensitivity of the baseline estimates was tested against the following five

parameters: background CO_2, PBL height, wind variability observed during the downwind flight, wind variability during air transport across the study area, and instrument uncertainty. For the sensitivity test, the $\pm 1\sigma$ uncertainty value of each parameter were used for the mass balance calculation. Section 2.2.5 describes how the 1σ uncertainty was determined for each of these five parameters. Table 2.2 shows relative differences (RD) of the newly calculated emission rates against their baseline estimates. On average, the estimated emission rate of CO_2 is most sensitive to the uncertainty of the perpendicular wind speed observed during downwind flight, with the mean of the seven RD as ±25%. The PBL height and the CO_2 background were the second and the third most important parameters contributing to the overall uncertainty in the emission rate of CO_2. Instrument measurement uncertainties (temperature, pressure, CO_2) and the wind variability during the air transport over the Balt-Wash area (parameter k) show less significant impact the emission estimate of CO_2 than other parameters.

The total uncertainty (1σ) for each baseline estimate was determined by propagating 1σ values of the five sensitivity parameters using Monte Carlo simulations. The total uncertainty of seven mass balance estimates ranged from ±31% to ±49%, with the mean of the seven total uncertainties being ±38%. The precision assigned to the mean of the seven independent mass balance estimates with SEM95 is ±16%, which is much lower than the average of the seven total uncertainties (38%). These results are comparable to findings from previous INFLUX studies that made use of an aircraft-based mass balance approach to estimate urban CO_2 emissions. Cambaliza et al. (2014) assigned an overall uncertainty of ~37% (or conservative ~50% when including

unknown systematic errors) to the CO_2 emission rate estimated from a single aircraft-based mass balance experiment. Heimburger et al. (2017) estimated CO_2 emission rates for the city of Indianapolis with SEM95 of ±17% by averaging nine aircraft-based mass balance estimates conducted during November-December 2014.

2.3.5 Comparison of top-down and bottom-up emissions

In this study, differences between atmospheric observation based (top-down) and inventory data based (bottom-up) approaches were studied from three different perspectives. First, geographical distributions of CO_2 flux were compared for five bottom-up products: Anthropogenic Carbon Emissions System version 1 (ACESv1, (Gately & Hutyra, 2017, 2018)), Emissions Database for Global Atmospheric Research version 4.3.2 (EDGARv432, (Janssens-Maenhout et al., 2017)), FFDASv2.2, the Open-Source Data Inventory for Anthropogenic CO_2 version 2018 (ODIAC2018, (Oda et al., 2018; Oda & Maksyutov 2011, 2015)), and CarbonTracker version 2017 (CT2017, (Peters et al., 2007)). Second, hourly emissions of CO_2 estimated from the aircraft (FLAGG-MD) were compared to hourly emissions from Fossil Fuel Data Assimilation System version 2.2 (FFDASv2.2, (Asefi-Najafabady et al., 2014; Rayner et al., 2010)). Finally, monthly emissions of CO_2 estimated from FLAGG-MD were compared to monthly emissions from the bottom-up products.

The bottom-up gridded products were largely developed based upon the emission downscaling method, which attempts to downscale national (or sub-national) and annual (or sub-annual) emissions inventories into model grids using spatiotemporal metrics (Gurney et al., 2019; Oda et al., 2019). For example, ODIAC2018 downscales

emissions estimates from the Carbon Dioxide Information Analysis Center (CDIAC) into a 1 km global grid, using the carbon monitoring action (CARMA) data for power plants and the Defense Meteorological Satellite Program (DMSP) nightlight imagery for non-point sources. FFDASv2.2 downscales national emissions estimates by the International Energy Agency (IEA) onto a 0.1° resolution lat/lon global grid, using data assimilation to combine DMSP nightlight, population, traffic pattern, and power plant data. EDGARv432 downscales national sectoral emissions estimates onto a 0.1° lat/lon global grid for each emissions sector specified by IPCC. ACESv1 downscales the sector-specific emissions estimates provided by the National Emissions Inventory (NEI), Greenhouse Gas Reporting Program (GHGRP), and Database of Road Transportation Emissions (DARTE) onto 1 km spatial resolution U.S. northeast regional grid. CT2017 is a data assimilation system with four sectors: fossil fuel combustion, biosphere, ocean, and fire. For the biosphere and ocean sectors, prior model CO_2 fluxes were optimized onto a 1° lat/lon global grid using atmospheric CO_2 observations and transport simulations. For the fossil fuel combustion sector, emissions from ODIAC and the "Miller" emissions data set were averaged onto a 1° lat/lon global grid. The net amount of biogenic CO_2 emitted from the Balt-Wash area during February 2015 was computed from CT2017, and this value was compared to the VEGAS estimate of the biogenic CO_2 emissions (section 2.3.8).

2.3.6 The Baltimore, MD-Washington, D.C. area: Spatial distribution of CO_2 flux

Figure 2.7 shows the spatial distribution of Fossil Fuel CO_2 ($FFCO_2$) flux over the Balt-Wash area from the five bottom-up products. These five bottom-up emission

inventories indicate similar overall patterns, but distinctly different geographic distributions of the emissions due to variations in the underlying metrics that drive the emissions as well as spatial resolution. ACESv1 (with a 1 km resolution) shows highly resolved geographical distributions of $FFCO_2$, such as the Beltway around Washington, D.C. and I-95 highway connecting major cities in the northeast corridor, due to their use of census block-level geospatial information (Gately & Hutyra, 2017). ODIAC2018, also at 1 km resolution, does not resolve individual roads due to their use of satellite-observed nighttime light data as a spatial emission proxy for non-point source emissions (Oda et al., 2018; Oda & Maksyutov, 2011). Still, it is noticeable that the global model ODIAC2018 shows a horizontal transect of CO_2 flux summed across the study area that is similar to that from the regional model ACESv1 (Figure 2.7f). The difference between ACESv1 and ODIAC2018 emissions would be less significant at an aggregated coarser spatial resolution, such as the resolution of the many inverse model simulations (Oda et al., 2019). Maps of CO_2 flux from FFDASv2.2 and EDGARv432 (0.1° resolution) show emission hot spots for the major power plants and the urban areas. Emissions from these power plants are represented by the higher resolution ACESv1 and ODIAC2018 inventories but are difficult to see on panels (a) and (b) of Figure 2.7 because the pixels are so small. Horizontal transects of the CO_2 flux derived from FFDASv2.2 and EDGARv432 exhibit an overall similar shape to those from ACESv1 and ODIAC2018, while spikes induced by power plants are more apparent in the flux transects from ACESv1 and ODIAC2018 due to higher spatial resolution (Figure 2.7f). The CT2017 inventory has a 1° lat/lon resolution, and hence the CT2017 map of $FFCO_2$ is more spatially uniform at the scale of our study domain,

since there are only 4 grid cells covering the Balt-Wash area.

According to VEGAS, the net amount of CO_2 emitted by the biogenic sector was ~0.4 MtC in the Balt-Wash area during February 2015. However, the horizontal transect of biogenic CO_2, simulated by VEGAS and scaled by NDVI (see section 2.2.4), is nearly constant across the Balt-Wash area during February 2015 (Figure 2.7f). This horizontal transect for biogenic emissions across our study area indicates that the CO_2 background, defined by the linear fitting method, is likely to already include the enhancement signal due to biogenic emissions. Therefore, we did not attribute any of the CO_2 flux found from the mass balance estimate to the biogenic sector (Figure 2.8). We acknowledge that the lack of any independent source of validation for VEGAS/NDVI outputs, such as radiocarbon measurements or eddy covariance flux towers, might be a weakness in our analysis. On-going efforts to develop $^{13}CO_2$ and radiocarbon measurements from NIST northeast corridor tower network (Karion et al., 2019) and urban biospheric CO_2 models (Hardiman et al., 2017; Smith et al., 2019) will provide further opportunity to study the impact of biogenic CO_2 flux on the aircraft-based mass balance estimates.

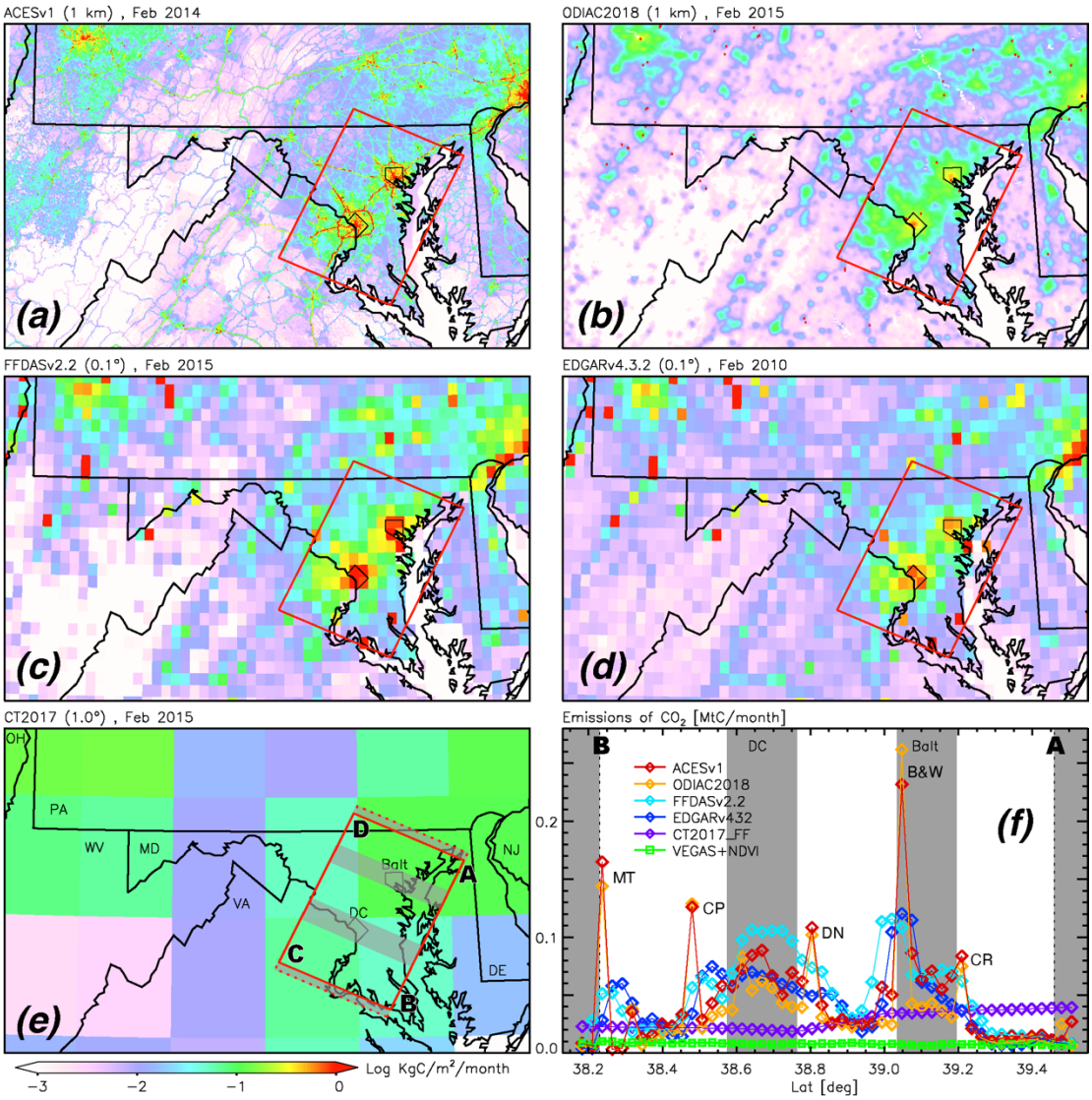

Figure 2.7. Maps of $FFCO_2$ flux over the Mid-Atlantic region from (a) ACESv1, (b) ODIAC2018, (c) FFDASv2.2, (d) EDGARv432, (e) CT2017. The Balt-Wash study area is indicated as a red box. (f) Horizontal transects of CO_2 flux derived from the biogenic model (VEGAS+NDVI) and the five $FFCO_2$ products (Unit: Million tons Carbon (MtC) per month). These transects were obtained by summing the flux along diagonal latitudinal bins, as indicated by four grey shaded areas shown in panel (e) and (f) (SE corner and NE corner of a red box, Washington, D.C. and Baltimore). The x-axis in (f) represents the latitudes along the line AB shown in panel (e). For major spikes, abbreviated names of the power plants are shown (see Figure 2.3).

2.3.7 Hourly emission rate of CO_2 from the Baltimore, MD-Washington, D.C.

The FLAGG-MD estimate of fossil-fuel combustion CO_2 ($FFCO_2$) emission rate is derived from the baseline mass balance estimates shown in Table 2.2. First, the emissions of CO_2 from human/pet respiration (human, dog, and cat) are estimated based on the following assumptions: the population in the Balt-Wash study area (red box, Figure 2.7e) was ~8.1 million in February 2015 (CIESIN, 2018); the CO_2 release rate by human respiration is 254 gC/person/day (Prairie & Duarte, 2007); dog/cat ownership is 0.22 dogs/person and 0.24 cats/person, and the dog/cat release rate of CO_2 is 25% of the human release rate (American Veterinary Medical Association, 2012). Next, the estimated emissions from human/pet respiration are subtracted from the baseline mass balance estimates. Then, the remainder of the mass balance estimates was apportioned to either $FFCO_2$ or Non-$FFCO_2$ Anthropogenic emissions (hereafter '$NFA\text{-}CO_2$') by applying the ratio derived from the Maryland GHG inventory for year 2014 (MDE, 2016). The $NFA\text{-}CO_2$ consists of following sectors: 1) industrial processes (cement manufacture, limestone and dolomite, soda ash, ammonia and urea production), 2) agriculture (urea fertilizer usage), 3) waste management (waste combustion, landfills, and residential open burning). Note that emissions from gasoline for on-road transportation were solely regarded as $FFCO_2$, as the emissions from ethanol (E85) in gasoline comprises only ~0.1% of total emissions from gasoline for on-road transportation (MDE, 2016). See Section 2.5.5 for a detailed description of the method utilized for human/pet respiration and the $FFCO_2$ to Non-$FFCO_2$ ratio from the Maryland GHG inventory, and their associated uncertainties. Note that we did not apportion any of the mass balance estimates to the biogenic sector, as discussed in section 2.3.6.

Figure 2.8 shows the emission rates of CO_2 from the Balt-Wash area estimated from seven FLAGG-MD flights and corresponding FFDASv2.2 estimates. On average, $FFCO_2$ comprises 93% of the mass balance estimates, while NFA-CO_2 and human/pet respiration comprises 4.6% and 2.6%, respectively. Overall, the emission rate of $FFCO_2$ from FFDASv2.2 for the flight days was 32% larger than that from FLAGG-MD but within the 1σ uncertainty range for most flights, except UMD-RF5. Still, such level of agreement is very meaningful given that FLAGG-MD and FFDASv2.2 use two independent approaches: aircraft observation-based sampling versus a data assimilation framework for disaggregating the annual/national inventory into hourly/0.1° grids.

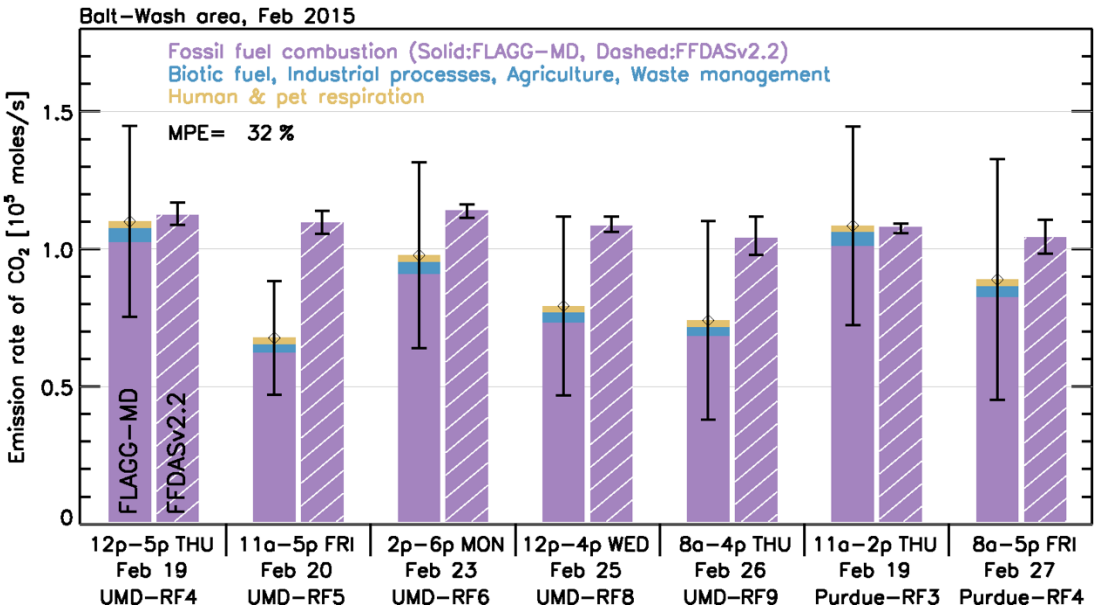

Figure 2.8. The emission rates of CO_2 from the Balt-Wash area during the sampling period of seven research flights in February 2015. Solid bars and their black vertical lines indicate the seven FLAGG-MD baseline estimates and their 1σ uncertainty range (Table 2.2). FLAGG-MD mass balance estimates were apportioned to $FFCO_2$ (purple), Non-$FFCO_2$ Anthropogenic emissions (NFA-CO_2, blue) and the human/pet respiration (yellow) (See Section 2.5.5). Dashed bars indicate corresponding $FFCO_2$ from FFDASv2.2. The black vertical lines at the top of the FFDASv2.2 bars (dashed) indicate the minimum to maximum hourly emission rates of $FFCO_2$ for each time period, and thus are not an uncertainty estimate of FFDASv2.2.

Turnbull et al. (2018) highlighted that the background CO_2, determined from the edge fitting method, is likely to be overestimated when there are nonzero emissions over the edge region of the study domain. In their study, CO_2 flux values were computed using an approach similar to Equation 2.1. Then, computed CO_2 flux values were scaled to a background-corrected aircraft mass balance flux by adding a mean CO_2 flux value for the rural area outside the aircraft footprint which was determined from a bottom-up inventory. Should we take the same approach, using either FFDAS or ODIAC to define the emissions of CO_2 along the narrow vertical boxes that define region illustrated in Figure 2.7, our value of $FFCO_2$ for the Balt-Wash area would increase by 30%, rising from 1.9 MtC to 2.5 MtC. This type of adjustment is not used in our analysis for two reasons. First, this adjustment implicitly assumes our estimate of background CO_2 is too large by approximately 0.3 ppm, whereas the comparison of the mole faction of background CO_2 to the measured upwind mole fraction of CO_2 already indicates a potential bias of 0.18 ppm (Figure 2.2a). If we were to adjust background CO_2 to adjust for possible unaccounted emissions in these edge, rectangular regions, the scatter plot between upwind and background CO_2 would exhibit such a bias that would begin to approach the standard deviation of the difference between upwind and background CO_2. Second, this adjustment assumes that anthropogenic emissions of CO_2 can be well defined in sparsely populated geographic regions by global models. We are reluctant therefore to make such an adjustment to our estimate of $FFCO_2$ for the Balt-Wash area, but we acknowledge that our definition of background CO_2 found using the method illustrated in Figure S2.3 could potentially need revision, due to lack of explicit consideration of anthropogenic emissions of CO_2

in these edge regions. Our approach is similar to the methodology used in numerous other recent mass balance studies (Heimburger et al., 2017; Krautwurst et al., 2016; Xinrong Ren et al., 2019).

Finally, we acknowledge that the rectangular-shaped region (Figure 2.7), determined based on the dominant wind direction, may not perfectly represent the emissions area that induced enhanced CO_2 observed by the aircraft, especially when uncertainties associated with wind variability determination are significant. Such mis-representation of the emissions area could have potentially contributed to the difference between top-down and bottom-up estimates (Lopez-Coto et al., 2020; J. Turnbull et al., 2018). In this study, flight-by-flight adjustment for the geographic study area was not attempted, as six of the seven flights share similar flight patterns and wind conditions. Unlike the other flights, UMD-RF9 was conducted under northeasterly wind conditions.

2.3.8 Monthly emissions of CO_2 from the Baltimore, MD-Washington, D.C.

The four bottom-up gridded products cover different years (i.e., EDGARv432: 2010, ACESv1: 2014, FFDASv2.2 and ODIAC2018: 2015) with varying temporal resolution (i.e., EDGARv432 and ODIAC2018: monthly, FFDASv2.2 and ACESv1: hourly). To facilitate the comparison among these bottom-up models and our mass balance estimates, the amounts of $FFCO_2$ emitted during the month of February in the Balt-Wash study area were computed from each bottom-up product and our seven mass balance estimates shown in Figure 2.8. No further attempts were made to harmonize the temporal mismatch existing in EDGARv432 (year 2010) and ACES v1 (year 2014). The FLAGG-MD monthly total $FFCO_2$ emission was estimated by temporally scaling

up the seven FLAGG-MD emission rates of $FFCO_2$, shown in Figure 2.8. The Temporal Improvements for Modeling Emissions by Scaling (TIMES), which provides scaling factors for diurnal and weekly variability of $FFCO_2$ in global rectangular 0.25° lat/lon grids, was used for the temporal scaling process (Nassar et al., 2013). The monthly emissions from human/pet respiration and NFA-CO_2 were estimated as described in section 2.3.7. The major challenge for comparing different bottom-up gridded products is to harmonize various emission source sectors covered by each product (Gately & Hutyra, 2017; Gurney et al., 2019; Oda et al., 2019). In this study, source sector harmonizing was only conducted for EDGARv432 (see Section 2.5.6), while all available sectors in other bottom-up products (ACESv1, FFDASv2.2, and ODIAC2018) were used to derive $FFCO_2$ emissions. Thus, sectoral mismatching among the FLAGG-MD estimate and the four bottom-up products exists for the following sectors: cement manufacturing, gas flaring, aviation, and oil and gas extraction, refining, and transport. These mismatching sectors account for ~4% of the total $FFCO_2$ in our study domain (see Section 2.5.6). Note that one of the main objectives set for developing these global bottom-up gridded products was to provide a prior CO_2 flux for use in inversion modeling (Oda et al., 2018). Therefore, $FFCO_2$ flux values at specific time-space model grids should be regarded as a climatological mean rather than snapshot of the truth (Gurney 2018).

We estimate that 2.4 MtC of CO_2 was emitted from the Balt-Wash area during February 2015, according to the FLAGG-MD estimate (all emission other than biogenic) and VEGAS simulations (biogenic CO_2) (Figure 2.9). The total 2.4 MtC consists of 1.9 MtC of $FFCO_2$ (78% of the total), 0.4 MtC of biogenic CO_2 (15%), 0.1

MtC of NFA-CO_2 (4%), and 0.06 MtC of human/pet respiration (3%). The mean and the standard deviation of the four bottom-up estimates of $FFCO_2$ were 2.2±0.3 MtC (FFDASv2.2: 2.5 MtC, ACESv1: 2.3 MtC, EDGARv432: 2.0 MtC, ODIAC2018: 1.9 MtC), which is 15% larger than the FLAGG-MD estimate of $FFCO_2$ (1.9±0.3 MtC). The ODIAC2018 bottom-up estimate of $FFCO_2$ shows best agreement with the top-down FLAGG-MD estimate.

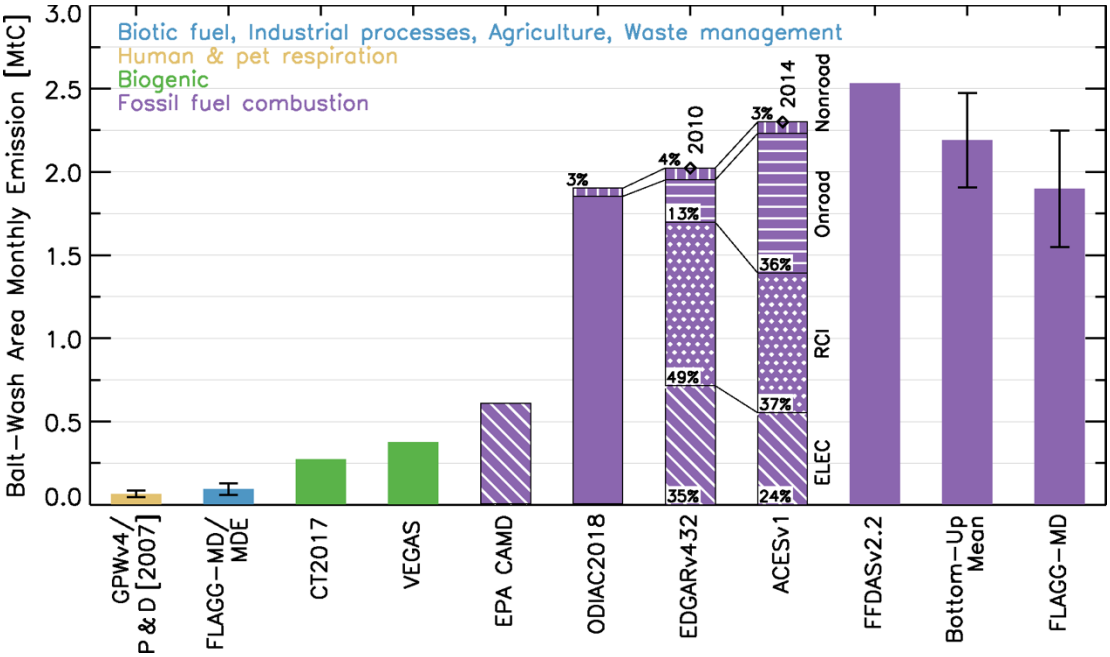

Figure 2.9. Monthly emission of CO_2 from the Balt-Wash area for February 2015. The emission by human/pet respiration (yellow) was estimated using population data (GPWv4, (CIESIN, 2018)) and the average respiration rate from Prairie & Duarte (2007) (see Section 2.5.5). Non-$FFCO_2$ Anthropogenic emissions (NFA-CO_2, blue) were calculated from FLAGG-MD mass balance estimates using the scaling factor derived from the MDE GHG inventory 2014 (MDE, 2016). EDGARv432 and ACESv1 were available for 2010 and 2014, respectively. The four bottom-up $FFCO_2$ estimates (ODIAC2018, EDGARv432, ACESv1, and FFDASv2.2) contain several mismatching emission sectors, and thus are not directly comparable (see text). Sectoral emissions from EDGARv432 and ACESv1 were aggregated into four categories: electricity generating facilities ("ELEC", diagonal), residential, commercial, and industrial ("RCI", dotted), on-road (horizontal) and non-road transportation (vertical). See Section 2.5.6 for emission sectors covered by each bottom-up product. The "Bottom-Up Mean" bar and its vertical error bar indicate the mean and standard deviation of the four bottom-up $FFCO_2$ estimates. The error bar on the FLAGG-MD symbol indicates

the 1σ uncertainty range of the best estimate.

ACESv1 and EDGARv432 provide sectoral emissions of $FFCO_2$ for years 2014 and 2010, respectively. Based on ACESv1, power plant emissions were 24% of the monthly total $FFCO_2$, while they were 35% of the monthly total $FFCO_2$ according to EDGARv432 (Figure 2.9). Estimates from EPA CAMD and FLAGG-MD for our study area suggest power plant emissions accounted for 29% of the monthly total $FFCO_2$ emissions in February 2015. On-road transportation emissions account for 36% of the ACESv1 estimate, while they only account for 13% of the EDGARv432 estimate. A significant difference of on-road emissions between ACESv1 and EDGARv432 might be due to the temporal mismatching (i.e., 2010 versus 2014) of the two inventories, but more likely reflects a bias in either one or perhaps both products. Gately et al. (2013) and McDonald et al. (2014) reported that EDGAR overestimates urban vehicles emissions in major U.S. cities. However, the recent update of EDGAR version 4.3.2 addressed this issue by adopting proxy layers for various roads and vehicles types (Janssens-Maenhout et al., 2017). We have not attempted to further quantify the source of the difference between on-road emissions of CO2 for these two inventories, as this effort is beyond the scope of this study. We leave the detailed analysis of sectoral composition of urban $FFCO_2$ for future work.

We would like to emphasize that this study provides an independent, objective measure for the emission comparison. Evaluation of downscaled emissions is often difficult mainly due to the lack of physical measurements (Andres et al., 2016; Oda et al., 2018) and often done by inter-comparison of emission inventories that allow only for characterization of differences among inventories. This study demonstrates the use

of atmospheric measurements for examining the errors and biases in the emission inventories.

Finally, we compare ODIAC2018, which showed the best agreement against our aircraft-based estimate of the monthly CO_2 emissions, to the Maryland GHG inventory published by the Maryland Department of the Environment (MDE) (MDE, 2016). The Maryland GHG inventory estimated that 18.8 MtC of $FFCO_2$ was emitted from Maryland during year 2014, while ODIAC2018 estimated 20.2 MtC for the same domain in 2014. The overall excellent agreement among the top-down approach, bottom-up models, and State emission inventory is promising given the fact that each relies on independent datasets and methodologies.

2.4 Conclusions

The first FLAGG-MD aircraft campaign was conducted during February 2015 to study the emissions of CO_2 in the Balt-Wash area. Several conclusions are drawn from this study.

First, a series of HYSPLIT transport modeling analyses was conducted to provide source attribution of the plumes of CO_2 observed by the aircraft. A number of plumes of CO_2 could be attributed to either Washington, D.C. and Baltimore, MD, or the major power plants in the study area. We found that inter-state transport of power plant plumes can induce a substantial local increase of CO_2 throughout the Balt-Wash area, increasing the spatial variability of background CO_2.

Second, the accuracy and precision of the aircraft-based mass balance approach

were tested against local power plant emissions, and also the sensitivity of the approach was tested for urban emissions. Emissions of CO_2 from two local power plants were estimated using aircraft data and the resulting estimates were found to have no discernible systematic bias, with a mean percentage error of −0.3 % compared to corresponding CEMS data for 16 cases. Also, power plants emissions could be estimated with MPE of ~10% when a total number of twelve plumes was sampled by the aircraft for the mass balance calculation (95% CL). These results demonstrate that the accuracy of mass balance estimates increases and as the number of mass balance experiments increases for the same target emission source (Heimburger et al., 2017; Karion et al., 2015). From a sensitivity analysis, we found that the variability of the wind speed and direction downwind of the study area have the largest impact on the mass balance calculation, followed by the boundary layer height and the specification of background CO_2. The 1σ uncertainty of a single mass balance estimate of CO_2 emission from the Balt-Wash study area can be significant, ranging from ±31% to ±49%. However, we also found that the precision assigned to the mean of the seven mass balance estimates was considerably better, with a SEM95 of ±16 %. This result supports the findings from previous studies: the precision of the mass balance estimate of CO2 emissions over urban regions is improved by repeating mass balance experiments numerous times, within a short span of time.

Finally, differences among the five bottom-up models (ACESv1, CT2017, EDGARv432, FFDASv2.2, and ODIAC2018) and the top-down estimate were studied from the perspective of both the geographical distribution of CO_2 flux and the total emissions over the Balt-Wash study area. With respect to the geographical distribution

of CO_2, we found that horizontal transects of CO_2 flux across the Balt-Wash area derived from four models (ACESv1, ODIAC2018, EDGARv432, and FFDASv2.2) have similar structures, showing spikes for the area where major power plants and highly developed areas are located. Only ACESv1 provided spatial distribution of CO_2 flux on the spatial scale of individual roads. From the perspective of total monthly emissions, the FLAGG-MD aircraft flights yield and estimated 1.9±0.3 MtC as the amount of $FFCO_2$ emitted from the Balt-Wash area during February 2015, and the four bottom-up models (except for CT2017) estimated 2.2±0.3 MtC. ODIAC2018, which provides downscaled emissions for year 2015, shows best agreement with the FLAGG-MD top-down estimate. Evaluation of subnational emissions of bottom-up models is often limited to an evaluation based on an inter-comparison among different models. This study provided an independent, objective measure for the inventory evaluation. Additionally, we found that the statewide annual total $FFCO_2$ emissions in the Maryland (MDE) GHG inventory was 7% lower than the ODIAC2018 estimate.

Numerous efforts are currently underway to better understand urban emissions of CO_2. For instance, the recent installations of observation towers and low-cost sensors around the Balt-Wash area will provide improved constraints on spatiotemporal variability of the CO_2 background (Lopez-Coto et al., 2017; Martin et al., 2017, 2019; Mueller et al., 2018). Also, radiocarbon measurements and urban-specific biospheric CO_2 models will provide better understanding on the impact of biogenic CO_2 flux on the aircraft-based mass balance approach. A new version of VEGAS currently under development will incorporate an accurate representation of the diurnal cycle of the biogenic flux of CO_2. Lastly, frequent and regular aircraft campaigns in the future will

provide resources to better understand the gaps among top-down approaches, bottom-up models, and state/local GHG inventories, benefiting both stakeholders and the carbon cycle modeling community.

2.5 Supporting Information

2.5.1 Wind Bias Detection

The existence of the heading-dependent bias in the wind speed measured by the Garmin G600 system onboard the UMD Cessna aircraft was first identified by colleagues at the Pennsylvania State University (Ren et al., 2019). To address this issue, a series of calibration flights were conducted in October 2017 with the same UMD Cessna aircraft used for the flights in February 2015. For these calibration flights, the Cessna aircraft was equipped with both the original Garmin system and a newly installed differential GPS (DGPS) system, which measures aircraft true heading precisely with an accuracy of 0.05º. Figure S2.8 shows that the aircraft heading measured by the original Garmin system has a cosine-shaped systematic bias with respect to the aircraft heading measured by the DGPS system. The cosine-shaped bias in the Garmin heading measurement implies the existence of a hard-iron effect during the October 2017 flights: i.e., the permanent magnetic field that exists in the aircraft vessel interferes with the magnetometer's reading of the Earth's magnetic field.

For the February 2015 flights, neither DGPS data nor other kinds of records exist that could be used to directly quantify the magnitude of the hard-iron effect on the Garmin heading. However, the difference between measured wind speed and output of the NAM4 model as a function of aircraft heading can be analyzed to qualitatively

show the existence of the hard iron effect during the February 2015 flights (Figure S2.8b). The 'W' shaped pattern in Figure S2.8b, where the smallest differences of the wind speed were found near 90º and 270º and the largest differences were found near 0º, 180º, and 360º, demonstrates the existence of a hard iron effect during the mass balance flights conducted in February 2015.

2.5.2 Wind Bias Correction

The original wind data measured by the Garmin system during February 2015, which we call hereafter version 1 (v1) wind, include an error induced by the systematic bias in the aircraft heading reported by the Garmin G600 system (Figure S2.8). From the original v1 wind data, the v2 wind field (speed and direction) was derived by correcting the systematic heading bias. Then, the v3 wind field in which the accuracy is further improved was derived utilizing NAM4. Table S2.1 summarizes the differences in the wind speed perpendicular to the aircraft heading for these three versions of the wind field. The following paragraphs describe the method used to derive the v2 and v3 wind fields.

First, the systematic heading bias for the February 2015 flights data was corrected using the fourth-degree polynomial function given at the top of Figure S2.8a, which was obtained from the calibration flights conducted in October 2017. Following the correction of the heading bias, calibration coefficients of +0.8º and +1.3% were applied to the headings and the true air speeds (TAS), respectively (see Supplement of Ren et al., 2019). Then, the v2 wind speed and wind direction were calculated based

upon the bias-corrected/calibrated headings and TAS measurements, along with the original records of ground speed (GS) and true track angle (TTA).

Even after the bias correction and the calibration of the heading and TAS measurements, a systematic bias could still be present in the v2 wind if the magnitude and direction of the hard-iron effect in February 2015 was significantly different from that in October 2017.

The same aircraft had been used for both flight months; there is no record of how internal aircraft electronics and support structures may have changed. To address this issue and further improve the accuracy of the v2 wind, NAM4 model wind was used to calculate v3 wind data in the following manner. For the downwind transects measurements for each flight, 10 second running means of the perpendicular wind speed were calculated from v2 wind and from NAM4 wind, respectively ($U_{\perp,x,z}^{V2}$ and $U_{\perp,x,z}^{NAM4}$), as shown in Figure S2.10. From the two sets of perpendicular wind speed, the mean difference ($U_{\perp}^{NAM4} - U_{\perp}^{V2}$) was calculated. Then, v3 perpendicular wind speed was calculated by adding the mean difference to the v2 perpendicular wind speed during the downwind transects (i.e., $U_{\perp,x,z}^{V3} = U_{\perp x,z}^{V2} + \overline{U_{\perp}^{NAM4} - U_{\perp}^{V2}}$).

2.5.3 Wind Evaluation

For the evaluation of the series of the aircraft wind correction procedures described in section 2.5.2, three analyses were conducted. First, wind profiler data was used to evaluate the accuracy and the precision of the NAM4 wind data that is a factor in the derivation of the v3 aircraft wind data. Second, the NAM4 wind was used to assess the variations among the three versions of the aircraft winds. Finally, the

Continuous Emissions Monitoring System (CEMS) measurement of CO2 emissions from power plants was utilized to evaluate the accuracy of the three versions of the aircraft wind field.

Figure S2.9 shows a comparison of four variables (wind speed, wind direction, U and V components of the horizontal wind) between the NAM4 and the wind profiler observations at the Beltsville, Maryland site on 8 days in February 2015. An excellent correlation is found between the NAM4 and profiler data for each of these four wind components, without any noticeable systematic bias. The mean difference of wind speed between the NAM4 and the profiler was found to be 0.2 m/s, which translates into a 2.6 % uncertainty in the CO2 flux estimation.

Figures S2.10 shows a comparison of the perpendicular wind speed derived from the NAM4 versus that derived from the three versions of the aircraft wind field, for flight MD RF4 conduction on 19 February 2015. The original v1 perpendicular wind speed was found to be consistently faster than the value from NAM4. The v2 wind field (i.e., correct for the heading bias) caused the shape of $U_{\perp,x,z}^{V2}$ versus time to change, because the aircraft heading varied as a function of time. The shape of the v2 wind as a function of time agrees more closely with the shape of the NAM4 perpendicular wind field. However, the v2 perpendicular wind speed was consistently slower compared to NAM4. The v3 perpendicular wind speed (found as described in section 2.5.2) shows excellent agreement with the NAM4 wind speed, retaining the same shape versus time as the v2 wind. Table S2.1 documents the root mean square error (RMSE) between the NAM4 perpendicular wind field and the three versions of the aircraft wind field. The v3 wind field displays either the smallest (all flights except

UMD RF6) or nearly the smallest (UMD RF6) value of RMSE relative to the NAM4 perpendicular wind.

Figure S2.11 shows a comparison between the emission rate of CO_2 for two local power plants, Chalk Point (CP) and Morgantown (MT), from the CEMS record (see Figure 2.6 for a detailed description) versus the emission rate of CO_2 derived from the v1, v2, and v3 wind fields. Three quantitative metrics for the comparison; i.e., MPE (mean percentage error), MAPE (mean absolute percentage error), and a linear regression of our computed CO_2 emission versus the CEMS value all indicate that the v3 wind field provides the most accurate estimate of the emission rate of CO_2 for the two local power plants. Figure S2.11c is similar to Figure 2.6, except Figure 2.6 also includes data from Purdue RF3 and Purdue RF4.

2.5.4 Uncertainty in the Emission Rate of CO_2 from CEMS records

The uncertainty for CEMS CO_2 emissions (σ_{CEMS}) in Figure 2.6b was determined by combing three independent sources of uncertainty in a root mean sum of error fashion: 1) uncertainty in CEMS records based on the RATA performance specification ($\sigma_{\mathrm{CEMS,\ RATA}}$), 2) the difference of CEMS records against fuel-consumption based EIA datasets ($\sigma_{\mathrm{CEMS,\ EIA}}$), and 3) the uncertainty in the air transport time (between the power plant and aircraft) estimated using HYSPLIT back trajectories ($\sigma_{\mathrm{CEMS,\ Transport}}$).

First, $\sigma_{\mathrm{CEMS,\ RATA}}$ is determined based upon the main performance specification values described in the Relative Accuracy Test Audit (RATA). The RATA is the periodical comparison test of CEMS against the concurrent measurements made by the

EPA reference method (USEPA, 2009). The value of $\sigma_{\text{CEMS, RATA}}$ was found by propagating the relative accuracy of 10% for concentration and volumetric flow rate measurements into the CO_2 mass emission rate calculation equation shown in Table 6 of USEPA (USEPA, 2009).

Second, $\sigma_{\text{CEMS, EIA}}$ was considered because Gurney et al. (2016) found that monthly CO_2 emissions in facility CEMS records (stack measurements based estimates) differ by more than ±13% compared to those in EIA datasets (fuel consumption based estimates) for about one-fifth of U.S. power plants. Quick & Maryland (2019) identified and corrected systematic errors in either the U.S. EPA CAMD (Clean Air Markets Division) or the U.S. EIA (Energy Information Administration) datasets (i.e., unreported unit emissions in the CAMD dataset and emission factor error in the EIA dataset). We confirmed from Quick & Marland (2019) that the CAMD dataset for the CP and MT power plants are not affected by unreported unit emissions. Further, we compared CO_2 emissions for CP and MT from the CAMD data against corresponding EIA data for February 2015. For the CP power plant, the monthly CO_2 emission for Feb 2015 in CAMD is 4% greater than in EIA. For the MT power plant, the emission for Feb 2015 given by CAMD is 8% lower compared than that provided by EIA. While such differences could be caused by errors in either the CAMD or EIA estimate, we used our computed difference values of – 4% and 8% as σ_{CEMS}, EIA for the CP and MT power plants, respectively.

Finally, the value of $\sigma_{\text{CEMS, Transport}}$ was determined as the standard deviation of the CEMS hourly CO_2 emissions within ± 1 hour (i.e., 3 hours span) from our baseline estimate of the transport time from the power plant stack to the aircraft. The baseline

plume transport time was estimated using HYSPLIT back trajectories run with NAM12 meteorology.

2.5.5 Emissions of CO_2 from human and pet respiration and NFA-CO_2 sources and uncertainty propagation

To estimate emissions of CO_2 from respiration by humans and pets, we adopted a similar approach to Gurney et al. (2017). A value of 254 gC/person/day was used as the average CO_2 release rate by human respiration (Prairie & Duarte, 2007). The population of the Balt-Wash area for 2015 was estimated as 8,153,000 based on GPWv4 (Gridded Population of the World) data. Emissions of CO_2 from dog and cat respiration were also estimated assuming that the study area follows the average U.S. per capita ownership of 0.22 dogs/person and 0.24 cats/person, and a dog/cat release rate of CO_2 of 25% of the human release rate (American Veterinary Medical Association, 2012).

Once the human/pet respiration estimate for the emission of CO_2 (~2,000 mol/s) was subtracted from the mass balance estimate for each flight, 4.7% of the remaining CO_2 mass balance emission estimate was apportioned to anthropogenic sources other than the combustion of fossil fuel (i.e., Non-Fossil fuel Anthropogenic CO_2, or NFA-CO_2). According to the MDE GHG inventory, 4.7% of the total in-state emissions of CO_2 are from the following sectors: 1) industrial processes (cement manufacture, limestone and dolomite, soda ash, ammonia and urea production), 2) agriculture (urea fertilizer usage), 3) waste management (waste combustion, landfills, and residential

open burning) (MDE, 2016). The MDE estimates are based on annual emissions for 2014; the 4.7% value was adopted, unchanged, for February 2015.

The uncertainty range of the FLAGG-MD monthly total $FFCO_2$ estimate was determined by propagating four independent sources of uncertainty: 1) uncertainty in the mass balance estimate ($\sigma_{\text{mass-balance}}$), 2) uncertainty in the human/pet respiration estimate ($\sigma_{\text{human/pet-respiration}}$), 3) uncertainty in the ratio of NFA-CO_2 to total CO_2 ($\sigma_{\text{NFA-CO2}}$), and 4) uncertainty in the temporal scaling factor used to relate our seven mass balance estimates to the monthly total emission of CO_2 ($\sigma_{\text{temporal-scaling}}$). First, $\sigma_{\text{mass-balance}}$ was determined from a Monte Carlo simulation by propagating the uncertainties of five parameters that enter the mass balance equation (see Table 2.2). Second, $\sigma_{\text{human/pet-respiration}}$ was specified to be ±30%, based on a conservative estimate in how local pet ownership might vary relative to the national averaged. Given the preponderance of dogs and cats in the Balt-Wash region and the lack of large-scale animal feedstock, emissions of CO_2 from animals other than human, dog, and cat should be well covered by this ±30% value. Third, $\sigma_{\text{NFA-CO2}}$ was determined to be ±1.5%, based upon as the standard deviation of three NFA-CO_2 ratios derived from MDE GHG inventory for year 2006, 2011, and 2014. Finally, $\sigma_{\text{temporal-scaling}}$ was determined to be 0.4%, based upon the standard deviation of three temporal scaling factors from FFDASv2.2, TIMES, and ACESv1.

2.5.6 Bottom-up gridded emissions products: Discrepancies and harmonizing efforts

FFDASv2.2 consists of the downscaled IEA estimate of fossil fuel combustion emissions and the EDGAR (Emissions Database for Global Atmospheric Research)

version 4.3.2 estimate of aviation and shipping emissions. FFDASv2.2 data files did not provide any sector specific emissions. In Figure 2.9, the $FFCO_2$ value from FFDASv2.2 was directly derived from hourly NetCDF data files available at http://ffdas.rc.nau.edu.

EDGARv432 monthly data for year 2010 consists of source sectors specified by IPCC, as detailed in Table S4 of Janssens-Maenhout et al. (2017). In Figure 2.9, the $FFCO_2$ value of EDGARv432 consists of the following sectors: Power Industry, Energy for Buildings, Combustion for Manufacturing Industry, Road Transportation, Aviation (landing & take off, climbing & descending, and cruise), Shipping and Railways, Pipelines, and Off-Road Transport. The $FFCO_2$ value was calculated solely from the long cycle C (file name: "CO2_excl_short-cycle_org_C") to be consistent with our other estimates of $FFCO_2$. In Figure 2.9, the "ELEC" label of the EDGARv432 indicates emissions from the Power Industry sector. The "RCI" label consists of the Energy for Buildings and the Combustion for Manufacturing Industry sectors. The "Onroad" label indicates the Road Transportation sector, and the "Nonroad" label consists of emissions from the Aviation, Shipping, and Off-Road Transport sectors.

The ACESv1 data for year 2014 consist of emissions from the following sectors: Residential, On-Road Transportation, Oil and Gas Production, Off-Road Vehicles/Marine/Rail, Non-Electricity Generating Facilities, Electricity Generating Facilities, Airport, and Industrial and Commercial. In Figure 2.9, the $FFCO_2$ value of ACESv1 consists of all of the sectors listed above. The "ELEC" label for ACESv1 denotes emissions from the Electricity Generating Facilities sector. The "RCI" label consists of the Residential, Industrial and Commercial, and Non-Electricity Generating

Facilities sectors. The "Onroad" label indicates emissions from On-Road Transportation, whereas the "Nonroad" label combines emissions from the Airport and the Off-Road Vehicles/Marine/Rail sectors. The total emissions of CO_2 for 2014 from ACESv1 are held constant to that for their year 2011 analysis, but re-distributed based on variations in meteorology, fuel consumption, and traffic patterns between these two years (Gately & Hutyra, 2018).

ODIAC2018 data consists of two emission categories: emissions over land (variable name: "land") and emissions from international aviation and marine bunkers (variable name: "bunker"). The land sector consists of emissions from fossil-fuel combustion, cement manufacturing, and gas flaring. The bunker sector was only available on a 1×1° lat/lon grid provided via NetCDF data files, while the land sector was available on both 1×1 km spatial grid via GeoTIFF files and the 1×1° grid via NetCDF files. In Figure 2.9, the $FFCO_2$ value from ODIAC2018 consists of both land and bunker sectors. The land emissions were obtained from the 1×1 km data file. For bunker emissions, the ratio of bunker to land emissions for our study domain was calculated using data from both 1×1° files, and the ratio was multiplied by the land emissions computed using data from the 1×1 km file. In Figure 2.9, the "Nonroad" label for ODIAC2018 indicates emissions from the bunker sector. Note that the $FFCO_2$ values marked by the "Nonroad" label for ACESv1 and EDGARv432 consist of not only aviation and bunker emissions, but also the off-road vehicle and rail sectors.

The MDE GHG inventory for year 2014 Microsoft Excel data file consists of various sources sectors (including imported electricity) and sinks of GHG. The state-wide annual total $FFCO_2$ was calculated as the sum of emissions from following

sectors: In-state Energy Production (coal, natural gas, and oil), Residential/Commercial/Industrial Fuel Use (coal, natural gas & LPG, petroleum), Transportation (on-road gasoline & diesel, nonroad gasoline & diesel, rail, marine vessels, lubricants & natural gas & LPG, and jet fuel & aviation gasoline), and Fossil-Fuel Industry (natural gas industry). Emissions from the following sectors were summed to calculate NFA-CO_2 (Non-Fossil fuel Anthropogenic CO_2): industrial processes (cement manufacture, limestone & dolomite, soda ash, and ammonia & urea production), agriculture (urea fertilizer usage), and waste management (waste combustion, landfills, and residential open burning).

Several sector mismatches exist for $FFCO_2$ derived from the five bottom-up inventory datasets. First, FFDASv2.2 does not cover the cement manufacturing and gas flaring sectors (CM&GF). The EDGARv432 and MDE inventories cover CM&GF, but we excluded these sectors when calculating $FFCO_2$. The ACESv1 and ODIAC2018 datasets cover CM&GF, but these two sectors could not be isolated from other $FFCO_2$ sectors in the data files provided by these two groups. Therefore, emissions of CO_2 from the CM&GF sectors remain the bottom-up inventories from ACESv1 and ODIAC2018. According to the MDE inventory, the CM&GF sectors emitted 0.4 MtC during year 2014, which is about 2% of the state-wide annual total $FFCO_2$ estimate.

Second, EDGARv432, FFDASv2.2, and ODIAC2018 cover both the aircraft landing & takeoff sector as well as the airborne aircraft emissions sector, while ACESv1 only covers the aircraft landing & takeoff sector. Note that the aircraft emissions sector of FFDASv2.2 was directly adopted from EDGAR. The MDE inventory estimate of aviation emissions was based on aviation fuel consumption

statistics, and thus does not necessarily indicate emission within the geographical boundary of the state. According to EDGARv432, airborne aircraft emissions ("TNR_Aviation_CDS/CRS") emitted 0.05 MtC during February 2010, which is again about 2% of the monthly total $FFCO_2$ estimate. According to the MDE inventory, emissions from the jet fuel & aviation gasoline usage constitute about 1% of the state-wide annual total $FFCO_2$ emission inventory.

Finally, FFDASv2.2 does not cover emissions from the oil and natural gas refining and transformation sectors. Emissions provide by ODIAC2018 and ACESv1 do cover these sectors. Emissions of CO_2 from oil and natural gas refining and transformation could not be isolated from emissions of CO_2 from the more dominant combustion sectors for ODIAC2018, whereas according to ACESv1 there was no CO_2 emitted from these oil and gas sectors in our study domain.

EDGARv432's oil refineries and transformation industry sector (file name: "REF_TRF") and fuel exploitation sector (file name: "PRO") denote emissions from these oil and gas sector; non-combustion emissions of CO_2 are also provided in these files. Since FFFASv2.2 does not cover the oil and gas sector emissions provided by these "REF_TRF" and "PRO" files of EDGAR, these emissions were excluded from $FFCO_2$ of EDGARv432 shown in Figure 2.9. The MDE inventory does include emissions from pipeline fuel combustion within the natural gas industry sector; these emissions are included in the calculation of $FFCO_2$ from MDE discussed in section 2.3.8. According to MDE, only 0.0001 MtC of CO_2 was emitted from the oil and gas sector in year 2014 (including pipeline fuel combustion), which is less than 0.001 % of the total annual value of $FFCO_2$.

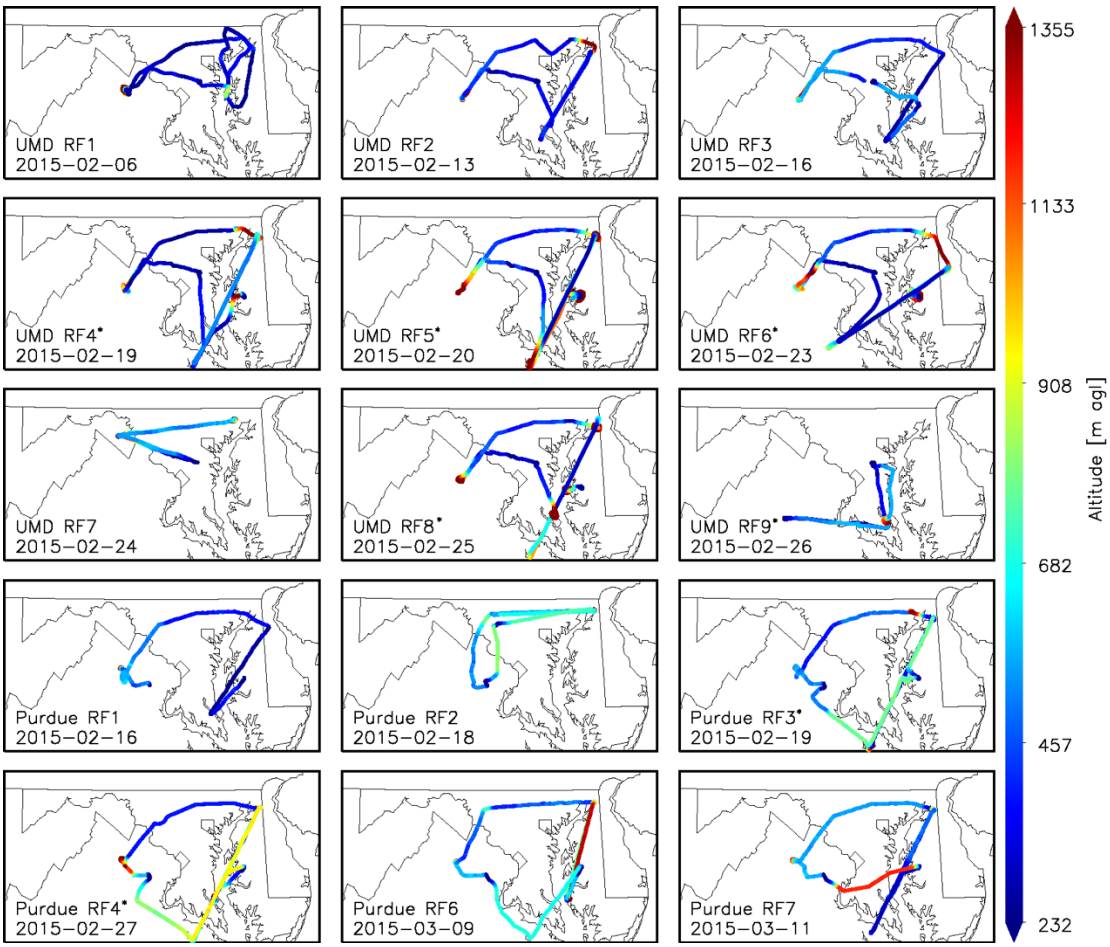

Figure S2.1. Flight tracks of the 15 research flights conducted during the winter 2015 FLAGG-MD campaign. A total of nine flights were conducted by the UMD aircraft and six flights were conducted by the Purdue aircraft. The date of each research flight is shown at the bottom left of each panel, in a year-month-day format. The asterisk (*) symbol next to each RF number indicates that in-situ data of that flight was used for the mass balance estimate of the emission of CO_2 from the Balt-Wash area within our study.

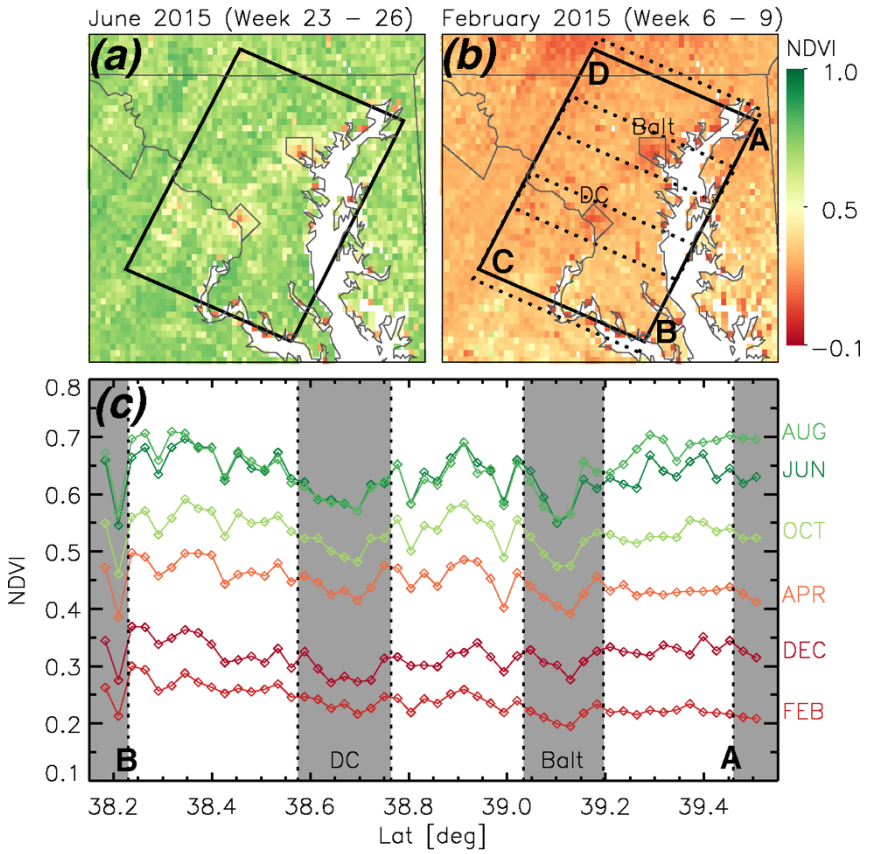

Figure S2.2. Normalized Difference Vegetation Index (NDVI) for (a) June 2015 and (b) February 2015. The v1r12 weekly NDVI data on a 4 km×4 km grid from the Visible Infrared Imaging Radiometer Suite (VIIRS) is available from the following link: https://www.star.nesdis.noaa.gov/smcd/emb/vci/VH/index.php. Data for February 2015 are used in the analysis; measurements for June 2015 are shown to illustrate that the VIIRS determination of NDVI is more sensitive to the rural/urban setting during summer than winter. Points A, B, C, and D as well as the rectangular box denoting our study area are the same as used in Figure 2.1. (c) Averages of NDVI along a series of diagonal boxes that extend from just south point B and just north of point A on panel (b), plotted as a function of the middle latitude of each box along line AB (called as "horizontal transect"). The most southerly box and the most northerly box correspond to "edge areas" used to define background CO_2 for six of the seven mass balance flights. The latitudinal span of these boxes, as well as the latitudinal span of Washington, D.C. (DC) and the city of Baltimore (Balt), are shown by the grey shaded regions. Results for NDVI are shown for six months in 2015, as indicated. The slight decline in NDVI for DC and Balt for Feb 2015 is used to scale the results of the biogenic emission of CO_2 computed by the VEGAS model.

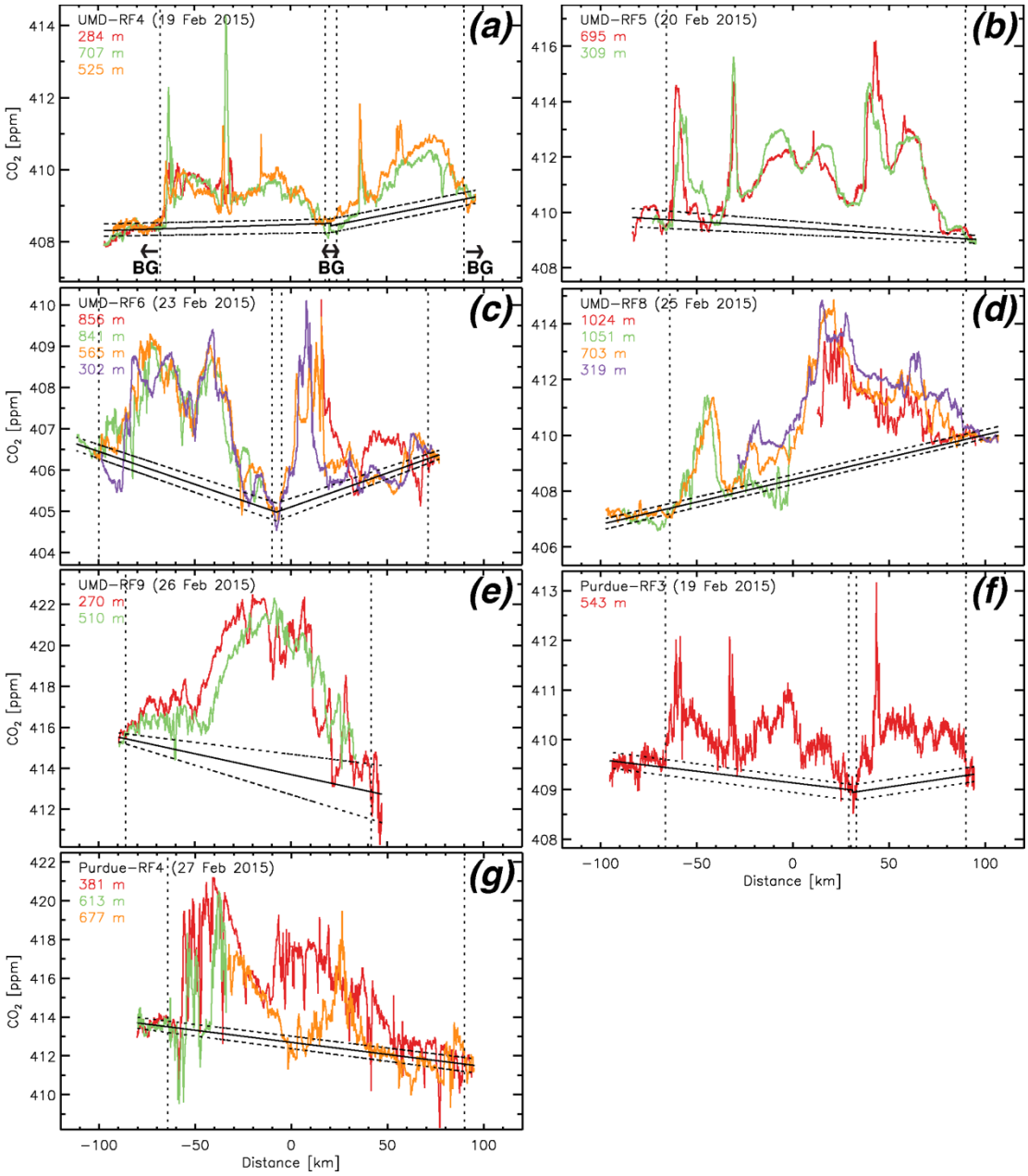

Figure S2.3. (a-g) Mole fraction of CO_2 measured downwind of the Balt-Wash area (colored) and the background CO_2 (black, solid) for the seven mass balance flights. Each colored line indicates downwind horizontal transects at different altitudes. The flight date and the mean altitude of each horizontal transect is shown at the left-top of each panel. The black solid lines indicate background CO_2 used to estimate the emission rate of CO_2; the black dotted lines indicate the $\pm 1\sigma$ bound of background CO_2 used for the sensitivity analysis. Dotted vertical lines indicate the boundaries of flight segments used to define the values of background CO_2.

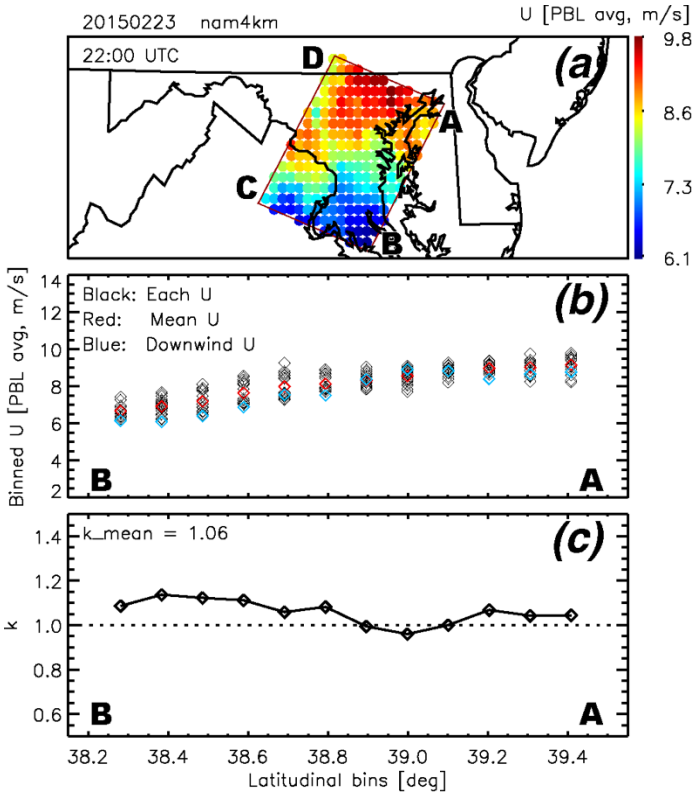

Figure S2.4. (a) Map showing the average value of U within the PBL ($\overline{\boldsymbol{U_{PBL}}}$) derived from NAM4 for every cell on the 0.1°×0.1° lat/lon grid. (b) Same $\overline{\boldsymbol{U_{PBL}}}$ data shown in (a) but binned in 0.1° diagonal latitudinal bins (see Figure 2.7). For each diagonal latitudinal bin, the black diamonds indicate $\overline{\boldsymbol{U_{PBL}}}$ from each grid 0.1°×0.1° NAM4 grid point that lies within the bin. The red diamond indicates the mean value of $\overline{\boldsymbol{U_{PBL}}}$ within the diagonal bin (i.e., the average of the black diamonds. The blue diamond indicates $\overline{\boldsymbol{U_{PBL}}}$ for the NAM4 grid located closest to the downwind portion of the study area (i.e., line AB in Figure 2.1). (c) Black diamonds indicate the scaling factors *k* derived for each latitudinal bin, and the black line indicates the linearly interpolated scaling factor applied to wind measurements for the mass balance calculation.

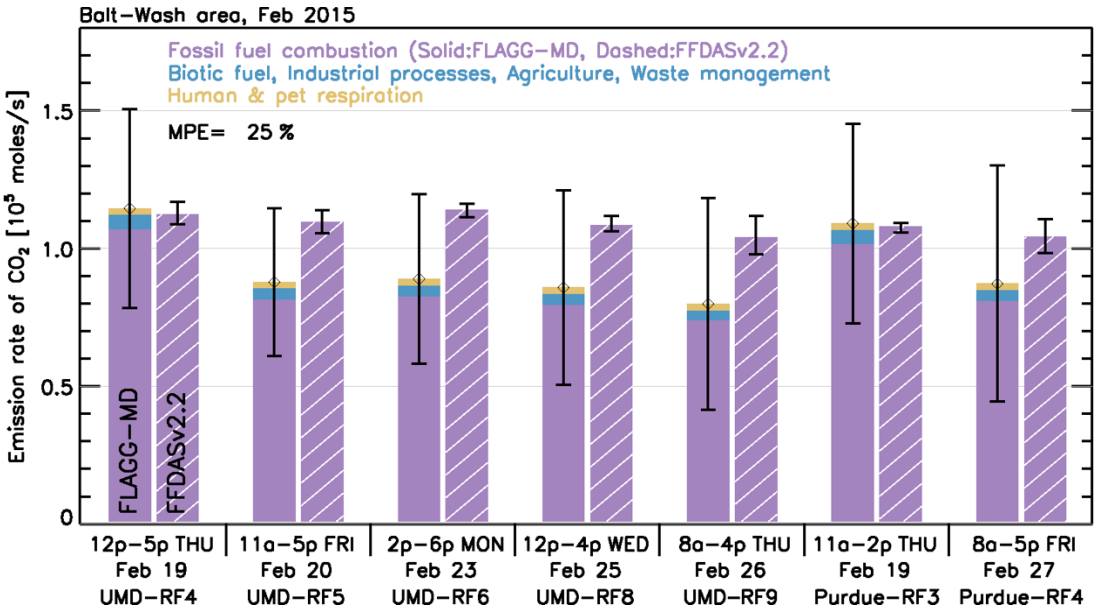

Figure S2.5. The emission rates of CO_2 from the Balt-Wash area during the sampling period for seven research flights conducted in February 2015. This figure is identical to Figure 2.8, except here we have computed the FLAGG-MD mass balance emissions assuming a value of unity for the scaling factor k described in section 2.2.7. In other words, here we assume the wind speed perpendicular to the aircraft flight track was steady during the transport time over the Balt-Wash area (i.e., $k = 1$ in Equation 2.1). Overall, the FLAGG-MD fluxes shown here are 5% larger than those shown in Figure 2.8.

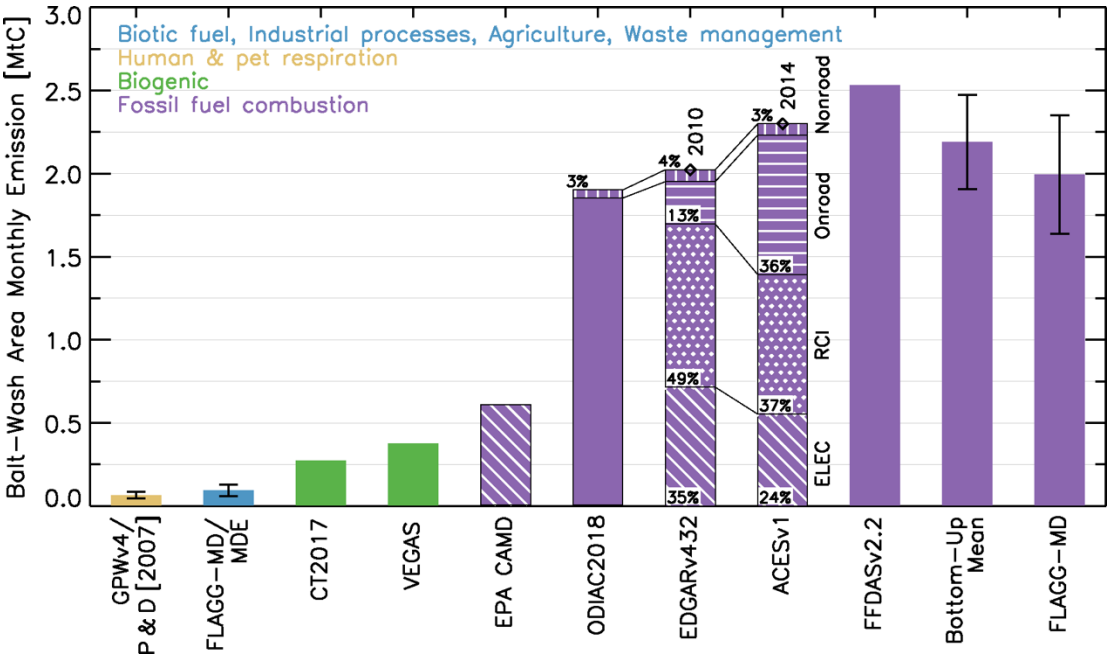

Figure S2.6. Emissions of CO2 from the Balt-Wash area during February 2015. This figure is identical to Figure 2.9, except here we have again computed the FLAGG-MD emissions assuming $k = 1$ in Equation 2.1 (i.e., steady perpendicular winds across the study area). The FLAGG-MD monthly emission shown here (last vertical bar) is 5% larger than that shown in Figure 2.9.

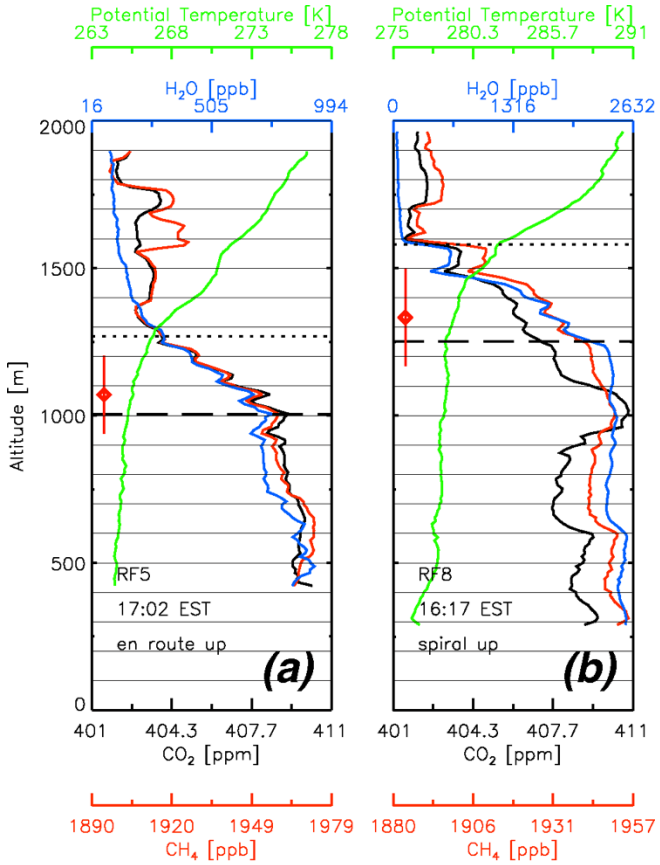

Figure S2.7. Vertical profiles of CO_2, CH_4, H_2O and potential temperature downwind of the Balt-Wash area on (a) 20 February 2015 (UMD-RF5) and (b) 25 February 2015 (UMD-RF8). The locations of these vertical profiles are indicated as VP3 and VP5 in Figure 2.1. The dashed line represents the top of the well-mixed PBL. The dotted line represents the entrainment height. The red diamond and vertical error bar indicate the adjusted mixing height and its 1σ uncertainty range, used for the flux estimation in Equation 2.1.

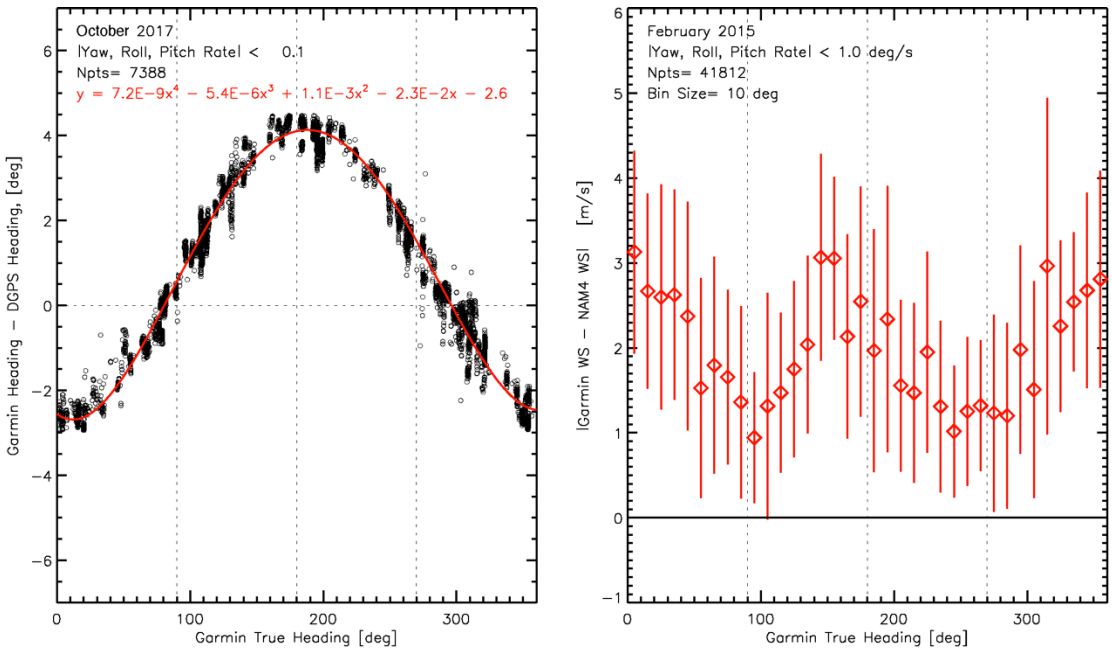

Figure S2.8. (a) The difference of true heading measurements obtained by the Garmin system and the Differential GPS (DGPS) during four calibration research flights conducted in October 2017. (b) The difference of v1 wind speed derived from the Garmin output and NAM4 sampled along the flight track as a function of the Garmin true heading, during eight UMD research flights conducted in February 2015.

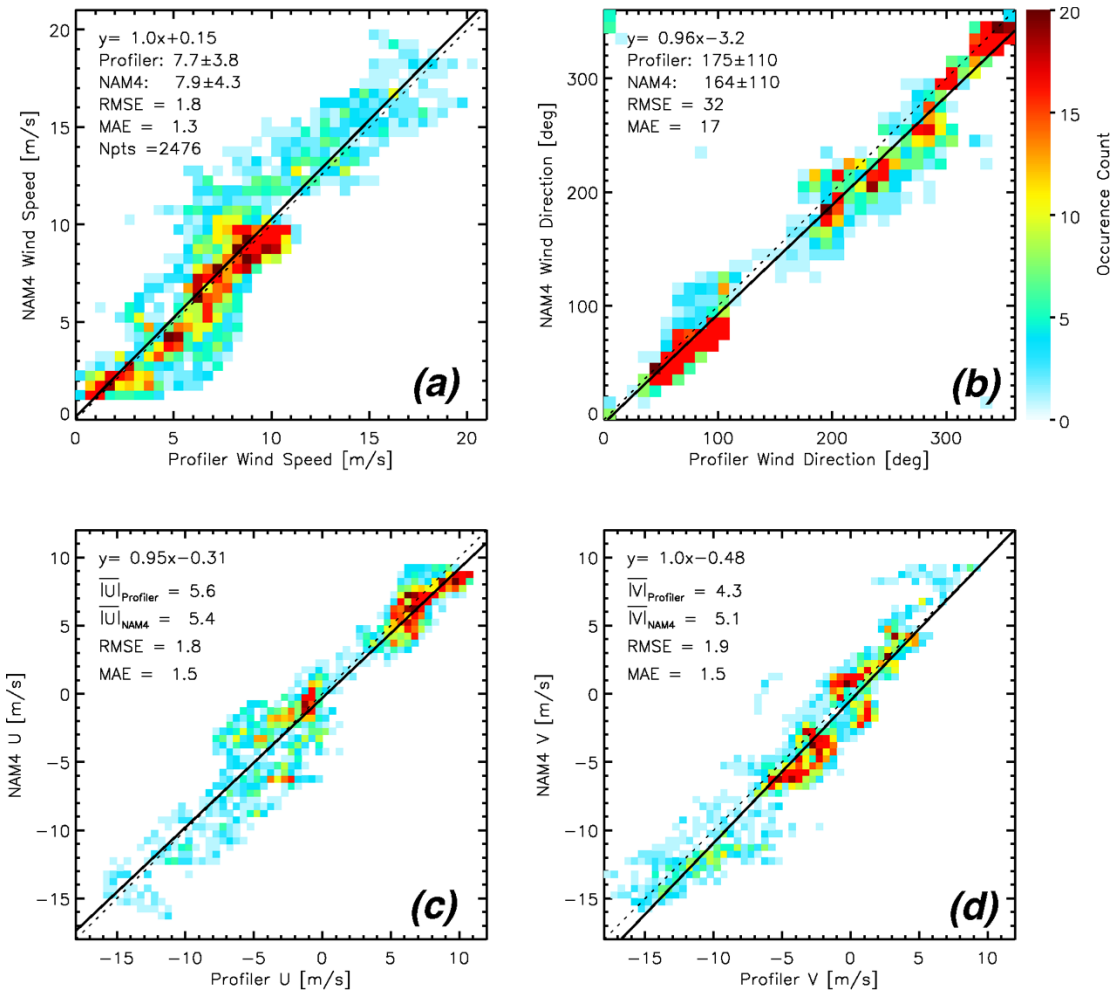

Figure S2.9. Scatter plots comparing the Beltsville site wind profiler measurements and the NAM4 meteorological model for (a) wind speed, (b) wind direction, (c) U component, and (d) V component wind. Dotted line indicates 1 to 1 ratio line and solid line indicates the linear regression fitted to the data. The data plotted were obtained during the eight flight days during the campaign (i.e., 13, 16, 19, 20, 23, 24, 25, and 26 February 2015).

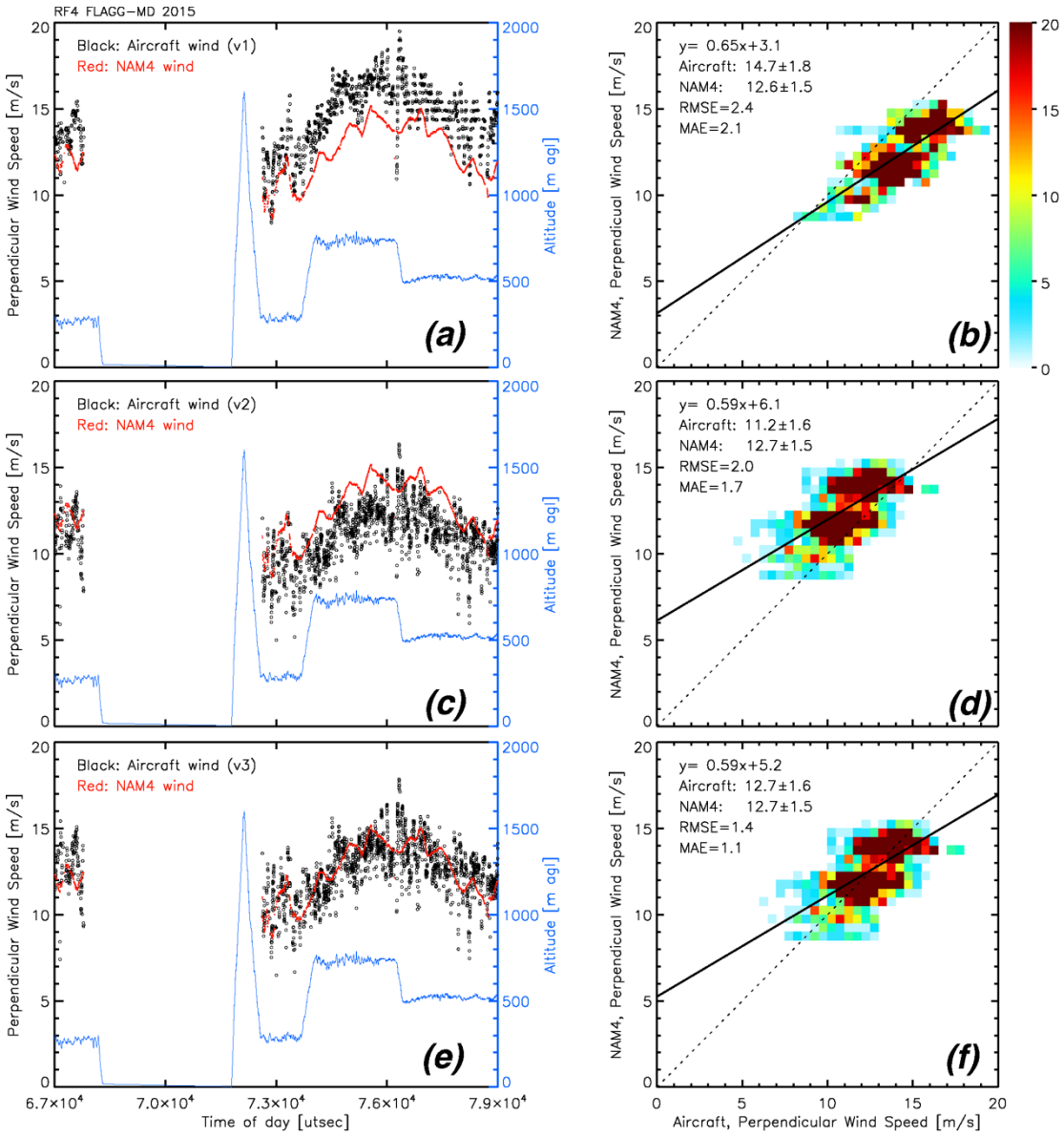

Figure S2.10. Comparisons between three versions of the aircraft wind perpendicular to the aircraft flight track and the perpendicular wind from NAM4. For each row, the left and right plots showing the same data, but as time series and scatter plots, respectively. The first row shows the comparison for the original v1 aircraft perpendicular wind. The second row shows the comparison for the v2 aircraft wind, which incorporates the magnetic heading bias correction and true airspeed calibration described in section 2.5.1 - 2.5.3. The third row shows the comparison for the v3 aircraft wind, which is derived by scaling the perpendicular wind speed to the NAM4 data, as described in section 2.5.2.

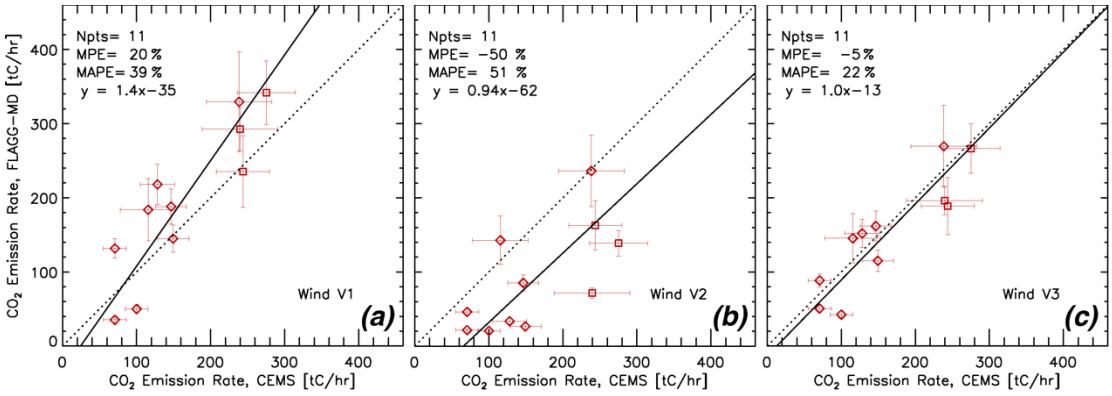

Figure S2.11. Scatter plots of the emission rate of CO_2 from the CEMS record of Chalk Point (CP) and Morgantown (MT) power plants versus the emission rate of CO_2 estimated using (a) v1 wind, (b) v2 wind, and (c) v3 wind fields of the UMD Cessna aircraft. The data points shown in (c) are identical to the UMD data points shown in Figure 2.6b. The mean percentage error (MPE) and the mean absolute percentage error (MAPE) of the UMD mass balance versus CEMS emissions are shown at the top left of each panel. The dotted line shows the 1 to 1 ratio and the solid line shows a linear least square fit of the data points, for each version of the wind field. The close agreement of the linear fir on panel (c) to the 1 to 1 line supports the validity of the v3 wind field.

Table S2.1. The mean and the standard deviation of the three different versions of the aircraft perpendicular wind speed. The root mean square error (RMSE) of the perpendicular wind speed against the corresponding the NAM4 wind data are shown.

Unit: m/s	Date 2015	Wind v1		Wind v2		Wind v3	
		$U_\perp \pm 1\sigma$	RMSE	$U_\perp \pm 1\sigma$	RMSE	$U_\perp \pm 1\sigma$	RMSE
UMD-RF1	Feb 6	7.4±3.1	3.1	5.1±3.2	2.8	5.3±3.2	2.8
UMD-RF3	Feb 16	5.4±1.0	2.1	2.3±1.0	1.3	3.4±1.0	0.7
UMD-RF4	Feb 19	14.7±1.8	2.4	11.2±1.6	2.0	12.7±1.6	1.4
UMD-RF5	Feb 20	7.2±1.6	1.5	3.4±1.5	2.9	6.1±1.5	1.0
UMD-RF6	Feb 23	11.1±1.3	1.4	8.5±1.4	2.6	10.6±1.4	1.5
UMD-RF8	Feb 25	6.7±2.2	2.4	2.9±1.9	2.8	5.1±1.9	1.7
UMD-RF9	Feb 26	3.7±1.2	1.2	3.5±1.1	1.1	4.1±1.1	1.0

Chapter 3: Emissions of CO_2 and CO in the Baltimore, MD-Washington, D.C. area: Lessons learned from aircraft campaign during COVID-19 pandemic

3.1 Introduction

Cities account for 70% of global energy consumption (O'Shaughnessy et al., 2016). Fossil-fuel combustion in the world's cities (i.e., residential, commercial, industrial, transportation) produces a significant portion of global air pollutants that are detrimental to climate and air quality. According to UN-Habitat (2011), cities account for more than 70% of global CO_2 emissions. Cities and local governments across the globe have set various climate plans to reduce the emission of greenhouse gases (GHGs) (C40, 2019). For example, the state of Maryland is in on track to achieving the target of reducing emissions of GHGs 40% by year 2030, relative to the 2006 emission level (Maryland Department of the Environment (MDE), 2021). Washington D.C. has also set a climate action plan to reduce the emission of GHGs by 50% below 2006 levels by year 2032, and by 80% in 2050 (Department of Energy & Environment (DOEE), 2018).

Many states and cities rely on self-generated bottom-up emission inventories to track progress on their GHG emission reduction plans (Kevin Robert Gurney et al., 2021). Even though the methodology underlying detailed inventories vary, the bottom-up approach estimates emissions by combining activity metric data (i.e., fossil-fuel consumption) and corresponding emission factors (i.e., carbon content of specific fuel,

combustion efficiency) for various source sectors (Liu et al., 2020). Any inaccuracy in activity metric data or emission factors propagates into the uncertainty of bottom-up inventories (McDonald et al., 2018). Conversely, the top-down approach constrains emissions based upon analysis of atmospheric observations of GHGs from various platforms (i.e., ground, aircraft, satellite). Various top-down analysis methods exist, such as the mass balance approach (Ahn et al., 2020; Heimburger et al., 2017; Klausner et al., 2020; X. Ren et al., 2018; Ryoo et al., 2019), the inversion framework (Balashov et al., 2020; Cusworth et al., 2020; Lopez-Coto et al., 2020; Michalak et al., 2017; Staufer et al., 2016), or the trace gas ratio method (Ammoura et al., 2016; Goldberg et al., 2019; Plant et al., 2019; X. Ren et al., 2018; Wong et al., 2016). One of the major challenges in the top-down approach is to attribute observed emissions to specific source sectors (i.e., transportation vs residential/commercial/industrial sector) (Miller & Michalak, 2017).

The Severe Acute Respiratory Syndrome Corona Virus 2 (SARS-CoV-2 or COVID-19) pandemic affected human activities worldwide. In the United States, various social activity regulations were issued starting in March 2020. On 16 March 2020, Maryland and D.C. governments ordered the closure of restaurants and other recreational facilities to slow the spread of COVID-19 (NGA, 2020). Abrupt changes in the emission of GHGs from various sources sectors (i.e., transportation, residential, commercial, power) have been reported, with varying magnitudes for each sector (EIA, 2020b; Laughner et al., 2020; Le Quéré et al., 2020). Here, we will examine the accuracy of several of these bottom-up emission inventories by comparing to results based upon airborne observations analyzed using the top-down method.

The University of Maryland, Purdue University, and the National Oceanic and Atmospheric Administration (NOAA) conducted a series research flights from February to May 2020. These flights focused on the measurement of the outflow of atmospheric pollutants from cities along the U.S. North East Corridor. The acquisition of these atmospheric in-situ observations during the pandemic, for which abrupt changes in various source sector emissions were occurring, provides an unprecedented opportunity to study the effect of COVID19 on air pollutant emissions from the Baltimore-Washington D.C. (Balt-Wash) region.

In this study, we quantify the emission of CO_2 from the Balt-Wash area during the COVID-19 pandemic. We also quantify the emission of carbon monoxide (CO), a byproduct of incomplete combustion and one of the six criteria air pollutants regulated under the National Ambient Air Quality Standards (NAAQS) (EPA, 2010). In section 3.2.1 to 3.2.3, we describe the aircraft-based top-down approach used to estimate the emissions of CO_2 and CO. In section 3.2.4, we describe how we combine the top-down and bottom-up approach to conduct source sector attribution. In section 3.3.1, we present the changes in atmospheric distribution of CO_2 and CO over the Balt-Wash area before and after governmental stay-at-home directives issued in response to COVID-19 outbreaks. In section 3.3.2, we quantify the changes in emissions of CO_2 and CO during the COVID-19 pandemic period. In section 3.3.3, we evaluate three bottom-up inventories, using our top-down estimates of the emissions of CO_2 and CO.

3.2 Materials and Methods

3.2.1 Aircraft Research Flights during the COVID-19 pandemic

The University of Maryland (UMD) conducted six research flights in February 2020 as a part of the Fluxes of Greenhouse Gases in Maryland (FLAGG-MD) campaign, which aims to quantify GHG emissions from the Balt-Wash area. On 30 March 2020, formal stay-at-home orders were issued for the District of Columbia, Maryland, and Virginia areas due to the spread of COVID-19 (NGA, 2020). In April 2020, a series of coordination calls were conducted among the UMD, Purdue University (Purdue), and the National Oceanic and Atmospheric Administration (NOAA) flight panning teams. Although coordinated, the UMD, Purdue, and NOAA teams conducted research flights designed to independently investigate the impact of COVID-19 on the air pollutions from the major cities in the U.S. North East corridor. In this study, we focus on airborne measurements over the Balt-Wash area obtained from the UMD Cessna and the NOAA Twin Otter aircraft. Figure 3.1 shows flight tracks of UMD and NOAA aircraft conducted during February (red lines), April (green lines), and May 2020 (blue lines).

The UMD research aircraft Cessna 402B was equipped with a Picarro cavity ring-down spectroscopic (G2401-m) to measure the dry air mole fraction of CO_2 and CO. Measurements of CO_2 were calibrated on the ground and during the flight using an onboard calibration system with two cylinders of trace gases certified by NIST. The UMD aircraft is also equipped with instruments to measure other trace gases (i.e., NO, NO_2, SO_2, O_3), aerosol optical properties (black carbon, scattering, absorption coefficients), and meteorological variables (temperature, pressure, wind speed, wind direction, relative humidity). The complete list of instrumentations onboard the UMD research aircraft is described in Ren et al. (2018). The NOAA Twin Otter aircraft (De Havilland DHC-6-300) was equipped with a Picarro Cavity Ringdown Spectrometer

(G2401-m) to measure CO_2, CO, CH_4 and water vapor. Also, the Twin Otter aircraft was equipped with the Rosemount ambient sensor to record temperature and pressure and the wind probe along with differential GPS to record wind information (Conley et al., 2014). Further details of the instrumentation setup on the NOAA Twin Otter aircraft are given in Text S1 of Plant et al. (2019).

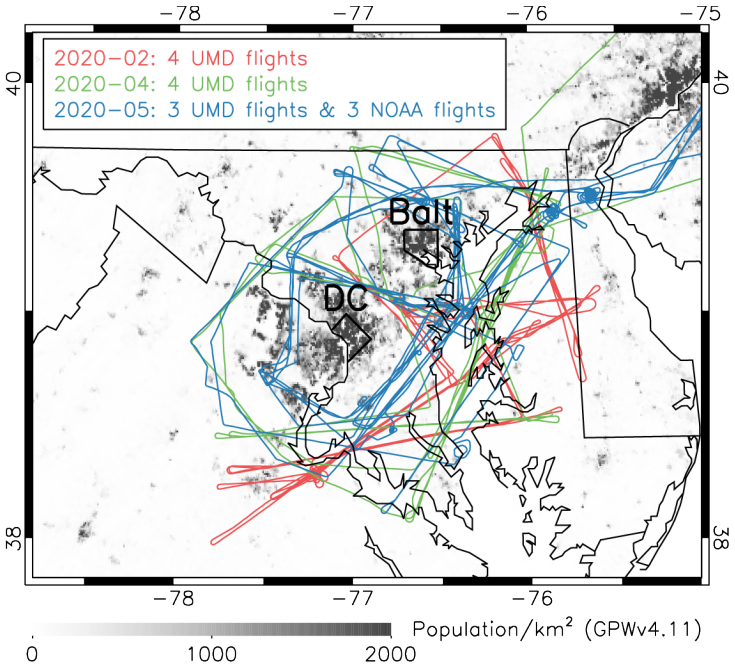

Figure 3.1. Aircraft research flight tracks conducted in the Baltimore, MD-Washington, D.C. metropolitan areas during February (red), April (green), and May (blue) of 2020. The upper left box shows the number of UMD and NOAA flights used to calculate the emission rate of CO_2 and CO in this study (flight dates are shown in Table 3.1). The gray-scale over the geographical domain indicates population density from the Gridded Population of the World (GPWv4.11, CIESIN (2018)). The aircraft footprint area covered by each flight is shown in Figure S3.1.

3.2.2 Aircraft-based Mass Balance Approach

The mass balance approach estimates the emission rate of trace gases from aircraft observations, based upon the principle of mass conservation within a geographical area of interest (Trainer et al., 1995; White et al., 1983). The aircraft-based mass balance method has been widely used to estimate greenhouse gas emissions

in urban areas, including Indianapolis (Cambaliza et al., 2014; Heimburger et al., 2017; Mays et al., 2009), Sacramento (Ryoo et al., 2019; J C Turnbull et al., 2011), London (Ashworth et al., 2020; O'Shea et al., 2014; Pitt et al., 2019), Berlin (Klausner et al., 2020), and the Balt-Wash area (Ahn et al., 2020; X. Ren et al., 2018). The two previous studies focused on Balt-Wash, Ahn et al. (2020) and Ren et al. (2018), quantified emissions of CO_2, CO, and CH_4 during the winter of 2015 and 2016.

Here we compute the emission rate of CO_2 and CO over the Balt-Wash area with the following equation:

$$F = \int_{z_i}^{z_f} \int_{x_i}^{x_f} \left([C]_{x,z} - [C_{bg}]_{x,z} \right) \cdot U_{x,z} \, dxdz \qquad (3.1)$$

where x is the horizontal distance and z is the vertical coordinate in the aircraft transect downwind of the Balt-Wash area. Variables x_i, x_f and z_i, z_f are the horizontal and vertical bounds of the downwind transect influenced by the emission source of interest. We determine z_f using the same method in Ahn et al. (2020) with the following equation: $z_f = (3z_{well\text{-}mixed} + z_{entrainment}) / 4$. Variable $z_{well\text{-}mixed}$ is the well-mixed planetary boundary layer (PBL) height and $z_{entrainment}$ is the entrainment height where mixing from the PBL has reached the level of the free troposphere. Both $z_{well\text{-}mixed}$ and $z_{entrainment}$ are determined from the vertical profiles of potential temperature and mole fractions of the trace gases CO_2, CO, CH_4, and H_2O. Variable U denotes the wind speed perpendicular to the aircraft heading, variable $[C]$ represents the observed number density of a specific trace gas (i.e., CO_2 and CO), and $[C_{bg}]$ is the computed background number density of the trace gas of interest. We adopt the linear regression method of Ahn et al. (2020) to determine the background mole fraction of trace gas: a least squares linear regression line is fit to the mole fraction of trace gas measured at both edges of the

transect. If the mole fraction of the trace gas measured between Washington, D.C., and Baltimore, MD is lower than the mole fraction measured at either edge of the transect, an additional background area is designated approximately midway between Washington, D.C. and Baltimore, MD (Figure S3.2). The mole fractions of each trace gas are converted into number density ([C], [C_{bg}]) using in-situ measurements of temperature and pressure.

3.2.3 Evaluating the impact of biospheric CO_2 uptake on the aircraft-based mass balance approach

The impact of the active biosphere on fluxes of CO_2 found using the aircraft-based mass balance approach varies depending on both magnitude (i.e., seasonal dependence of biospheric CO_2 release or uptake) and spatial variability across the study domain (i.e., urban vs sub-urban). We assess the impact of biosphere by simulating the enhancement signal of urban CO_2 plumes for the following two scenarios:1) only fossil-fuel CO_2 ($FFCO_2$) emissions exist in the study domain ($\Delta F_{Balt-Wash}^{FFCO2}$); 2) both $FFCO_2$ emissions and biospheric CO_2 uptake exist in the study domain ($\Delta F_{Balt-Wash}^{FFCO2+GPP}$). Here, GPP refers to gross primary productivity.

We consider aircraft transects that show the absolute relative difference between $\Delta F_{Balt-Wash}^{FFCO2+GPP}$ and $\Delta F_{Balt-Wash}^{FFCO2}$ greater than 20% to be heavily affected by the biosphere: these aircraft transects are excluded from the mass flux calculation. To simulate the CO_2 enhancement signal, we utilize the following three models: 1) the Hybrid Single-Particle Lagrangian Integrated Trajectory (HYSPLIT) back trajectory estimate of air parcel history (Draxler et al., 2014; Stein et al., 2015); 2) the gridded

gross primary product developed using the solar induced fluorescence (SIF) retrieval from the Tropospheric Monitoring Instrument (TROPOMI) (Turner et al., 2020); 3) the Emissions Database for Global Atmospheric Research version v5.0 (EDGARv50, Crippa et al. (2020)) estimate of the flux of CO_2. Further details on our simulation of the urban enhancement of CO_2 fluxes due to the terrestrial biosphere are given in section 3.5.1. Table S3.1 show our estimates of the $\Delta F_{Balt-Wash}^{FFCO2+GPP}$ and the $\Delta F_{Balt-Wash}^{FFCO2}$ for the 14 research flights used in this study.

3.2.4 Source sector attribution of the emission of CO_2 and CO observed during flights

The abrupt changes in the emissions of CO_2 and CO during the COVID-19 pandemic period provide an opportunity to determine the source sector compositions of CO_2 and CO. The aircraft-based estimates of the CO_2 (or CO) emission rate, computed using Equation 3.1, can be described as the sum of emissions from four source sectors:

$$C_{Feb}^{Total} = C_{Feb}^{RCI} + C_{Feb}^{Onroad} + C_{Feb}^{Nonroad} + C_{Feb}^{ELEC} + C_{Feb}^{Others} \quad (3.2)$$

where the variable C_{Feb}^{Total} represents the emission rate of CO_2 (or CO) over the Balt-Wash area during February 2020. The superscript 'RCI' indicates the Residential/Commercial/Industrial sector, 'Onroad' indicates the onroad transportation sector (i.e., vehicle on roads, highway ramps), 'Nonroad' indicates the nonroad transportation sector (i.e., construction equipment, lawn and garden equipment, commercial marine vessels), 'Elec' is the power sector (i.e., electricity generation), and 'Others' is the sum of other source sectors. Next, the percentage change of the CO_2 (or

CO) emission rate from February to April 2020 can be described as the sum of changes from the four major source sectors plus the category 'Others':

$$\Delta C_{Apr}^{Total} = \left(\frac{C_{Feb}^{RCI}}{C_{Feb}^{Total}} \cdot \Delta A_{Apr}^{RCI}\right) + \left(\frac{C_{Feb}^{Onroad}}{C_{Feb}^{Total}} \cdot \Delta A_{Apr}^{Onroad}\right) + \left(\frac{C_{Feb}^{Nonroad}}{C_{Feb}^{Total}} \cdot \Delta A_{Apr}^{Nonroad}\right) + \left(\frac{C_{Feb}^{ELEC}}{C_{Feb}^{Total}} \cdot \Delta A_{Apr}^{ELEC}\right) + \left(\frac{C_{Feb}^{Others}}{C_{Feb}^{Total}} \cdot \Delta A_{Apr}^{Others}\right), \quad where\ \Delta C_{Apr}^{Total} = \frac{C_{Apr}^{Total} - C_{Feb}^{Total}}{C_{Feb}^{Total}} \cdot 100 \qquad (3.3)$$

where the variable $\Delta C_{Apr-Feb}^{Total}$ is the percentage change of the emission rate of CO_2 or (CO) from February to April 2020. We estimate $\Delta C_{Apr-Feb}^{Total}$ using aircraft observations as described in section 3.2.2. Variable $\Delta A_{Apr-Feb}^{y}$ is the percentage change of activity metric for a source sector *y* (i.e., RCI, Onroad, Nonroad, Elec, Others) from February to April 2020. We determine $\Delta A_{Apr-Feb}^{y}$ from various activity metric data, such as the natural gas consumption by the RCI sector (EIA, 2021a), traffic volume (MDOT, 2020), gasoline/special fuel/aviation fuel sales (Comptroller of Maryland, 2020), and power plant operational data (EPA, 2020a). Table S3.2 provides the complete list of metric data used to determine ΔA_{x-Feb}^{y}.

The emission of CO_2 and CO from the power sector (C_{Feb}^{ELEC}) is recorded by Continuous Emissions Monitoring Systems (CEMS) installed on power plants. The CEMS data are available from EPA's Air Markets Program Data (EPA, 2020a). The 'Others' sector (C_{Feb}^{Etc}) accounts for 6% of the state-wide emission of CO_2 in 2017 according to the state inventory (MDE, 2017) and 2% of the emission of CO for our study domain according to the National Emissions Inventory 2017 (EPA, 2021). Assuming the emission of CO_2 and CO (C_{Feb}^{Etc}) from the 'Others' sector emission is accurately represented in the state inventory and NEI2017, three variables in Equation 3.2 (C_{Feb}^{RCI}, C_{Feb}^{Onroad}, $C_{Feb}^{Nonroad}$) remain as unknowns. These three unknowns (C_{Feb}^{RCI}, C_{Feb}^{Onroad},

$C_{Feb}^{Nonroad}$) can be numerically solved as an intersection point of three planes (one plane from Equation 3.2 and two planes from Equation 3.3 for April and May).

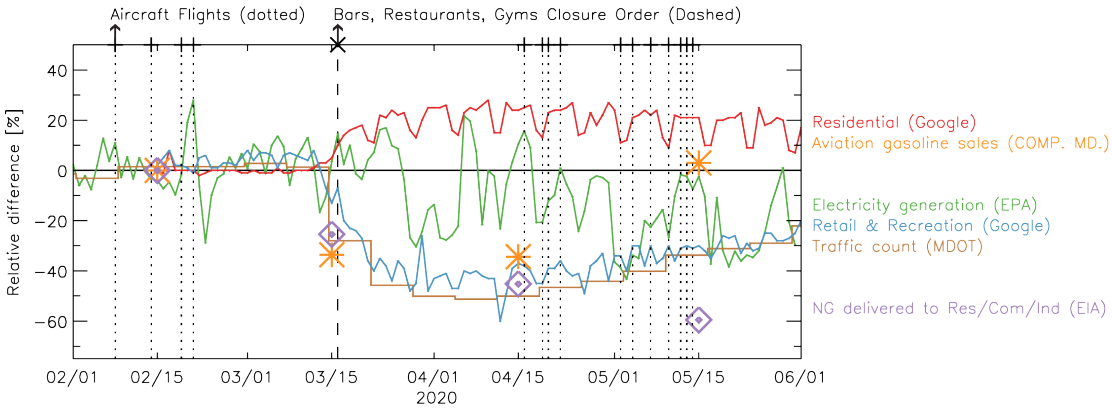

Figure 3.2. Percentage change of activity-metrics for six emission source sectors in the Baltimore, MD and Washington, D.C. area relative to baseline values in February 2020. The red line is daily residential activity (Google, 2020), orange asterisks are monthly aviation gasoline sales (Comptroller of Maryland, 2020), the green line is daily electricity generation from power plants in the Balt-Wash area (EPA, 2020a), the blue line represents daily retail & recreation activity (Google, 2020), the brown line denotes the weekly traffic count (MDOT, 2020), and purple diamonds are monthly natural gas delivered to residential, commercial, and industrial customers (EIA, 2021a). Vertical dotted lines indicate the 14 dates of the aircraft research flights. The vertical dashed line marks 16 March 2020, the day when the Maryland and D.C. governments ordered the closure of recreational facilities to slow the spread of COVID-19, which was the first local area governmental action taken to slow the spread of the pandemic (NGA, 2020).

3.3 Results and Discussions

3.3.1 Atmospheric distribution of CO_2 and CO: Before and After COVID-19 Lockdown

A series of aircraft research flights allow us to assess the changes in vertical distribution of atmospheric trace gases. Figure 3.3 shows the dry-air mole fraction of CO_2 and CO observed during the 14 UMD and NOAA flights from February to May 2020 (see Table 3.1). The mean and the standard deviation of the planetary boundary layer (PBL) height was 1,412 ± 300 m for the four flights in February 2020. The PBL

height increased to 1,804 ± 513 m in April, and to 1,876 ± 419 m in May 2020 (The diamond symbols in Figure 3.3c). In February 2020, the mean and the standard deviation of CO_2 within PBL was 421.8 ± 0.7 ppm (Figure 3.3a). In April, the PBL mean CO_2 was 421.2 ± 0.7 ppm, 0.6 ppm lower than the February mean. In May, the PBL mean CO_2 further decreased to 417.0 ± 1.5 ppm, indicating the increase in biospheric CO_2 uptake as the domain warmed. The gridded GPP product derived from the TROPOMI's solar-induced fluorescence (SIF) retrieval documents the increased biospheric uptake of CO_2 over the Balt-Wash area during May 2020 (Figure S3.3, Turner (2020)). Here we quantify the impact of biospheric uptake on mass balance estimates of the CO_2 emissions, using the gridded GPP product, the EDGARv50 CO_2 product, and the Hybrid Single-Particle Lagrangian Integrated Trajectory (HYSPLIT) model, as described in section 3.2.3.

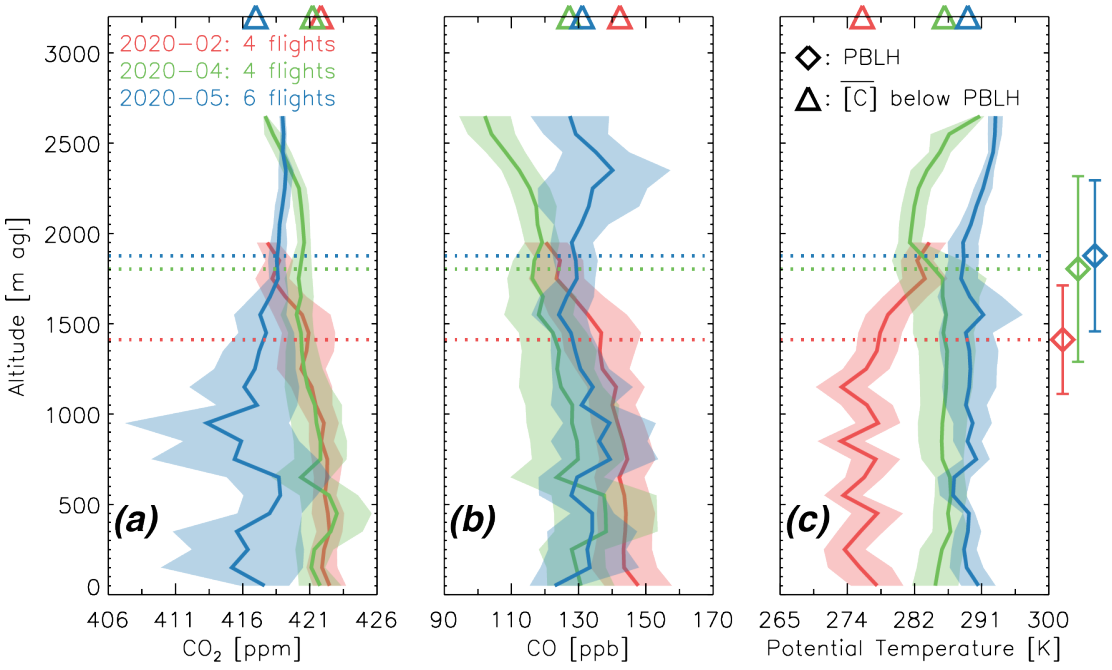

Figure 3.3. Vertical profiles of CO_2 (a), CO (b), and potential temperature (c) observed during the 14 UMD and NOAA aircraft research flights in February (red), April (green), and May (blue) of 2020. The number of research flights in each month are shown at

the top of panel (a). The solid lines and shaded areas indicate the mean and the standard deviation of each parameter (CO_2, CO, potential temperature) within 100 m vertically spaced bins. The diamond symbols and their errors bars shown to the right of panel (d) indicate the mean and the standard deviation of the PBL height for flight days in each month. The triangle symbols shown on the top of each panel indicate the mean CO_2, CO, and potential temperature within the PBL (a-d).

Mean values of CO in the PBL exhibited temporal trends from February to April similar to these described above for CO_2. During the February flights, the mean and the standard deviation of CO within PBL was 142 ± 3 ppb (Figure 3.3b). In April, the PBL mean CO decreased to 127 ± 6 ppb, 15 ppb lower from the February mean. However, from April to May the mean value of CO within the PBL increased to 131 ± 5 ppb, a behavior that contrasts that of CO_2 which decreased from April to May. The observed temporal change in the CO mole fraction within the PBL follows a similar trend of traffic volume. Figure 3.2 shows that traffic volume abruptly declined on 16 March 2020, when the state of Maryland and D.C. governments first ordered the closure of recreational facilities (NGA, 2020). Reduction in traffic volume peaked during the first week of April 2020, then displayed signs of a slow recovery (brown line in Figure 3.2). The mole fraction of atmospheric trace gases varies depending on emission sources, sinks, PBL height, wind, and background mole fractions. We quantify the changes in the emission of CO_2 and CO during COVID-19 pandemic in section 3.3.2.

3.3.2 Emissions of CO_2 and CO: Before and After COVID-19 Lockdown

We now focus on the emissions of CO_2 and CO over the Baltimore, MD-Washington, D.C. area (the Balt-Wash area) during the COVID-19 pandemic period. On 16 March 2020, the state of Maryland and D.C. governments ordered the closure of

recreational facilities to slow the spread of COVID-19 (NGA, 2020). Figure 3.2 shows that activity-metrics of several major source sector have abruptly changed on 16 March 2020. We estimate the emission rates of CO_2 and CO during the COVID-19 pandemic using the aircraft-based mass balance approach (see section 3.2.2). Table 3.1 shows the emission rates of CO_2 and CO over the Balt-Wash area determined from 14 research flights in February, April, and May 2020.

For the four flight days in February 2020, we estimate the mean and the standard deviation of the emission rate of CO_2 to be 54,700 ± 16,800 mol s^{-1} based on mass balance computations (Table 3.1). During the four flights in April 2020, our estimate of the CO_2 emission rate is 37,200 ± 10,700 mol s^{-1}, 32% lower than the February mean. As described in section 3.2.4, we attribute the observed change in the CO_2 emission rate to the following five sectors: power generation (Elec), onroad transportation (Onroad), nonroad transportation (Nonroad), residential/commercial/industrial (RCI), and a sector denoted other. Our estimates indicate that the largest decline from February to April is from the Onroad sector ($\Delta C_{Apr}^{Onroad} = \frac{c_{Feb}^{Onroad}}{c_{Feb}^{Total}} \cdot \Delta A_{Apr}^{Onroad} = -11{,}700$ mol s^{-1}, see Equation 3.3), followed by the RCI sector ($\Delta C_{Apr}^{RCI} = -4{,}600$ mol s^{-1}) and the Nonroad sector ($\Delta C_{Apr}^{Nonroad} = -1{,}100$ mol s^{-1}). For the six flights in May 2020, the CO_2 emission rate was determined to be 39,100 ± 14,700 mol s^{-1}, which is 29% lower than the February mean and 5% higher than the April mean. Our sector attribution analysis indicates that the CO_2 emission rate in May was larger than that in April, mainly because the increase in emissions of CO_2 from the transportation sector (i.e., the recovery in traffic volume) was about a factor of two greater than the decrease in

emissions of CO_2 from the RCI sector (i.e., less demand for spatial heating in office buildings).

For February 2020, our mass balance, top-down estimate of the emission rate of CO over the Balt-Wash area to be 329 ± 124 mol s^{-1} (Table 3.1). For April, our estimate of the CO emission rate is 206 ± 54 mol s^{-1}, which is 37% (123 mol s^{-1}) lower than the February mean. Our source sector attribution analysis (applications of Equations 3.2 and 3.3) indicates that the largest portion of the observed decrease, 30% (99 mol s^{-1}), was from the onroad transportation sector. The RCI sector was the second largest source of this reduction, accounting for a decline of 5% (16 mol s^{-1}). For the six flights in May, our estimate of the CO emission rate rose (relative to April) to a value of 241 ± 42 mol s^{-1}, which is still 27% (88 mol s^{-1}) lower than the February mean. From February to May, the onroad sector was the largest source of the reduction (24%, 78 mol s^{-1}), followed by the nonroad transportation sector (2%, 6 mol s^{-1}). The MDOT traffic count data shows that the traffic volume in our domain declined by 48% from February to April 2020. In May 2020, the traffic volume showed a sign of recovery, 37% lower than the traffic in February (Figure 3.2, MDOT (2020)). These aircraft-based mass balance estimates demonstrate that this technique can capture the abrupt change in the CO emissions induced by COVID-19 based upon bottom-up data.

The emissions of CO_2 and CO during February-May 2020 are affected by both behavioral changes driven by COVID-19 and normal seasonal patterns of source sectors (Huang et al., 2019). The energy demand for the spatial heating/cooling varies as a function of outdoor temperature (Beheshti et al., 2019) and traffic volumes also follow seasonal patterns (Memmott & Young, 2008). According to MDOT traffic count

data, traffic volume in our study domain during April-May 2019 was 18% greater than that of February 2019. Using traffic volume in 2019 as a baseline, declines in traffic volume due to COVID-19 are 65% for April and 54% for May 2020. Such declines in traffic volumes led to 34% and 28% declines in the emission of CO_2 and CO for our study domain, respectively, based on our source sector attribution analysis (see section 3.2.4). Meanwhile, the emissions from the residential sector were likely to have increased due to COVID-19, as people spent more time at home. Separating the impact of COVID-19 from natural variability would require detailed analysis of meteorological and socioeconomic data (Goldberg et al., 2020). For the source sectors other than onroad transportation, we do not attempt to separate the impact of COVID-19 from the normal-year seasonality.

Table 3.1. The emission rates of CO_2 and CO estimated from mass balance flights conducted during February, April, and May 2020.

Flight	Date	CO_2 [mol s^{-1}]	CO [mol s^{-1}]
UMD-RF1	02/08 (SAT)	39,600	230
UMD-RF3	02/14 (FRI)	50,500	333
UMD-RF5	02/19 (WED)	78,700	502
UMD-RF6	02/21 (FRI)	49,900	252
February Mean ± 1σ		54,700 ± 16,800	329 ± 124
UMD-RF7	04/16 (THU)	46,800	259
UMD-RF8	04/19 (SUN)	44,400	241
UMD-RF9	04/20 (MON)	23,200	141
UMD-RF10	04/22 (WED)	34,600	184
April Mean ± 1σ		37,200 ± 10,700	206 ± 54
UMD-RF13	05/07 (THU)	49,000	232
UMD-RF14	05/10 (SUN)	27,200	200
UMD-RF16	05/14 (THU)	21,400	203
NOAA-RF12	05/07 (THU)	N/A*	258
NOAA-RF14	05/12 (TUE)	41,100	241
NOAA-RF15	05/13 (WED)	56,600	314
May Mean ± 1σ		39,100 ± 14,700	241 ± 42

* The impact of the active biosphere was above the threshold of 20% and excluded from the mass balance calculation (see section 3.2.4).

3.3.3 Comparison to Emission Inventories: Overview

We next compare our top-down estimates of the CO_2 and CO emission rates, computed using February 2020 aircraft data (i.e., prior to COVID-19 lockdowns), to following three bottom-up inventories: EDGARv50 (monthly, 0.1°, global, Crippa et al. (2021)), Maryland GHG inventory 2017 (annual, state, MDE (2017)), and the National Emissions Inventory (NEI) 2017 (annual, county, EPA (2021)). From the three bottom-up inventories (EDGARv50, MDE2017, and NEI2017), we compute the emission rate of CO_2 and CO over our study domain as follows. First, we update the power sector emissions of CO_2 in EDGARv50 and MDE2017, by replacing with the mean CO_2 emission rates recorded from continuous emissions monitoring system (CEMS) during February 2020 (EPA, 2020a). Second, we minimize the spatial coverage difference between our aircraft-based estimates and three bottom-up inventories. For the EDGARv50, we sum the emissions of CO_2 and CO for the grids located in our aircraft footprint area (grey area in Figure S3.1). For the NEI2017, we sum the CO emissions for the following counties: Montgomery, Howard, Anne Arundel, Prince George's, Baltimore City, Baltimore (Maryland), Fairfax, Arlington, Prince William (Virginia), and Washington, D.C, which cover most of our study domain. For the MDE2017, the state-wide total CO_2 emissions, excluding the power sector, are scaled by a factor of 1.27, which is the ratio of the 2020 population within the aircraft footprint (7.78 million) to the population of the state of Maryland in 2017 (6.02 million). The three bottom-up inventories cover different years (i.e., EDGARv50: 2015, the state of Maryland inventory: 2017, and NEI2017: 2017) with varying temporal resolution (i.e., EDGARv50: monthly, state of Maryland inventory: annual,

NEI2017: annual). We do not attempt to harmonize the temporal mismatch existing between bottom-up inventories and our aircraft observations during 2020.

3.3.4 CO_2: Aircraft-based, EDGAR, and State Inventory

Figure 3.4a shows the top-down and bottom-up estimates of the emissions of CO_2 from the Baltimore, MD-Washington, D.C. area. The three leftmost bars in Figure 3.4b are the emission estimates prior to the COVID-19 government measures, and the two rightmost bars are the estimates in the midst of COVID-19 pandemic. We attribute the aircraft-based estimate of the CO_2 emissions to five source sectors using the observed changes the total emissions of CO_2 and the percentage changes in source sector activities (see section 3.2.4).

For the four research flights conducted in February 2020, prior to the major COVID-19 outbreak, we estimate the mean emission rate of CO_2 to be 54,700 ± 16,800 mol s^{-1} (Figure 3.4a). For the study domain, EDGARv50 estimates the emission rate of CO_2 as 44,900 ± 2,600 mol s^{-1}, which is 18% lower than our aircraft estimate. The state of Maryland GHG inventory, scaled by population to represent our aircraft footprint area, provides a CO_2 emission rate of 47,300 ± 4,600 mol s^{-1}, which is 13% lower than our top-down estimate. This result is consistent with the findings in Gurney et al. (2021): self-reported inventories for 25 cities in the Eastern U.S underestimate the fossil-fuel based emission of CO_2 by 25% (95% CI: 12.8% to 37.8%), in comparison to the Vulcan CO_2 product which is consistent with atmospheric measurements.

We determine that the largest source is the onroad transportation sector (52% of the total emissions), followed by RCI (27%), nonroad transportation (11%), and

electricity generation (5%). For the EDGARv50, our sector attributions indicate that the onroad sector is the major source of underestimation in the EDGARv50 CO_2 emissions. Also, we find that the large underestimation in the EDGARv50's onroad transportation sector (−19,990 mol s^{-1}) is partly balanced by the overestimation in the RCI sector (+10,540 mol s^{-1}). For the state of Maryland bottom-up inventory, the overall source sector composition for the emission of CO_2 shows good agreement with our aircraft-based top-down sector composition estimate. The nonroad transportation sector is largest contributor to the underestimation in the state inventory (3,200 mol s^{-1}), followed by onroad transportation sector (2,300 mol s^{-1}) and RCI sector (1,900 mol s^{-1}).

Ahn et al. (2020) (hereafter A2020) estimated the emission rate of CO_2 over the Baltimore, MD-Washington, D.C. area to be 89,000 ± 15,000 mol s^{-1}, based upon analysis of data collected during seven mass balance flights in February 2015. The aircraft footprint area covered in A2020 is 17,904 km^2, 42% larger than the footprint area covered in this study (12,629 km^2). Assuming the CO_2 emissions scales linearly with geographic domain across the Baltimore-Washington metropolitan area, we scale our top-down estimate of 54,700 ± 16,800 mol s^{-1} by a factor of 1.42, a ratio of the footprint area in A2020 to the area in February 2020. Our estimate of the CO_2 emission rate, scaled to represent footprint area in A2020, is 77,700 ± 23,900 mol s^{-1}, 13% (11,300 mol s^{-1}) lower than the A2020 estimate. Such decline in the CO_2 emissions observed between 2015 and 2020 is mostly from to the power sector. According to the CEMS records of power plants in the study domain, the CO_2 emission rate from power

plants was 21,000 mol s^{-1} in February 2015 and 5,700 mol s^{-1} in February 2020 (EPA, 2020a).

The rapid decline in the power sector emission of CO_2 between February 2015 and February 2020 for the study domain is a result of the following three factors. First, the warmer outdoor temperature in February 2020 compared to February 2015 (i.e., monthly sum heating degree days (HDD, base temperature 65°F) for the state of Maryland declined from 1,105 in February 2015 to 705 in February 2020 (NOAA CPC, 2020)), resulting in a reduction in electricity demand for heating. Second, the shutdown of two coal-fired power plants (i.e., Charles P. Crane Generating Station retired in 2018 and Luke Mill Power Plant retired in 2019, (EIA, 2021b)) led to less power generation in the study domain. Third, the increasing share of natural gas power units within the state of Maryland and increase in the import of electricity from nearby states also contributed (MDE, 2017). The state climate goal (i.e., the greenhouse gas reduction act (GGRA)) under the state/regional initiatives (i.e., Maryland Commission on Climate Change and the Regional Greenhouse Gas Initiative (RGGI)) played an important role in achieving these reduction in the emission of CO_2 from the power sector.

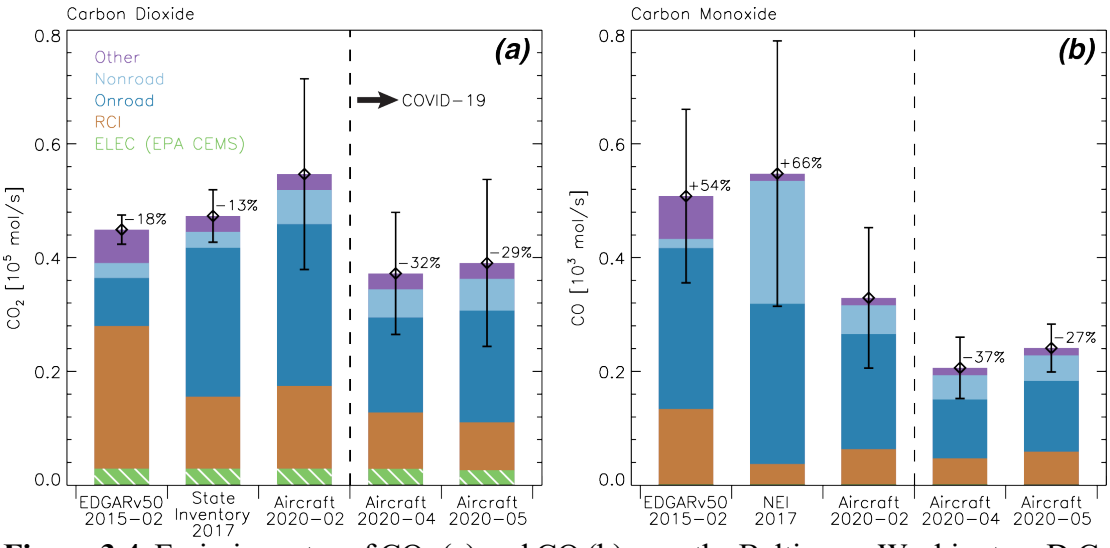

Figure 3.4. Emission rates of CO_2 (a) and CO (b) over the Baltimore-Washington, D.C. area. For each panel, the two leftmost estimates are based on bottom-up emission inventories (i.e., EDGARv50, the state of Maryland GHG inventory 2017, National Emissions Inventory 2017) and the three rightmost estimates are from the aircraft-based mass balance approach for February, April, and May 2020. The vertical dashed line distinguishes the time before (left to the dashed line) and after (right to the dashed line) the date when Maryland and D.C. governments first ordered the closure of recreational facilities to slow the spread of COVID-19 (see Figure 3.2). For the comparison of bottom-up and top-down emission estimates, bottom-up estimates are scaled to match the spatiotemporal footprint of aircraft observations (see section 3.3.3). The error bar indicates 1σ uncertainty range assigned to each estimate (see Section 3.5.2). The bottom-up estimates are colored by major source sector as provided by each inventory. The aircraft top-down estimate of CO_2 and CO emissions during February 2020 are apportioned to major source sectors by relating observed emission reductions during COVID-19 pandemic to change in source sector activity-metrics such as traffic counts and natural gas consumptions (see section 3.2.4).

3.3.5 CO: Aircraft-based, EDGAR, and NEI

Figure 3.4b shows the top-down and bottom-up estimates of the emissions of CO from the Baltimore, MD-Washington, D.C. area. The three leftmost bars in Figure 3.4b are the emission estimates prior to the COVID-19 government measures, and the two rightmost bars are the estimates in the midst of COVID-19 pandemic. For the four research flights in February 2020, prior to the COVID-19 directives, we estimate the

mean emission rate of CO to be 329 ± 124 mol s^{-1} based on the aircraft data (Table 3.1). The EDGARv50 bottom-up estimate of the CO emission rate for the same domain covered by the analysis of aircraft data is 508 ± 152 mol s^{-1}, a value that is 54% (179 mol s^{-1}) greater than our top-down estimate. Several studies have reported that the emissions of CO in EDGAR is overestimated (Kim et al., 2013; Miller et al., 2008; Parrish, 2006; X. Ren et al., 2018). Our sector attribution analysis indicates that EDGARv50 overestimates the emission of CO by about a factor of two (71 mol s^{-1}) for the RCI sector, and by 40% (81 mol s^{-1}) for the onroad transportation sector. Also, we find that EDGARv50 underestimates CO emissions from the Nonroad transportation by 69% (35 mol s^{-1}). The NEI2017 value for the emission rate of CO for 2017 is 548 ± 233 mol s^{-1}, which is also 66% greater than our top-down estimate. Our sector attribution analysis indicates that the largest discrepancy between the NEI and our top-down emission estimate for CO is due to the nonroad transportation sector. The NEI estimates the Nonroad emission rate of CO to be 216 mol s^{-1}, which is a factor of ~4 greater than our estimate of 51 mol s^{-1} (Figure 3.4b).

Both Salmon et al. (2018) and Ren et al. (2018) (hereafter S2018 and R2018) reported the emission rate of CO over the Balt-Wash area using aircraft-based, top-down approaches. S2018 estimated the CO emission rate to be 540 ± 490 mol s^{-1} (mean and the 95% CI), based on five mass balance flights conducted during February 2015. R2018 estimated the emission rate of CO over the Balt-Wash area as 500 ± 411 mol s^{-1} (mean ± 1σ) from seven mass balance flights in February 2015. Both S2018 and R2018 computed emissions using the same aircraft dataset in A2020. Assuming the aircraft footprint area covered in S2018 and R2018 is same as that in A2020 (17,904

km^2), we can scale the top-down estimate for the emission of CO in this study by a factor of 1.42 (see section 3.3.4) to cover comparable areas. Our estimate of the CO emission rate for February 2020, scaled to match the footprint area in S2018 and R2018, is 467 ± 176 mol s^{-1}. This estimate of the CO emission rate for 2020 is 14% lower than the S2018 estimate and 7% lower than the R2018 estimate. This observed 7 to 14% decline in the emission of CO between the winter of 2015 and 2020 could be induced by improved emission efficiencies via emission controls and regulations (i.e., the Maryland Clean Cars Program (MDOT & MDE, 2016)) and increase of electric vehicles (Slowik & Lutsey, 2018). We leave detailed analysis on inter-annual trend analysis as a future study. Multi-year aircraft/ground tower observation data will be needed for such trend analysis.

3.4 Conclusions

In this study, we have investigated the urban emissions of CO_2 and CO from the Balt-Wash area during the COVID-19 pandemic. First, we compared the airborne observations of CO_2 and CO obtained during February 2020 (prior to the implementation of COVID-19 measures) to April-May 2020 (in the midst of COVID-19 pandemic). Our aircraft observations show that atmospheric CO_2 within the planetary boundary layer (PBL) decreased from February (421.8 ± 0.7 ppm), to April (421.2 ± 0.7 ppm), and extending into May (417.0 ± 1.5 ppm). Meanwhile, the atmospheric CO within PBL decreased from February (142 ± 3 ppb) to April (127 ± 6 ppb), and showed a modest increase in May (131 ± 5 ppb). Second, we quantified the reductions in the emission of CO_2 and CO during the COVID-19 pandemic using the aircraft-based mass balance approach. Our mass balance estimates indicate that the

mean CO_2 emission rate over the Balt-Wash area declined by about 32% in April and by 29% in May 2020, relative to the February mean. Our estimate of the mean CO emission rate declined by 37% in April and 30% in May, relative to the February mean. For both CO_2 and CO, the onroad transportation sector was determined to be the largest contributor to reduced emission rates in April 2020, followed by the RCI sector.

We evaluated three bottom-up inventories (EDGARv50, the state of Maryland GHG inventory, and NEI2017) using our aircraft-based estimates of the CO_2 and CO emission rates. Also, sector compositions in the bottom-up inventories were evaluated using our estimate of the sector contributions to these emissions. Our analysis indicates that the observed, top-down emission of CO_2 over the Balt-Wash area based on analysis of the aircraft data acquired during February 2020 is about 18% larger than the EDGARv50 bottom-up emission value. The Maryland data inventory underestimates our observed, top-down value for the emission of CO_2 by 13%. These results are consistent with the findings of Gurney et al. (2021), who reported that the self-reported fossil fuel emissions of CO_2 provided by 25 cities in the Eastern U.S. tend to be about 25% (95% CI: 12.8% to 37.8%) lower than estimates from the Vulcan emissions product, which is consistent with atmospheric measurements. For the source sector composition of the emission of CO_2, the state inventory showed overall better agreement with our estimate than the sector attribution provided by EDGARv50.

Meanwhile, our analysis indicates that the emission of CO over the Balt-Wash area is overestimated by about 54% within EDGARv50 and by about 66% in NEI2017. Based on our sector attribution analysis, the nonroad transportation sector was the largest contributor to the NEI overestimate of the emission of CO during February 2020.

McDonald et al. (2018) reported that bottom-up mobile source emissions of CO in the NEI for 2013 are about 90% higher than their own fuel-based inventory of motor-vehicle emissions (FIVE). Similarly, Salmon et al. (2018) reported that the emission of CO provided by NEI2014 emissions are factor of ~2.0 greater than their average top-down emission estimate of CO for the Baltimore, MD-Washington, D.C. region. Our study indicates that the nonroad sector emissions could be a major source of the overestimation for the Balt-Wash area.

We leave several topics for future study. First, we did not separate the impact of COVID-19 from the normal-year seasonality for the source sectors, other than onroad transportation. Separating the normal-year seasonality would require the analysis of various meteorological data (i.e., outdoor temperature) and the socioeconomic data (i.e., gross domestic product, energy prices). Second, even though we compared the emissions of CO_2 and CO over the Balt-wash area estimated during winters of 2015 and 2020 by comparing our results to previously published studies, we did not attempt to assess the inter-annual variability. The UMD have conducted more than 70 aircraft research flights over the Balt-Wash area from 2015 to 2020. In the future study, these aircraft measurements collected spanning 6 years will be analyzed, using the similar methods presented in this dissertation, to quantify trends in the emissions of CO_2 and CO. Nonetheless, our study provides an assessment of the change in the CO_2 and CO emissions and their source sector compositions during COVID-19 pandemic period, highlighting both underestimations in the bottom-up CO2 emissions inventories and overestimations in the bottom-up CO inventories. Our study will

hopefully spur further scrutiny of the bottom-up emissions estimates, which are central to so many policy decisions.

3.5 Supporting Information

3.5.1 Simulating the enhancements of CO_2 downwind of the Baltimore, MD-Washington, D.C. area: Fossil-fuel emissions and biogenic uptake of CO_2

The impacts of biosphere on the aircraft-based estimate of the emissions of CO_2 were evaluated by simulating the enhancement signal of urban CO_2 plumes for the following two scenarios:1) only fossil-fuel CO_2 ($FFCO_2$) emissions exist in the study domain ($\Delta F_{Balt-Wash}^{FFCO2}$); 2) both $FFCO_2$ emissions and biospheric CO_2 uptake exist in the study domain ($\Delta F_{Balt-Wash}^{FFCO2,GPP}$). Here, GPP refers to gross primary productivity. To simulate the CO_2 enhancement signal ($\Delta F_{Balt-Wash}^{FFCO2}$ and $\Delta F_{Balt-Wash}^{FFCO2,GPP}$), we compute the Hybrid Single-Particle Lagrangian Integrated Trajectory (HYSPLIT) back trajectory starting from the aircraft locations every 1 seconds downwind of the study domain (Draxler et al., 2014; Stein et al., 2015). The High-Resolution Rapid Refresh (HRRR) is used as an input meteorology (NOAA, 2020a). For each back trajectory, we compute the mean biogenic CO_2 uptake (F_i^{GPP}, the green lines in Figure S3.3h-j) by sampling the gridded product of the gross primary productivity (GPP). We use the gridded GPP product (daily, 500 m) developed using the solar induced fluorescence (SIF) retrieval from the Tropospheric Monitoring Instrument (TROPOMI) (Turner et al., 2020). Similarly, we compute the mean $FFCO_2$ flux (F_i^{FFCO2}, the red lines in Figure S3.3h-j) along each back trajectory by sampling grids of the Emissions Database for Global

Atmospheric Research version v5.0 (EDGARv50, Crippa et al. (2020)). For each back trajectory, which start off of every 1 second aircraft locations, we compute the enhanced signals of CO_2 for two scenarios (ΔF_i^{FFCO2} and $\Delta F_i^{FFCO2,GPP}$) by subtracting background values determined from the linear fitting method (red dotted lines and black dotted lines in Figure S3.3h-j). Lastly, the enhancement signals of urban CO_2 plume for the two scenarios are computed by integrating the enhanced CO_2 flux across the aircraft flight leg ($\Delta F_{Balt-Wash}^{FFCO2} = \sum \Delta F_i^{FFCO2}$ and $\Delta F_{Balt-Wash}^{FFCO2,GPP} = \sum \Delta F_i^{FFCO2,GPP}$). We consider the aircraft transect, which show the absolute relative difference between $\Delta F_{Balt-Wash}^{FFCO2,GPP}$ and $\Delta F_{Balt-Wash}^{FFCO2}$ greater than 20%, as heavily affected by the active biosphere and exclude in the mass flux calculation. Table S3.1 show our estimates of the $\Delta F_{Balt-Wash}^{FFCO2,GPP}$ and the $\Delta F_{Balt-Wash}^{FFCO2}$ for total 14 research flights used in this study.

3.5.2 The uncertainties for the bottom-up estimates of the emissions of CO_2 and CO from the Baltimore, MD-Washington, D.C. area

For the EDGARv50 emissions of CO_2 (the first bar in Figure 3.4a), we assume an 1σ uncertainty of 5.7%, determined from the total national uncertainty in Janssens-Maenhout et al. (2017). For the EDGARv50 emissions of CO (the first bar in Figure 3.4b), we assume an 1σ uncertainty of 30%, estimated from the total national uncertainty in Crippa et al. (2018). For the state of Maryland inventory emissions of CO_2 (the second bar in Figure 3.4a), we propagate uncertainties from the following two sources: 1) an uncertainty of 7% determined for the state of Maryland inventory in Ahn et al. (2020); 2) a standard deviation of population in aircraft footprint area, which are

used to scale the state-wide total emissions into our aircraft footprint. For the National Emissions Inventory (NEI) 2017 (the second bar in Figure 3.4b), we use a standard deviation of the following three terms as 1σ uncertainty of the emissions of CO estimated for our aircraft footprint: 1) the CO emissions calculated as the sum of 9 counties and Washington, D.C., as described in section 3.3.3; 2) the CO emissions calculated by scaling up the total emissions from Washington, D.C. using the ratio of populations (i.e., population_aircraft / population_D.C = 11.4); 3) the CO emissions calculated by scaling up the total emissions from the state of Maryland using the ratio of populations (i.e., population_aircraft / population_D.C = 1.27).

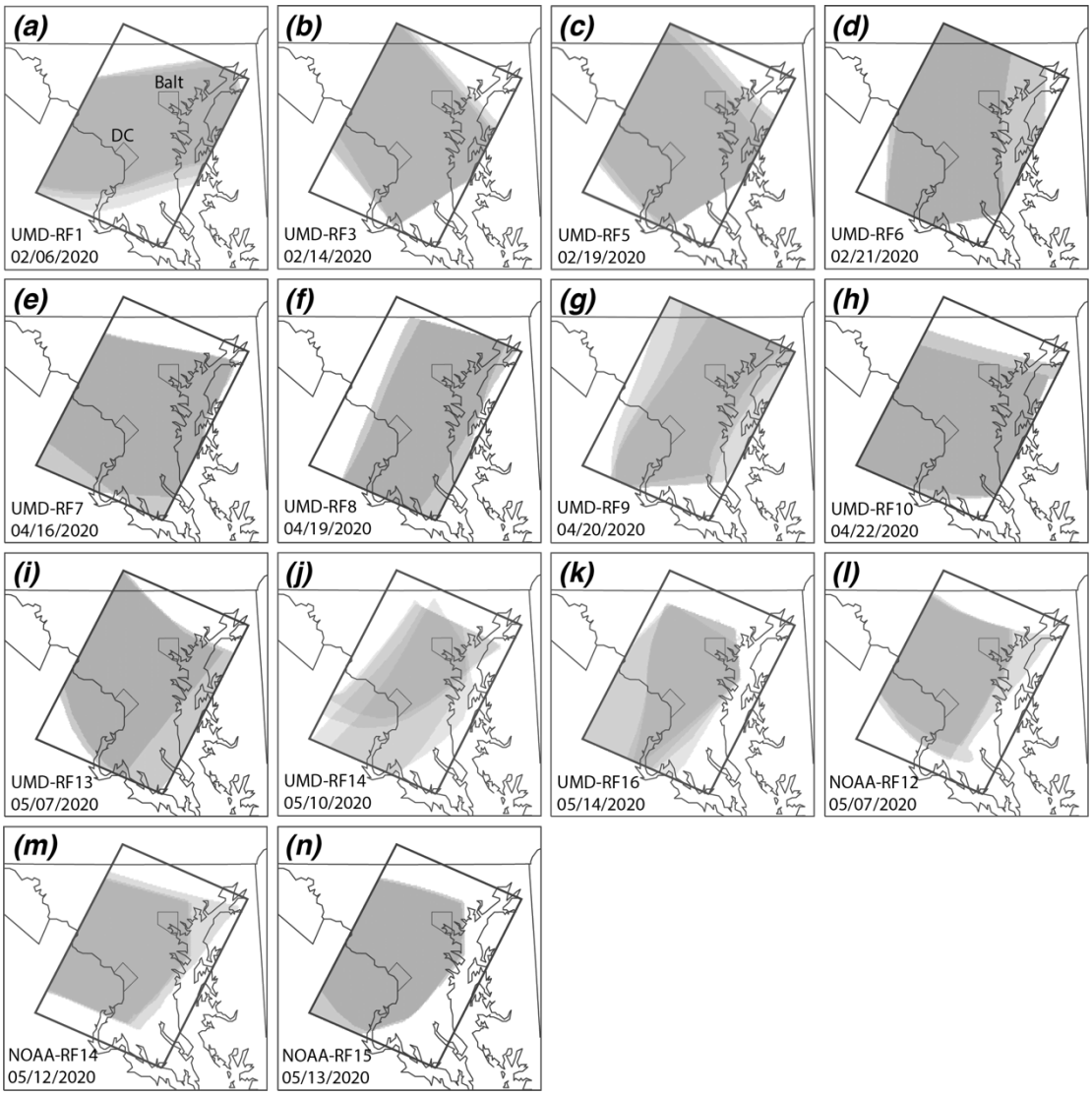

Figure S3.1. Aircraft footprint area for each of the 14 research flights used to compute the emission rate of CO_2 and CO over the Baltimore, MD-Washington, D.C. area (see Table 3.1). The grey shaded area represents the aircraft footprint area determined using HYSPLIT back trajectory ran with HRRR meteorology. The footprint areas determined from each of the downwind flight legs are overlapped (Each flight conducted 2-4 downwind flight legs). The black rectangular box represents the geographical domain that Ahn et al. (2020) used to compute the emission rate of CO_2 for February 2015 (=17,904 km^2).

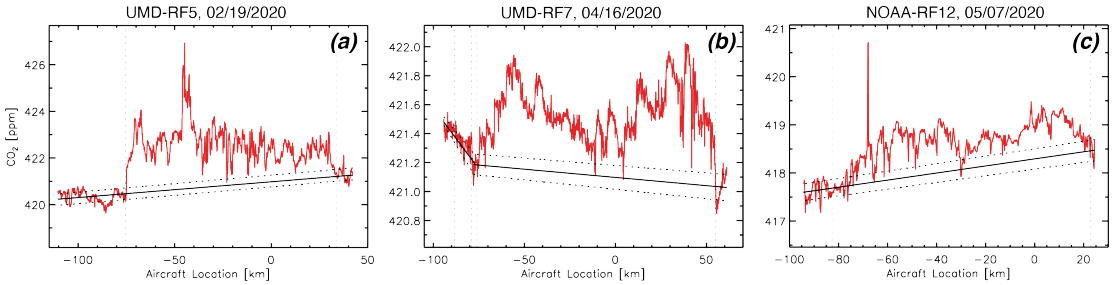

Figure S3.2. The red lines indicate mole fractions of CO_2 measured downwind of the Baltimore, MD-Washington, D.C. area for the three mass balance flights (a-c). The black solid lines indicate background CO_2 used to estimate the emission rate of CO_2 ([C_{bg}] in Equation 3.1); The black dotted lines indicate the ±1σ uncertainty range of background CO_2. The vertical dotted lines indicate the horizontal boundaries of flight segments used to determine the values of background CO_2 with the least square linear regression fits.

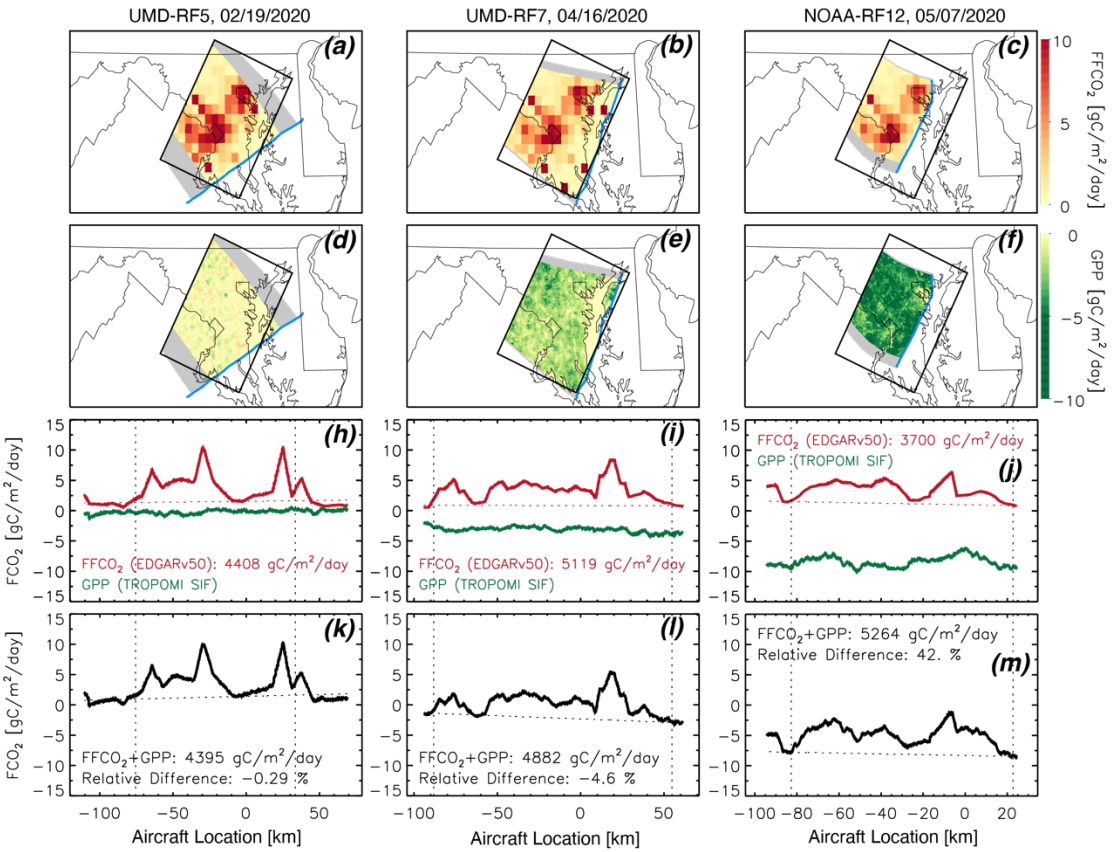

Figure S3.3. (a-c) The first-row panels show the gridded fossil-fuel CO_2 ($FFCO_2$) flux from the EDGARv50. The aircraft tracks are shown as blue lines. Colored area represents the spatial footprint area of the airmass. (d-f) The second-row panels show the gridded gross primary productivity (GPP) determined from the TROPOMI-SIF retrieval data (Turner et al., 2020). (h-j) The third-row panels show spatial variabilities of $FFCO_2$ (red) and GPP (green) across the aircraft footprint area. The ordinate of the plot is the values of $FFCO_2$ or GPP averaged for the grid cells sampled along with each back trajectory. The abscissa is the starting location of back trajectory (i.e., distance from the middle of downwind flight leg). The red dotted lines indicate background of $FFCO_2$ (i.e., a least square linear fit to values in edges). The integral value of $FFCO_2$ enhancements (i.e., area between red solid line and red dotted line) is shown at the bottom of each panel. (k-m) The fourth-row panels show spatial variabilities of the sum of $FFCO_2$ and GPP (black) across the aircraft footprint area. The black dotted lines indicate background of $FFCO_2$+GPP determined using the edge fitting method. The left-column panels show the 19 February flight, the middle-column panels show the 14 April flight, and the right-column panels show the 7 May 2020 flight.

Table S3.1. The enhancement signals of urban CO_2 plumes estimated for 14 research flights in the following two scenarios: 1) only $FFCO_2$ emissions exist in the Balt-Wash area ($\Delta S^{FFCO2}_{Balt-Wash}$); 2) both $FFCO_2$ emissions and biospheric CO_2 uptake exist in the Balt-Wash area ($\Delta S^{FFCO2,GPP}_{Balt-Wash}$).

Date	Flight leg	$\Delta S^{FFCO2}_{Balt-Wash}$	$\Delta S^{FFCO2+GPP}_{Balt-Wash}$	Absolute Relative Diff [%]
02/08/2020	UMD-RF1 (a)	3,152	3,074	2.5
	UMD-RF1 (b)	3,602	3,361	6.7
	UMD-RF1 (c)	2,533	2,262	10.7
	UMD-RF1 (d)	3,189	3,293	3.3
02/14/2020	UMD-RF3 (a)	6,827	6,895	1.0
	UMD-RF3 (b)	5,107	5,266	3.1
	UMD-RF3 (c)	4,791	4,778	0.3
02/19/2020	UMD-RF5 (a)	4,409	4,396	0.3
	UMD-RF5 (b)	4,338	4,376	0.9
	UMD-RF5 (c)	6,216	6,207	0.1
02/21/2020	UMD-RF6 (a)	4,371	4,609	5.5
	UMD-RF6 (b)	2,672	2,688	0.6
	UMD-RF6 (c)	7,123	7,983	12.1
04/16/2020	UMD-RF7 (a)	5,120	4,883	4.6
	UMD-RF7 (b)	4,736	5,226	10.3
04/19/2020	UMD-RF8 (a)	2,277	2,066	9.3
	UMD-RF8 (b)	2,116	2,492	17.7
04/20/2020	UMD-RF9 (a)	2,466	3,542	43.6
	UMD-RF9 (b)	2,443	2,843	16.4
	UMD-RF9 (c)	2,674	2,978	11.3
04/22/2020	UMD-RF10 (a)	4,849	5,805	19.7
	UMD-RF10 (b)	2,746	3,998	45.6
05/07/2020	UMD-RF13 (a)	4,558	3,829	16.0
	UMD-RF13 (b)	3,983	3,963	0.5
	NOAA-RF12 (a)	3,243	4,602	41.9
	NOAA-RF12 (b)	3,700	5,264	42.3
	NOAA-RF12 (c)	4,169	5,321	27.6
05/10/2020	UMD-RF14 (a)	2,635	2,221	15.7
	UMD-RF14 (b)	1,308	1,511	15.5
	UMD-RF14 (c)	1,601	2,481	54.9
	UMD-RF14 (d)	2,550	2,587	1.4
05/12/2020	NOAA-RF14 (a)	3,974	4,684	17.9
	NOAA-RF14 (b)	4,097	5,178	26.4
	NOAA-RF14 (c)	4,007	4,742	18.3
05/13/2020	NOAA-RF15 (a)	3,327	4,766	43.2
	NOAA-RF15 (b)	4,033	4,159	3.1
05/14/2020	UMD-RF16 (a)	3,340	3,947	18.2
	UMD-RF16 (b)	2,677	3,538	32.2
	UMD-RF16 (c)	3,368	4,375	29.9
	UMD-RF16 (d)	3,994	6,097	52.7

Table S3.2. The percentage changes in the emissions of CO_2 and CO from each of the four major source sectors (ΔA^{y}_{x-Feb} of Equation 3.3) and the activity metric data used to determine the percentage changes in the emissions.

Source Sector	$\Delta A^{y}_{Apr-Feb}$ [%]		$\Delta A^{y}_{May-Feb}$ [%]		Activity metrics (weighing factors for CO_2 and CO)	Data source
	CO_2	CO	CO_2	CO		
Electricity generation (ELEC)	−1.5	−1.5	−9.9	−9.9	1.Electricity generation (CO_2: 1.00, CO: 1.00)	1. EPA Air Markets Program Data (AMPD)
Residential/Commercial/Industrial (RCI)	−31.8	−26.0	−41.9	−6.8	1. Natural Gas delivered to RCI customers (CO_2: 1.00, CO: 0.21) 2. Monthly sales of densified biomass fuel in the U.S. East region (CO_2: 0.00, CO: 0.79)	1. EIA, Monthly Report of NG Purchases and Deliveries, (Form EIA-857) 2. U.S. EIA Densified Biomass Fuel Report (EIA 63C Table 7)
Onroad transportation (Onroad)	−41.3	−48.9	−31.0	−38.5	1. Traffic count of passenger vehicles (CO_2: 0.78, CO: 0.95) 2. Traffic count of trucks (CO_2: 0.22, CO: 0.05)	1-2. MDOT, Weekly Changes at Permanent Counters (ATR)
Nonroad transportation (Nonroad)	−17.6	−15.8	−6.9	−11.5	1. Monthly sales of special fuel (CO_2: 0.73, CO: 0.98) 2. Monthly sales of aviation fuel (CO_2: 0.27, CO: 0.02)	1-2. Comptroller of Maryland, Fuel Annual Report 2020

Chapter 4: Reduced Electricity Generation and Concomitant Emissions of CO_2 and NO_x in the United States during the COVID-19 Pandemic: Separating the Impact of COVID-19 from the Weather and Fuel-mix changes

4.1 Introduction

The United States (U.S.) power sector provides services that include generation, transmission, and distribution of electricity to customers in residential, commercial, and industrial sectors. In 2019, the U.S. power sector generated 4,127 billion kWh of electricity (EIA, 2020c). Combustion of natural gas was the largest source accounting for 38% of the total generation, followed by coal (23%), nuclear (20%), renewables (18%), and petroleum/other (1%). Electricity generation from combustion of fossil fuels produces air pollutants detrimental to climate and air quality, such as carbon dioxide (CO_2), nitrogen oxides (NO_x), sulfur dioxide (SO_2), and particulate matter. In 2019, the emission of CO_2 from the U.S. electricity generation sector was 1,618 million metric tons ($MTCO_2$), or 31% of the U.S. total energy-related emission of CO_2 (EIA, 2020g). The emission of NO_x from the electricity generation sector was 904 thousand metric tons in 2019, or 11% of the national total reported emission of NO_x (EPA, 2020b).

In the past decade, the U.S. power sector has seen trends of increasing use of natural gas and renewables and decreasing use of coal in fuel-mix profiles, driven

mainly by economic considerations (Fell & Kaffine, 2018; IEA, 2019). In 2010, the U.S. total electricity generation was 4,125 billion kWh, only 0.05% lower than the generation in 2019. However, the fuel composition in 2010 was significantly different from that in 2019 (detailed above). In 2010, coal was the largest fuel source (45%), followed by natural gas (23%), nuclear (20%), renewables (10%), and petroleum and other sources (1%) (EIA, 2020c). As a benefit of this fuel transition, significant improvement in the emission intensities of CO_2 and NO_x of the U.S. power sector have been reported (de Gouw et al., 2014; Lu et al., 2012; Schivley et al., 2018).

During the Severe Acute Respiratory Syndrome Corona Virus 2 (SARS-CoV-2 or COVID-19) global pandemic period in 2020, human activities around the globe were significantly reduced (WHO, 2020). As a result, reduction in emissions of CO_2 (Liu et al., 2020; Le Quéré et al., 2020; Alexander J Turner et al., 2020) and NO_x (Goldberg et al., 2020; Keller et al., 2020; Zhang et al., 2020) were reported for many countries. In the U.S., various types of social activity regulations and stay-at-home orders were issued at Federal, State, and Local levels starting in March 2020 (NGA, 2020). Several studies have assessed impacts of COVID-19 on the U.S. power sector using various approaches. Liu et al. (2020) reported a 7.6 % reduction in the emission of CO_2 from the U.S. power sector during the first half of 2020, using electricity generation in 2019 as a baseline for their analysis. The U.S. Energy Information Administration (EIA) published reports that show significant disruptions in electricity consumption pattern over the Midcontinent Independent System Operator (MISO) and the New York Independent System Operator (NYISO), after accounting for temperature changes (EIA, 2020b, 2020a). According to these EIA reports, weekday

electricity demand over MISO decreased by 9% - 13%, and weekday demand over NYISO decreased by 11% - 14% from the expected levels during late March to April 2020.

The objective of this study is to assess the impact of COVID-19 on U.S electricity generation and the emissions of CO_2 and NO_x due to this sector, from January to December 2020, by separating out the impacts of weather and long-term trends of fuel-mix transition. In section 4.2, a multivariate adaptive regression splines (MARS) model is presented and used to estimate daily electricity generation for major interconnection regions as a function of various indicators such as outdoor weather, day of week, and holidays. In section 4.3, our estimates of reductions in electricity generation due to COVID-19 are presented. In section 4.4, the impacts of COVID-19 on power sector emissions of NO_x and CO_2 are presented, in relation to recent trends in fuel-mix transition in the U.S. power sector.

4.2 Electricity Generation and Outdoor Temperature

The U.S. power system comprises three major grids: Western, Eastern, and Texas Interconnections. Within each interconnection, regional balancing authorities manage electricity supply to match demand, while the three interconnections operate independently with limited exchange of electricity (de Chalendar et al., 2019). In this study, data for electricity generation as well as emissions of CO_2 and NO_x are obtained from the U.S. Environmental Protection Agency Air Markets Program Data (EPA AMPD) and the U.S. Energy Information Administration (EIA) (EIA, 2020e; EPA, 2020a). To account for variability in weather, heating degree days (HDD, base

temperature 65°F) and cooling degree days (CDD, base temperature 65°F) data are obtained from the National Oceanic and Atmospheric Administration (NOAA) Climate Prediction Center (NOAA CPC, 2020). To represent the Western Interconnection, the power sector and HDD/CDD data are aggregated for the following states: Washington, Oregon, Idaho, California, Nevada, Utah, Arizona, Colorado, New Mexico, Montana, Wyoming (hereafter 'West', brown area in Figure 4.1g). Similar data for all other states in the Contiguous U.S. (CONUS) are aggregated to represent the Eastern and Texas Interconnections (hereafter 'East & Texas', purple area in Figure 4.1g). For the aggregation of state-level HDD/CDD data, CDD values are weighted by state populations and HDD values are weighted by the number of state-wide electricity heating households. Section 4.6.1 describes the aggregation processes of the power sector and HDD/CDD data.

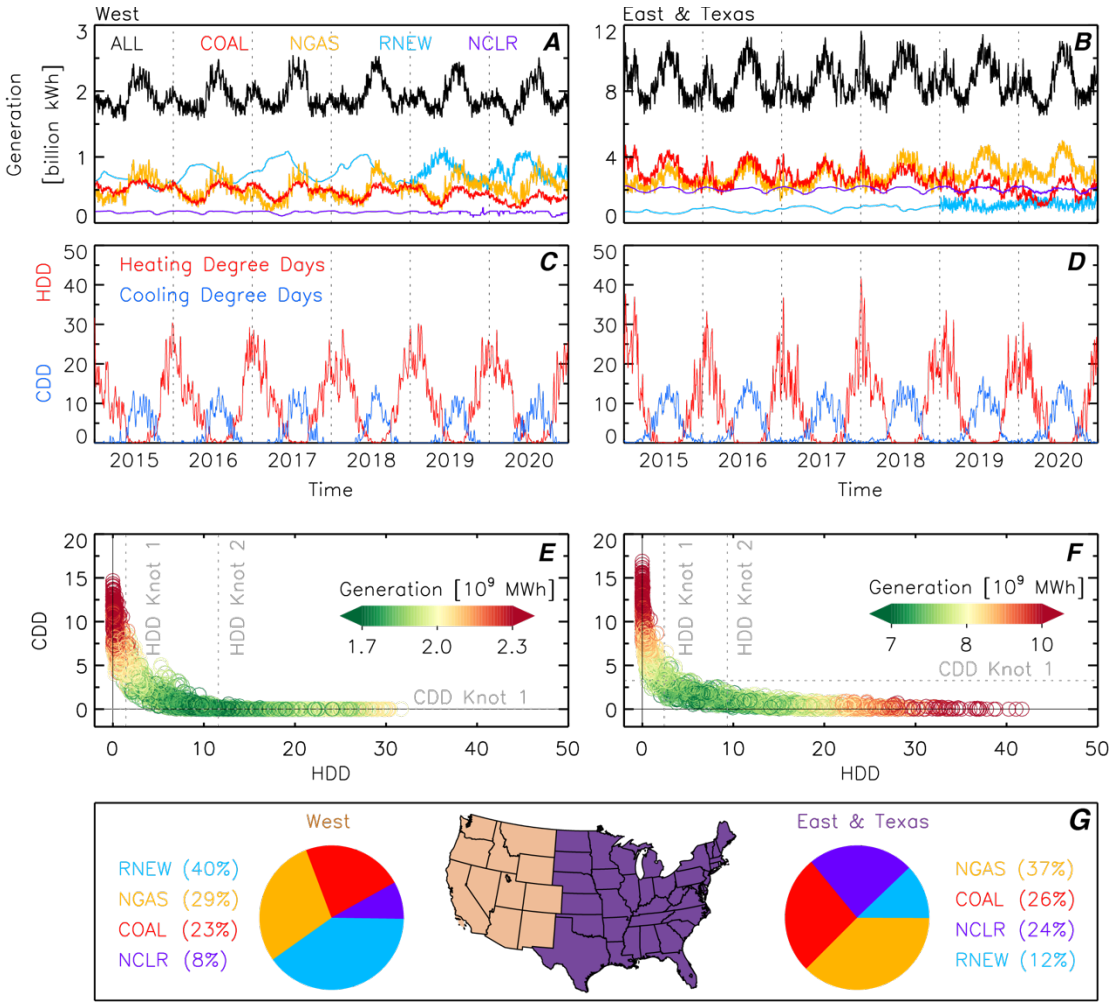

Figure 4.1. Electricity generation and outdoor temperature. Left panels are for the West (A, C, E), and right panels are for the East & Texas (B, D, F). (A, B) Time series of daily electricity generation from four energy sources: Coal, natural gas (NGAS), nuclear (NCLR), and renewables (RNEW) (Source: EPA, EIA). The total generation is shown as a black line (ALL). (C, D) Heating degree days (HDD, base temperature 65°F) and cooling degree days (CDD, base temperature 65°F) averaged for 3-days (Source: NOAA CPC). (E, F) Scatter plots of electricity generation as a function of 3-day running mean of HDD and CDD for 2015 to 2019. Vertical and horizontal gray lines indicate knot (cut point) values determined for a multivariate adaptive regression spline model (MARS-ELEC, Equation 4.1 and Equation 4.2). (G) The geographic regions of the West (brown) and the East & Texas (purple). Pie charts show the electricity fuel-mix composition of each region for 2019.

Figures 4.1a and 4.1b show daily electricity generation for the West and East & Texas regions, from January 2015 to December 2020. Electricity generation in both regions shows a seasonal cycle, peaking in summer and winter. The heating degree

days (HDD) and cooling degree days (CDD), proxies of energy demand for spatial heating and cooling, are used for to account for variations in electricity generation due to weather (Beheshti et al., 2019; Chang et al., 2016). To account for the temporal lead and/or lag in the electricity demand in response to varying outdoor temperature, three-day running averages are applied to the HDD and CDD values. Figures 4.1c and 4.1d show three-day running means of HDD and CDD, which also exhibit seasonal cycles. Figures 4.1e and 4.1f show the variation of electricity generation as a function of HDD and CDD for the West and East & Texas regions, respectively, from January 2015 to December 2019. Scatter plots of electricity generation versus each of HDD and CDD, individually, are shown in Figure S4.1.

Several studies have shown that energy demand exhibits nonlinear relations with HDD and CDD: i.e., a response of energy demand (i.e. air conditioning) per degree increase in CDD is relatively higher at the temperature of 85°F (29°C) compared to a response at the temperature of 65°F (18°C) (Almuhtady et al., 2019; Giannakopoulos & Psiloglou, 2006; Harvey, 2020). Multivariate adaptive regression splines (MARS) is a numerical method used to investigate non-linear relationships in multi-dimensional data (Friedman, 1991; Friedman & Roosen, 1995). For MARS, a set of piecewise linear basis functions is used to model nonlinear relationships between a response variable and predictors. In this study, MARS is adopted to estimate daily electricity generation as a function of HDD, CDD, and an indicator for weekends and holidays. Regression coefficients are determined from the training data within the period of January 2015 to December 2019 (1826 days). The first two months of 2020 (i.e., prior to the COVID-19 outbreak) are excluded from the training data, as this period can be used for model

evaluation (Figure S2). Further description of the model is given in section 4.6.2. One MARS models is developed for the East & Texas (MARS-ELEC$^{E\&T}$, Equation 4.1) and a second for the West (MARS-ELEC^{WEST}, Equation 4.2). MARS-ELEC consists a set of linear basis functions ($[\pm(x-c)]_+$), a type of day variable (D_i), and the intercept as following:

$$\hat{E}_i^{E\&T} = 23019.4 \cdot \left[HDD_i^{E\&T} - 2.44149\right]_+ + 98905.1 \cdot \left[HDD_i^{E\&T} - 9.37323\right]_+ + 255143 \cdot \left[CDD_i^{E\&T} - 3.27758\right]_+ - 254489 \cdot \left[3.27758 - CDD_i^{E\&T}\right]_+ - 610111 \cdot D_i + 8{,}013{,}300 + \varepsilon_i \quad (4.1)$$

$$\hat{E}_i^{West} = 15484.3 \cdot [HDD_i^{West} - 1.41964]_+ + 34468.5 \cdot [1.41964 - HDD_i^{West}]_+ + 20524 \cdot [11.5554 - HDD_i^{West}]_+ + 44397.7 \cdot [CDD_i^{West} - 0.0447815]_+ + 606041 \cdot [0.0447815 - CDD_i^{West}]_+ - 107065 \cdot D_i + 1{,}590{,}820 + \varepsilon_i \quad (4.2)$$

$$where\ [x-c]_+ = \begin{cases} x-c, & if\ x \geq c \\ 0, & if\ x < c \end{cases} \quad and \quad [c-x]_+ = \begin{cases} c-x, & if\ x < c \\ 0, & if\ x \geq c \end{cases}$$

where i represents date and $E\&T$ indicates the East & Texas. Variable $\hat{E}$ is a model estimate of total electricity generation for each region, HDD and CDD are heating degree days and cooling degree days averaged in three-day running windows. The values of c are knots (cut point) of the basis function ($[\pm(x-c)]_+$), which partition the data into disjoint regions (Equation 4.2). Variable D_i is 0 for regular weekdays and 1 for weekends, federal holidays, and four additional days (the last day of year, the day after Thanksgiving, and the day before and after Christmas). Variable ε_i is the error component. The two standard deviations (2σ) of residuals for the period of January 2015 to December 2019, shown in Figure S2, are determined as the uncertainty range of the model estimate during 2020 (orange area in Figure 2a-c). The generalized R^2 of

the model estimates of electricity generation versus reported values is 0.95 for MARS-ELEC$^{E\&T}$ and 0.91 for MARS-ELEC^{WEST} for the training set data (January 2015 – December 2019, Figure S4.2b and S4.2c).

4.3 Impact of COVID-19 on Electricity Generation in the U.S. Power Sector

We use MARS-ELEC$^{E\&T}$ and MARS-ELEC^{WEST} (Equation 4.1 and 4.2) to estimate the business-as-usual (BAU, i.e., No COVID-19 outbreak) electricity generation for the East & Texas and the West. In Figures 4.2b and 4.2c, the orange lines show our estimate of the BAU electricity generation from January to December 2020. For the first two months of 2020, prior to the major outbreak of COVID-19 in the CONUS, the BAU estimate of electricity generation shows excellent agreement with the actual generation reported by EPA (combustion-based units) and the EIA (nuclear and renewable units), with the mean percentage error (MPE) of 0.1% for the East & Texas and 0.7% for the West. The MARS-ELEC performs well at reproducing patterns of higher generation for colder days (higher HDD) and lower generation on weekends and holidays. On 19 March 2020 the state of California issued its first state-wide stay-at-home order, and total of 44 states in CONUS and the District of Columbia were under partial or full lockdown by 7 April 2020 (NGA, 2020). The impact of COVID-19 on electricity generation becomes apparent around mid-March, as daily generation reported by EPA and EIA show decreased values compared to the BAU values. For the East & Texas, the weekly reduction in generation peaked at 9 ± 2 % (5.0 ± 1.2 billion kWh) during the third calendar week of April (04/13 – 04/19). For the West, the weekly reduction peaked at 15 ± 3 % (1.9 ± 0.3 billion kWh) during the

second calendar week of April (04/06 – 04/12) (Figures 4.2e and 4.2f). For the entire CONUS, the total electricity generation during April 2020 was 258.7 ± 0.1 billion kWh, which is 9 ± 1 % lower than our BAU estimate (Figure 4.2d). This value is also the lowest April level in the 20 years for which EIA records are available (1991-2020). In mid-April, the reduction in electricity generation due to COVID-19 begin to mitigate for both regions. The West showed a faster return to the BAU level than the East & Texas. In August 2020, a modest resurgence of reduced generation is seen in the West (Figure 4.2f), while electricity generation remained at the BAU level in the East & Texas (Figure 4.2e).

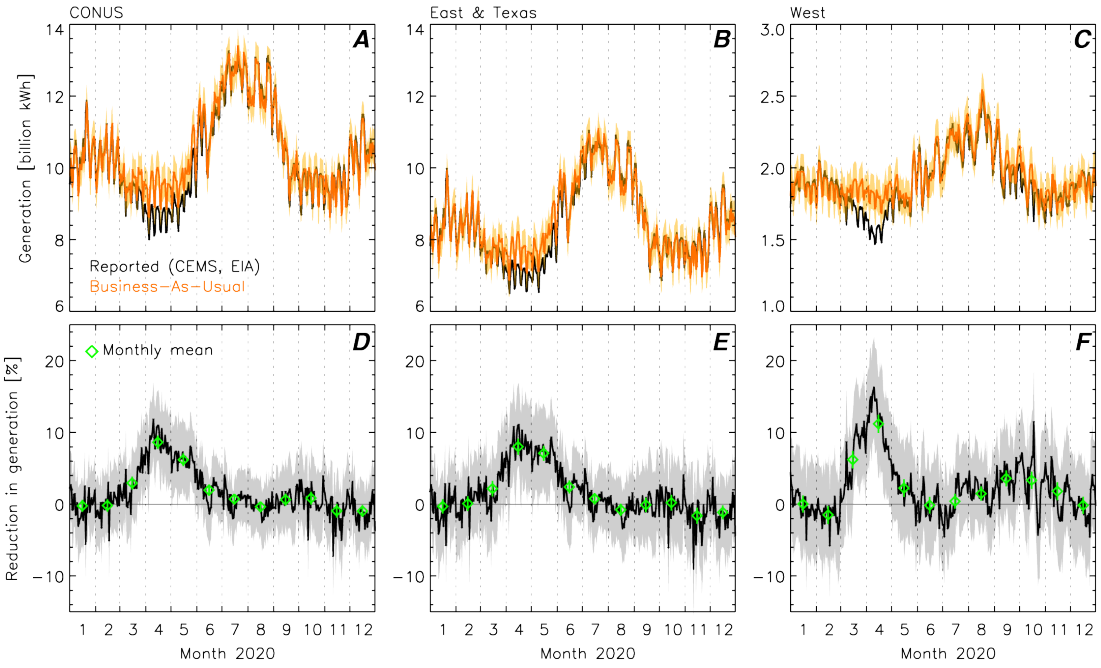

Figure 4.2. Impact of COVID-19 on electricity generation. The left panels are for the CONUS (A, D), the middle panels are for East & Texas (B, E), and the right panels are for West (C, F). Upper panels show daily electricity generation in 2020 (A, B, C). The black lines indicate actual generation reported by EPA (combustion-based units) and EIA (nuclear and renewables units). The orange lines indicate our BAU estimate of electricity generation, found as a function of outdoor temperature and type of day indicator (MARS-ELEC, Equations 4.1 and 4.2). Orange shaded areas are the uncertainty range of BAU generation, determined as the 2σ of model residuals for the five-year training dataset (see Materials and Methods). For the lower panels, the black

lines show the percentage reduction of actual generation relative to the BAU (D, E, F), and gray areas are 2σ uncertainty range. Positive numbers reflect reduced generation. Green diamonds and error bars show monthly mean reductions in electricity generation and the 2σ uncertainty, respectively.

4.4 Impact of COVID-19 on Emissions of CO_2 and NO_x from the U.S. Power Sector

We now focus on quantification of reductions in emissions of CO_2 and NO_x due to COVID-19. The emission of CO_2 and NO_x varies with the fuel-mix composition of power units affected by COVID-19. The unit commitment optimization in the generation of electricity (i.e., matching demand at minimum cost) is a complex process governed by generation costs, technical constraints on unit operations, electrical grid transmissions, and financial and regulatory conditions (van Ackooij et al., 2018; Siler-Evans et al., 2012; Takriti et al., 1996). The U.S. electricity network consists of traditionally regulated markets (Northwest, Southwest, and Southeast) and competitive wholesale electricity markets (Northeast, Midwest, Texas, and California) (FERC, 2020). For traditionally regulated markets, wholesale bilateral trading of electricity is common during times of need (de Chalendar et al., 2019). For competitive markets, lower marginal cost units (solar, wind, hydro, geothermal, nuclear) receive priority in dispatch compared to higher marginal cost units (coal and natural gas), until demand is met (Borenstein & Bushnell, 2015).

In this study, decline in electricity generation due to COVID-19 (Figure 4.2) is attributed to changes in the operation of coal-fired and natural gas-fired units. The business-as-usual (BAU) emissions of CO_2 from NO_x from power units in the East & Texas are estimated as following:

$$CO_{2,BAU}{}_m^{E\&T} = CO_2{}_m^{E\&T} + \left(\Delta E_{coal}{}_m^{E\&T} * \frac{CO_{2,coal}{}_m^{E\&T}}{E_{coal}{}_m^{E\&T}}\right) + \left(\Delta E_{gas}{}_m^{E\&T} * \frac{CO_{2,gas}{}_m^{E\&T}}{E_{gas}{}_m^{E\&T}}\right) \quad (4.3)$$

$$NO_{x,BAU}{}_m^{E\&T} = NO_{x}{}_m^{E\&T} + \left(\Delta E_{coal}{}_m^{E\&T} * \frac{NO_{x,coal}{}_m^{E\&T}}{E_{coal}{}_m^{E\&T}}\right) + \left(\Delta E_{gas}{}_m^{E\&T} * \frac{NO_{x,gas}{}_m^{E\&T}}{E_{gas}{}_m^{E\&T}}\right) \quad (4.4)$$

where m is a month of 2020 and E&T indicates the East & Texas. Analogs of Equation 4.3 and Equation 4.4 are also used to estimate BAU emissions of CO_2 and NO_x from power units in the West. Variables $CO_2{}_m^{E\&T}$ and $NO_x{}_m^{E\&T}$ are the monthly emissions of CO_2 and NO_x reported by EPA Air Markets Program Data (AMPD); Variables $E_{coal}{}_m^{E\&T}$ and $E_{gas}{}_m^{E\&T}$ are monthly electricity generation from coal-fired and gas-fired units reported by EPA AMPD; variables $\Delta E_{coal}{}_m^{E\&T}$ and $\Delta E_{gas}{}_m^{E\&T}$ are the reduction in the electricity generation due to COVID-19 for coal-fired units and gas-fired units, respectively. To determine variables $\Delta E_{coal}{}_m^{E\&T}$ and $\Delta E_{gas}{}_m^{E\&T}$, daily operational status of power units listed in the EPA AMPD are analyzed from 1 January to 12 August 2020 (225 days, Figure S4.3). This EPA AMPD data lists 400 coal-fired units and 2,036 gas-fired units in the East & Texas, and lists 67 coal-fired units and 510 gas-fired units for the West region. This span of 225 days is divided into three time-bins, each with 75 days (Period A: January 1–March 15, B: March 16–May 29, C: May 30–August 12, 2020). Then, a subset of power units which pass the following three conditions are selected as a proxy of power units affected by COVID-19 (hereafter CV19 units): 1) units that operated more than a day for both period A and period C (i.e., before and after the COVID-19 lockdown); 2) units that were shut-off for the entire period B (in the midst of COVID-19 lockdown); 3) units that operated more than a day for each of the three 75 days period for 2019 (January 1 – March 15, March 16 – May 29, May 30 – August 12, 2019). Of the selected CV19 units, the mean and two standard deviation of the percentage compositions in electricity generation from coal-fired versus gas-

fired CV19 units are computed for the period A and C (i.e., $E_{coal}^{CV19}/(E_{coal}^{CV19} + E_{gas}^{CV19})$). For the East & Texas, the computed mean and the two standard deviation are 58 ± 15 % (coal) and 42 ± 15% (gas), and these values are determined as the fuel composition of reduced electricity generation: $\Delta {E_{coal}}_m^{E\&T} = ({E_{BAU}}_m^{E\&T} - E_m^{E\&T}) * 0.58$ and $\Delta {E_{gas}}_m^{E\&T} = ({E_{BAU}}_m^{E\&T} - E_m^{E\&T}) * 0.42$. For the West region, the fuel compositions are determined as 54 ± 25 % (coal) and 46 ± 25 % (gas). The 2σ uncertainty range of business-as-usual emissions of CO_2 and NO_x (orange areas in Figure 4.3) are determined by propagating uncertainties associated with each term in Equation 4.3 and Equation 4.4, as detailed in section 4.6.3.

Figure 4.3 shows monthly electricity generation over the CONUS and concomitant emissions of CO_2 and NO_x from January to December 2020. For the first two months of 2020, BAU estimates of emissions of CO_2 and NO_x (the orange lines in Figure 4.3) show good agreement with reported emissions (the black lines in Figure 4.3), having a mean percentage error (MPE) of 0.4% for CO_2 and 0.5% for NO_x. From March to June 2020, emissions of CO_2 and NO_x are significantly less than the BAU estimate, with the reductions peaking in April 2020. For the CONUS in April 2020, our estimate of the decline in the emission of CO_2 due to COVID-19 is 18.3 ± 3.8 $MTCO_2$ (18 ± 4%), whereas the decline in the emission of NO_x due to COVID-19 is 10.5 ± 2.4 thousand metric tons (22 ± 5%). Table S4.1 summarizes the impacts of COVID-19 on electricity generation and concomitant emissions of CO_2 and NO_x for CONUS, East & Texas, and West from March to December 2020.

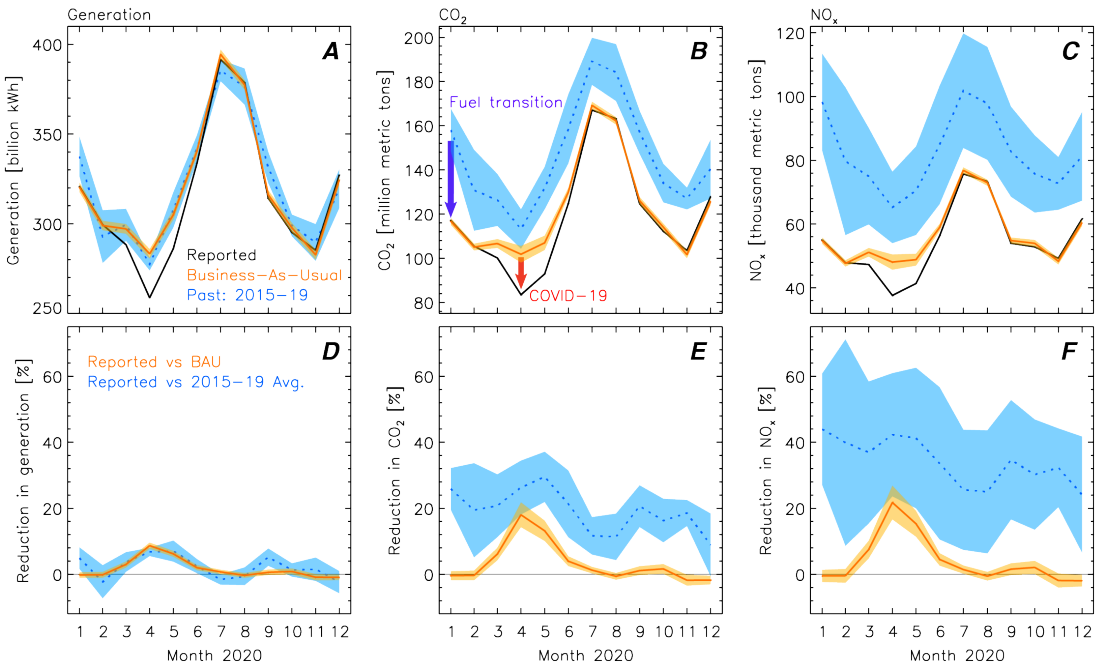

Figure 4.3. Impact of COVID-19 on the U.S. power sector. The monthly electricity generation (A, D), CO_2 emissions (B, E), and NO_x emissions (C, F) from power units in the CONUS. Upper panels show the monthly generation and emissions of CO_2 and NO_x in 2020 (A, B, C). Black lines indicate emissions reported by EPA. The orange lines indicate emissions estimated for the business-as-usual (BAU) scenario (i.e., without COVID-19 outbreak), using the MARS-ELEC and the analysis of power unit operation status (see Figure S4.3). The orange shaded area shows a 2σ uncertainty range. Blue dotted line and area indicate the mean and the standard deviation of each variable from 2015 to 2019. Lower panels show percentage reductions of the reported values relative to the BAU estimates (orange) and the past 5-year average values (blue) (D, E, F). Same formatted figures for the East & Texas and the West regions are shown in Figures S4.4 and S4.5.

In recent years, the U.S. power sector has seen trends of increasing natural gas and renewables and decreasing coal in fuel-mix profiles (see section 4.1, Figure 4.1, and Figure S4.6). Figure 4.3 shows the improvements in the emission intensities of CO_2 and NO_x achieved by the recent fuel transition in the U.S. power sector. The monthly emissions of NO_x in 2020 (black line) are always lower compared to the monthly emissions averaged for the previous five years (2015-2019, the blue dotted line in Figure 4.3c), while electricity generation has not shown a notable decrease relative to

five years mean (the blue dotted line in Figure 4.3a). As a whole for the CONUS, emission of NO_x during April 2020 decreased by 27.6 thousand metric tons (42%) from the average emission of April 2015-2019. Such reduction is ~2.6 times greater than the reduction induced by COVID-19 (10.5 ± 2.4 thousand metric tons). Also, the emission of CO_2 in April 2020 declined by 29.8 $MTCO_2$ (26%) from the average emission of April 2015-2019; a reduction 1.6 times greater than the impact of COVID-19 on the same month. These results suggest that using uncorrected prior year emissions as a baseline will result in an overestimation of the impact of COVID-19, given the recent downward trends in the emissions of CO_2 and NO_x from the U.S. power sector.

Liu et al. (2020) and Le Quéré et al. (2020) assessed the impact of COVID-19 on sector-specific CO_2 emissions (power, transport, industry, residential, etc.) across the globe in near-real time. Our study is more focused on a single sector (power) in a single country (the U.S.). According to Liu et al. (2020), U.S. power sector emissions of CO_2 declined by 66.3 $MTCO_2$ during the first half of 2020. Our study suggests the decline is 43.2 ± 6.1 $MTCO_2$ for the first six months of 2020. Two factors might contribute to the greater decline reported in Liu et al. (2020). First, Liu et al. (2020) used CO_2 emission intensity for 2019 to calculate emissions for 2020. Our analysis shows significant improvements in the CO_2 emission intensity for the U.S. power sector, even from 2019 to 2020 (Figure S4.6). Second, Liu et al. (2020) corrected power generation for temperature differences between 2019 and 2020. The temperature corrections are only applied to the countries that show good correlation between daily power generation and temperature ($R^2 > 0.5$). Such temperature correction may have not been applied to the U.S. power sector data, as Supplementary Figure 1 in Liu et al.

(2020) shows a significant decline in electricity generation during January and February 2020, prior to major outbreak of COVID-19. Le Quéré et al. (2020) reported that U.S. emission of CO_2 declined by 207 (112 to 314) $MTCO_2$ from January to April 2020 for the following six sectors: power, industry, surface transport, public buildings and commerce, residential, and aviation. They calculated the U.S. power sector CO_2 emissions for 2020 by multiplying the emissions for 2019 to fractional changes in weather-corrected electricity demand for the same weeks between 2019 and 2020. This approach also does not account for the decline in emission intensity in the U.S. power sector.

4.5 Conclusions

In this study we estimate the impact of COVID-19 on electricity generation and concomitant emissions of CO_2 and NO_x for the CONUS, East & Texas (geographical proxy of the Eastern and the Texas Interconnections, purple area in Figure 4.1g), West (geographical proxy of the Western Interconnections, brown area in Figure 4.1g). As a whole for the CONUS, we estimate that electricity generation in April 2020 decreased by $9 \pm 1\%$ (24.6 ± 2.6 billion kWh) as a direct result of COVID-19 restrictions, reaching the lowest April level in the past 20 years. Due to the reduced generation of electricity in April 2020, monthly emissions of CO_2 from the power sector are estimated to have fallen by $18 \pm 4\%$ (18.3 ± 3.8 $MTCO_2$). The size of reduction in CO_2 emission in April 2020 is comparable to the total amount of fossil-fuel CO_2 ($FFCO_2$) emitted from the State of Pennsylvania during April 2019 (16.9 $MTCO_2$), according to the Open-Source Data Inventory for Anthropogenic CO_2 (ODIAC2020, Oda & Maksyutov (2020)).

Emissions of NO_x from the power sector in April 2020 are estimated to have fallen by 22 ± 5% (10.5 ± 2.4 thousand metric tons) due to COVID-19.

We show that both outdoor temperature and the recent trend of fuel transitions in the U.S. power sector play significant roles in the emissions of CO_2 and NO_x. Improvements in emission intensities of CO_2 and NO_x for the U.S. power sector are shown in section 4.4 (Figure 4.3 and Figure S4.6). Power sector emission of NO_x in February 2020 is 40% lower compared to the average emission of NO_x for February 2015-2019, while the electricity generation in February 2020 is 2% greater than the average generation for February 2015-2019. This result implies that using emissions from previous years as a baseline will introduce bias into the quantification of the impact of COVID-19 on the U.S. power sector emission.

There are several limitations to our study. First, we analyzed the daily operation status of 3,013 coal-fired and gas-fired electricity generating units to attribute the observed reductions in electricity generation to specific fuel-sources. More detailed source attribution would require the use of dispatch and economic models, which could address complicated questions such as what would be the price of coal and natural gas if there had not been a global outbreak of COVID-19? Second, impacts of COVID-19 on the U.S. power sector at finer scale (i.e., hourly load, sector-specific demand) are not considered. Third, our study analyzed the direct impact of COVID-19 (i.e., reduced electricity demand due to change in human activities), while indirect impacts of COVID-19, such as delay in construction, maintenance, retirement of power plants, are not considered. We hope the limitations mentioned above will be addressed in the future by studies conducted at finer spatial, temporal, and sectoral scales than

considered here. Despite these limitations, our study provides a reliable assessment of the direct impact of COVID-19 on electricity generation and concomitant emissions of CO_2 and NO_x, by accounting for both meteorology and the recent trend of fuel transitions.

4.6 Supporting Information

4.6.1 Input data processing: Electricity generation, HDD, and CDD

Electricity generation data for combustion-based units (i.e., coal, gas, oil, etc.) and concomitant emissions of CO_2 and NO_x are obtained from the U.S. Environmental Protection Agency's Air Markets Program Data (EPA AMPD) website using customized data queries (EPA, 2020a). Unit-level daily operation data under the Acid Rain Program (ARP), for the period of 1 January 2015 to 31 December 2020, are used. ARP consists of electric generating units (EGUs) which have nameplate capacity greater than 25 MW, with few occasional exceptions (i.e., some non-EGUs were required to report operation data during 2003-2008 and still report data due to state requirements). In 2018, EPA AMPD data covered ~96% of the fossil fuel electricity generation in the U.S. (EPA, 2017). Gross load in the EPA AMPD dataset are converted into net load using the table of conversion factors in page 16 of Electric Power Monthly, Appendix C, Technical notes (EIA, 2020d). For "Combustion turbine" units, net load are computed by multiplying a fixed ratio of 0.98 to gross load values. For other unit types (i.e., "Combined-cycle" and "boilers"), net load was computed by multiplying a fixed ratio of 0.97 to gross load. The "primary fuel" column of the EPA AMPD dataset is used to categorize the unit-level daily net load for each fuel source.

If a "primary fuel" list two fuels (i.e., coal and pipeline natural gas), the given net load value is apportioned to each fuel by comparing the NO_x emission intensity of the given unit to the monthly average NO_x emission intensities of units using each of the two fuels.

Electricity generation data for non-combustion units (i.e., geothermal, hydroelectric conventional, nuclear, solar thermal & photovoltaic, and wind) are obtained from EIA power monthly (EIA, 2020e). State-level monthly net electricity generation data is temporally disaggregated into daily resolution using two methods. For the period of January 2019 to December 2020, the monthly generation by each fuel source is disaggregated into daily bins by multiplying daily temporal scaling factors from the Hourly Electric Grid Monitor dataset (EIA, 2020f). For the period of January 2015 to December 2018, EIA Hourly Electric Grid Monitor data are not available. For this period, state-level monthly net generation by each fuel-type is divided by the number of days in a given month and are allocated into the middle days of months (i.e., the 15^{th} day for 30-days month, the 16^{th} day for 31-days month). Then, allocated daily generation are linearly interpolated to determine daily generation for the remaining days of the month. The monthly sum of interpolated daily generation is matched to the original monthly generation by adding the daily mean difference to each day.

State-level daily heating degree days (HDD, base temperature 65°F) and cooling degree days (CDD, base temperature 65°F) data are obtained from National Oceanic and Atmospheric Administration Climate Prediction Center website (NOAA CPC, 2020). To account for the temporal lead and/or lag in electricity demand in response to varying weather, three-day running averages are applied to state-level daily

HDD and CDD values. Next, the HDD and CDD values for the Western Interconnection (West) as a whole are determined as the population-weighted average of HDD and CDD values for the following 11 states: Washington, Oregon, Idaho, California, Nevada, Utah, Arizona, Colorado, New Mexico, Montana, Wyoming. The HDD and CDD data for remaining 37 states in the CONUS plus the District of Columbia are aggregated, again using population weighting, to represent the Eastern and the Texas Interconnections (East & Texas). For these aggregations of state-level CDD data, CDD for each state is weighted by the ratio of state population to the regional total population ($CDD_{Day,i}^{West} = \sum_{j=1}^{11} CDD_{Day,i}^{State,j} * P_{Day,i}^{State,j} / P_{Day,i}^{West}$, where P is the population). Annual state-level population data are obtained from U.S. Census Bureau website (Census, 2019). For the aggregation of state-level HDD data, HDD for each state is weighted by the ratio of the state-wide electricity heating households to the regional total electricity heating households ($HDD_{Day,i}^{West} = \sum_{j=1}^{11} HDD_{Day,i}^{State,j} * PE_{Day,i}^{State,j} / PE_{Day,i}^{West}$, where PE is the number of electricity heating households). The number of households using electricity as the primary space heating fuel (PE) is obtained from the Table WF01 of the Short-Term Energy Outlook published by EIA on January 2021 (EIA, 2020h).

4.6.2 Multivariate Adaptive Regression Splines (MARS)

The Multivariate Adaptive Regression Splines (MARS) is a nonparametric regression technique that implements piecewise linear basis functions for each regressor variable (Friedman & Roosen, 1995). Linear basis functions are presented in the form of $[x - c]_+$ or $[c - x]_+$ as follows:

$$[x-c]_+ = \begin{cases} x-c, & if\ x \geq c \\ 0, & if\ x < c \end{cases} \quad and \quad [c-x]_+ = \begin{cases} c-x, & if\ x < c \\ 0, & if\ x \geq c \end{cases}$$

The use of numerous functions with unique break point values (knot, *c*) allows this piece-wise linear model to simulate highly nonlinear relationships. The python package "py-earth", which implements Jerome Friedman's MARS algorithm, is used to build our MARS regression models described by Equations 4.1 and 4.2 (Rudy et al., 2020). The forward pass and the pruning pass of the MARS algorithm determines a set of regression terms by minimizing the squared error of the training set and the generalized cross-validation (GCV) score. The GCV score is defined as $GCV = RSS/(N(1 - \frac{ENP}{N})^2)$, where *RSS* is the residual sum of squares of the training data, *ENP* is the effective number of parameters, and *N* is the number of training response data points. A more detailed description of the "py-earth" package can be found in https://contrib.scikit-learn.org/py-earth/content.html. For both the West as well as the East & Texas regions, the daily total electricity generation for the period of 1 January 2015 to 31 December 2019 is used as the training response variable (E_i, unit: MWh). The regional HDD, CDD, and the type of day indicator for the same period are used as training predictors (HDD_i, CDD_i, D_i). The type of day variable (D_i) is assigned a default value of 0, and is set to 1 for the following days: weekends, U.S. federal holidays (U.S. Office of Personnel Management, 2020), and four additional days: the day after Thanksgiving, the days before and after Christmas, and the last day of year). The maximum number of linear basis function terms is set to six to prevent overfitting and computational memory shortage (max_terms=6).

4.6.3 The uncertainty of business-as-usual emissions of CO_2 and NO_x

The 2σ uncertainty range of business-as-usual emissions of CO_2 and NO_x ($i.e., {CO_2}_{BAU}{}_m^{E\&T}$, ${NO_x}_{BAU}{}_m^{E\&T}$, orange areas in Figure 4.3) are determined by propagating uncertainties associated with each term in Equation 4.3 and Equation 4.4. The uncertainties of the reported emissions of CO_2 and NO_x (${CO_2}_m^{E\&T}$ and ${NO_x}_m^{E\&T}$) are determined by propagating the hourly Relative Accuracy Test Audit (RATA) uncertainty of 28% (2σ) assigned to each unit, as detailed in Ahn et al. (Ahn et al., 2020). The 2σ uncertainty of the terms $\Delta {E_{coal}}_m^{E\&T}$ and $\Delta {E_{gas}}_m^{E\&T}$ are determined by propagating uncertainties of the following components: 1) the two standard deviation of the MARS-ELEC residuals for the training dataset from January 2015 to December 2019 (${E_{BAU}}_m^{E\&T}$, Figure S4.2); 2) the ±2% accuracy in hourly electricity metering ($E_m^{E\&T}$) based on American National Standard for Electric meters (Nice, 2015), 3) the 2σ uncertainty for the mean fuel composition of electricity from CV19 units during the periods A and C (±15% for the East & Texas and ±25% for the West).

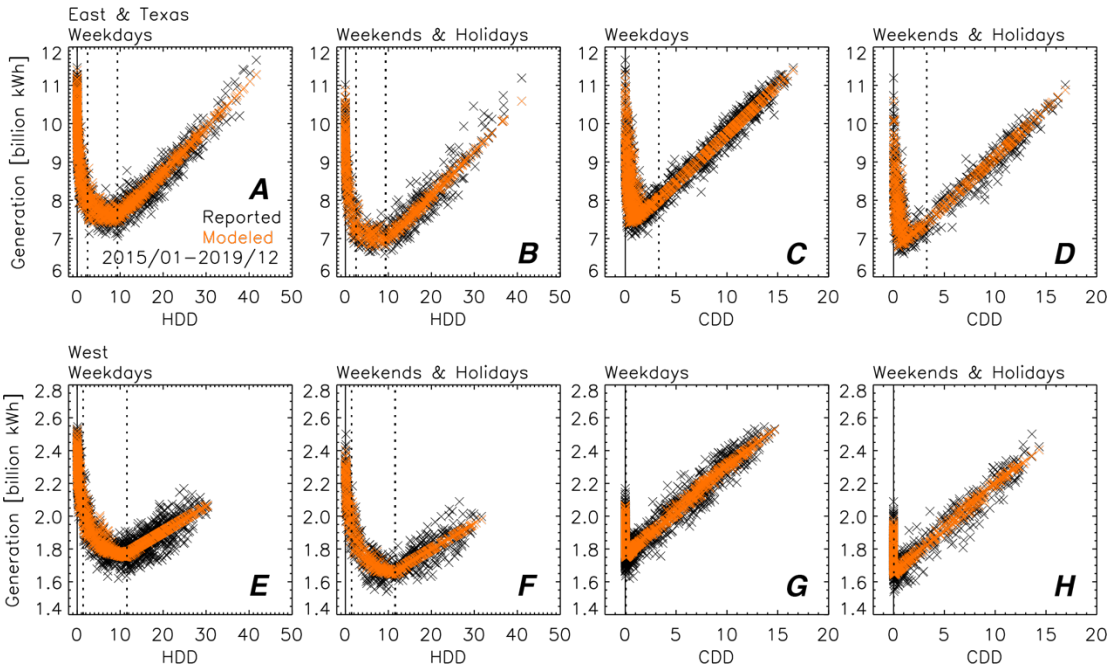

Figure S4.1. Scatter plots of daily net electricity generation versus HDD and CDD for the period of January 2015 to December 2019. Upper panels are for the East & Texas and the lower panels are for the West. Data for weekends & holidays are shown separately from weekdays to highlight the impact of type of day on electricity generation. Black 'X' symbols indicate net generation values reported by EPA and EIA (see Section 4.6.1). Orange 'X' symbols show the MARS-ELEC model estimate of net generation (Equations 4.1 and 4.2).

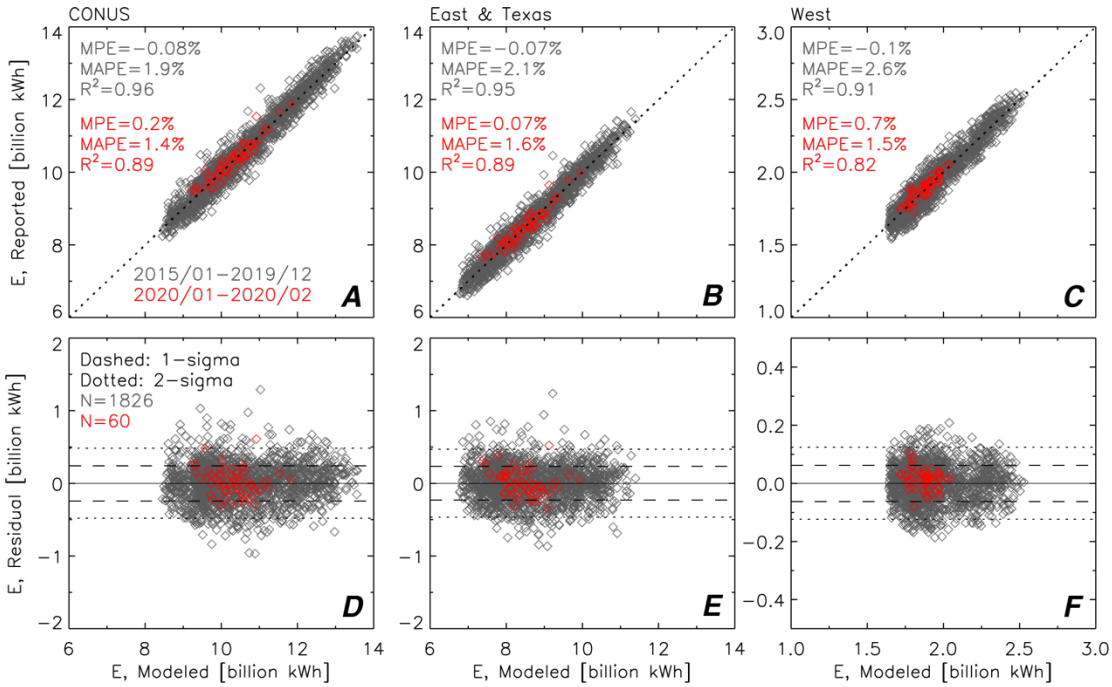

Figure S4.2. MARS-ELEC model performance evaluation for the CONUS (a, d), East & Texas (b, e), and the West (c, f). Upper panels show the scatter plot of the daily generation estimated by MARS-ELEC model versus the daily generation reported by EPA AMPD and EIA (see Section 4.6.1). In this study, one MARS-ELEC model is developed for the East & Texas region and another for the West (Equations 4.1 and 4.2). For the CONUS region, daily generation estimated from the both MARS-ELEC models are summed. Grey diamonds indicate daily electricity generation for the period of January 2015 to December 2019 used as training dataset to build the MARS-ELEC models. Red diamonds indicate daily generation data from January to February 2020, which are excluded from the model training dataset and also occur prior to the major outbreak of COVID-19 in the U.S. The mean percentage error (MPE), the mean absolute percentage error (MAPE), and R-squared values (based on the correlation of modeled versus measured electricity generation) are shown for each upper panel. Lower panels show the residuals of the MARS-ELC estimate (i.e., modeled minus measured electricity generation) as a function of our modeled estimate of daily electricity generation. Dashed and dotted horizontal lines indicate one standard deviation and two standard deviation of the residuals for the model training data points (January 2015 – December 2019).

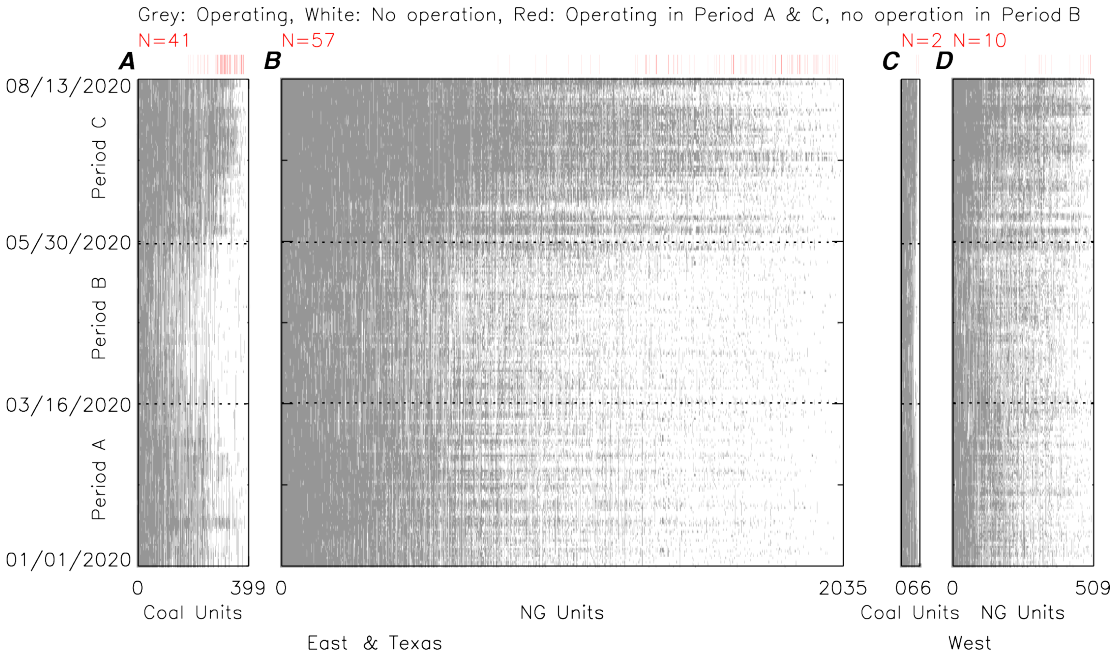

Figure S4.3. Operating status of coal-fired electricity generating units (a, c) and gas-fired units (b, d) for the East & Texas (a, b) and the West (c, d) from 1 January 2020 to 12 August 2020 (225 days). The 225 days are binned into 3 consecutive periods, each having 75 days (Period A, B, C along Y-axis). The abscissa of the plot shows the list of coal-fired and gas-fired units included in the EPA AMPD dataset for both regions. Grey colors indicate operating days and white colors indicate shut-off days (no electricity generated). Red vertical bars are shown above a subset of electricity generating units which were operating during period A and C but shut-off during period B, and thus selected as proxy for the units affected COVID-19 (CV19 units) (see Section 4.6.3 for more details). The total number of the CV19 units (red bars) are shown on the top of each panel.

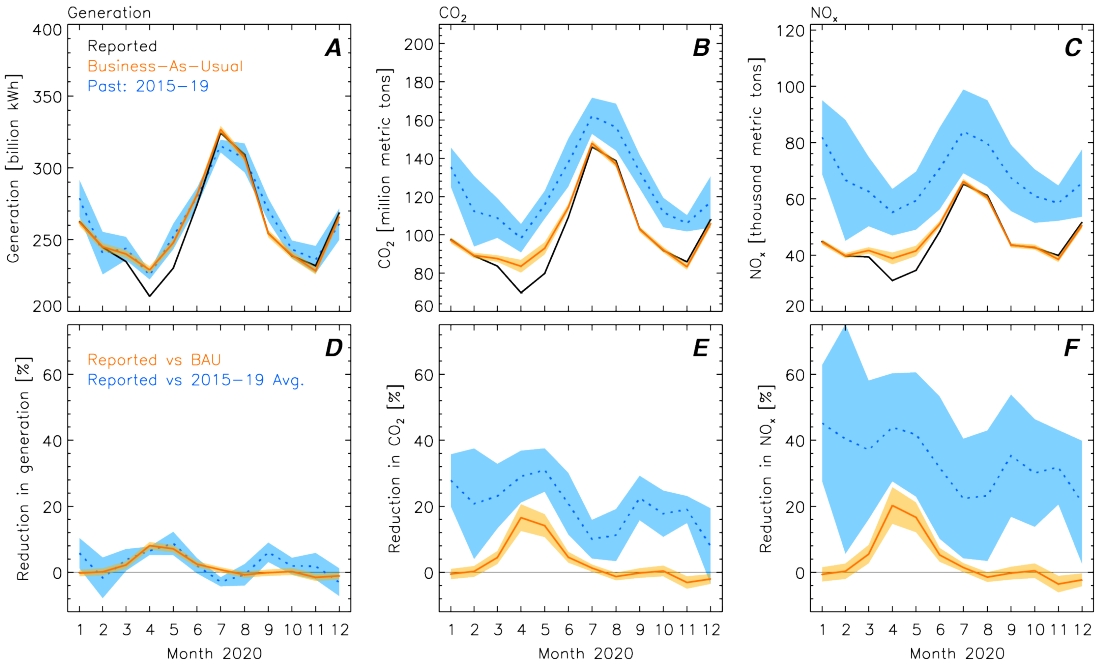

Figure S4.4. Same as Figure 4.3, but for the East & Texas region.

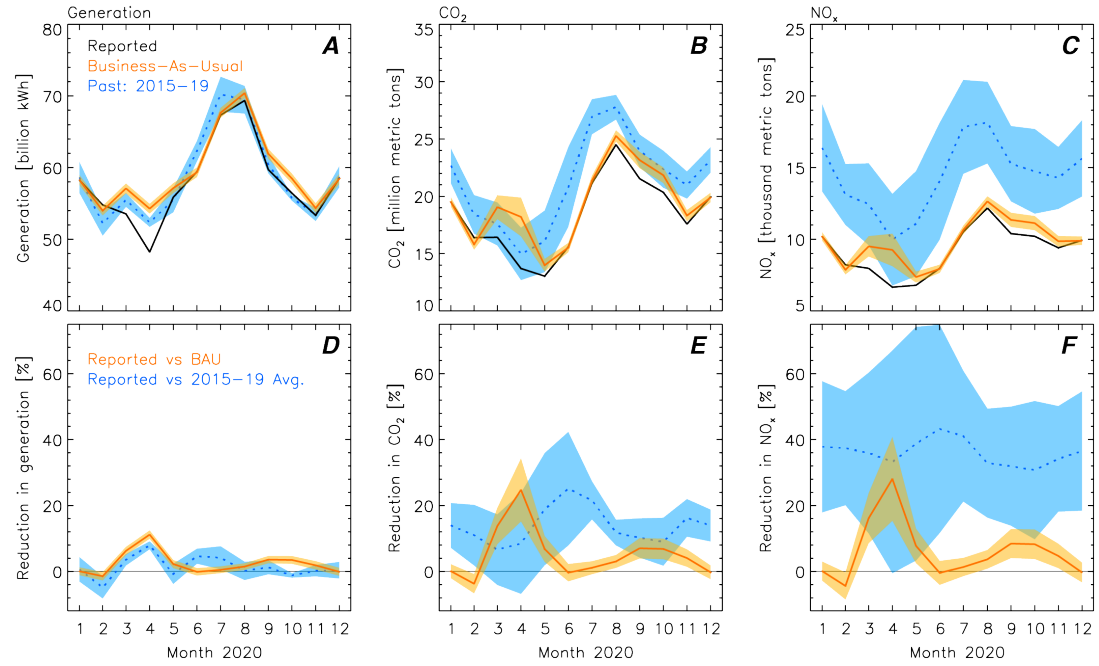

Figure S4.5. Same as Figure 4.3, but for the West region.

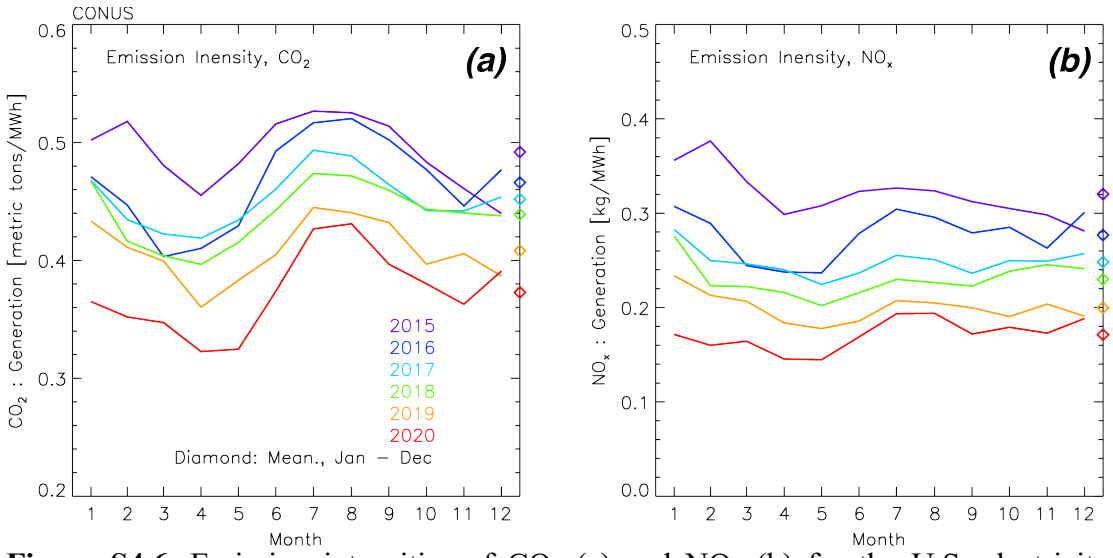

Figure S4.6. Emission intensities of CO_2 (a) and NO_x (b) for the U.S. electricity generation sector calculated from the EPA AMPD dataset. Monthly time series are shown for 2015 to 2020, with specific colors for each year (as indicated). Diamond symbol on the ordinate of both panels indicate the annual mean emission intensity.

Table 4.1. The impact of COVID-19 on the electricity generation and emissions of CO_2 and NO_x. Our estimates of the impact of COVID-19 are shown for the CONUS, East & Texas, and West regions (see Figure 4.1g for the geographic area for each region) from March to December 2020. The upper parts of the table show the absolute differences of reported values compared to business-as-usual estimates. The lower parts show the relative differences.

	ΔGeneration [10^9 kWh]			ΔCO_2 [10^6 MT]			ΔNO_x [10^3 MT]		
	CONUS	E&T	WEST	CONUS	E&T	WEST	CONUS	E&T	WEST
2020-03	−8.8	−5.3	−3.6	−6.5	−3.9	−2.6	−3.8	−2.3	−1.5
2020-04	−24.6	−18.5	−6.1	−18.3	−13.8	−4.5	−10.5	−7.9	−2.6
2020-05	−18.9	−17.6	−1.3	−14.1	−13.1	−0.9	−7.5	−6.9	−0.6
2020-06	−6.8	−6.9	0.1	−5.1	−5.2	0.1	−2.6	−2.7	0.0
2020-07	−2.8	−2.5	−0.3	−2.1	−1.9	−0.2	−1.1	−1.0	−0.1
2020-08	1.3	2.4	−1.0	1.0	1.8	−0.8	0.4	0.9	−0.5
2020-09	−1.9	0.3	−2.2	−1.4	0.2	−1.6	−0.8	0.1	−1.0
2020-10	−2.5	−0.5	−2.0	−1.9	−0.4	−1.5	−1.1	−0.2	−0.9
2020-11	2.5	3.5	−1.0	1.8	2.6	−0.7	0.9	1.4	−0.5
2020-12	3.0	2.9	0.1	2.2	2.2	0.1	1.2	1.2	0.0
Total	−59.5	−42.1	−17.3	−44.4	−31.6	−12.8	−24.9	−17.3	−7.6
	ΔGeneration [%]			ΔCO_2 [%]			ΔNO_x [%]		
	CONUS	E&T	WEST	CONUS	E&T	WEST	CONUS	E&T	WEST
2020-03	−3.0	−2.2	−6.2	−6.1	−4.5	−13.8	−7.5	−5.5	−16.1
2020-04	−8.7	−8.1	−11.2	−18.0	−16.6	−24.7	−21.7	−20.2	−28.1
2020-05	−6.2	−7.1	−2.2	−13.2	−14.1	−6.8	−15.3	−16.6	−7.7
2020-06	−2.0	−2.4	0.1	−4.0	−4.5	0.4	−4.5	−5.2	0.4
2020-07	−0.7	−0.8	−0.5	−1.3	−1.3	−1.1	−1.4	−1.4	−1.3
2020-08	0.3	0.8	−1.5	0.6	1.3	−3.0	0.6	1.5	−3.7
2020-09	−0.6	0.1	−3.6	−1.1	0.2	−7.0	−1.5	0.3	−8.4
2020-10	−0.8	−0.2	−3.5	−1.6	−0.4	−6.8	−2.1	−0.5	−8.2
2020-11	0.9	1.6	−1.9	1.8	3.1	−4.0	1.9	3.6	−4.7
2020-12	0.9	1.1	0.1	1.8	2.0	0.3	2.0	2.3	0.3
Total	−1.8	−1.6	−2.9	−3.6	−3.0	−6.5	−4.3	−3.7	−7.6

Chapter 5: Conclusions

5.1 Summary

In this dissertation, I quantified the emissions of CO_2 and two other co-emitted air pollutants (i.e., CO and NO_x) from the cities (i.e., the Baltimore, MD-Washington, D.C. area, Chapter 2 and 3) and the U.S. power sector (i.e., electricity generating units in the contiguous U.S., Chapter 4). As detailed further below, Chapter 2 has been published, Chapter 3 will be submitted once all of the co-authors have had a chance to provide comments, Chapter 4 will be submitted for publication soon after the defense of this dissertation.

In Chapter 2, the emissions of CO_2 from the Baltimore, MD-Washington, D.C. area (the Balt-Wash area) were investigated using aircraft data collected during February 2015. The accuracy, precision, and sensitivity of CO_2 emissions estimates from the mass balance approach were assessed for both power plants and cities. Our estimates of CO_2 emissions from two local power plants agreed well with their Continuous Emissions Monitoring Systems (CEMS) records. For the 16 power plant plumes captured by the aircraft, the mean percentage difference of CO_2 emissions was −0.3%, with the aircraft estimates smaller than the CEMS records. For the Balt-Wash area as a whole, the 1σ CO_2 emission rate uncertainty for any individual aircraft-based mass balance approach experiment was estimated to be ±38%. Treating the seven mass balance experiments conducted in nine days as an individual quantification of the Balt-Wash CO_2 emissions, the estimated uncertainty was ±16% (standard error of the mean

at 95% CL). Our aircraft-based estimate was compared to various bottom-up fossil fuel CO_2 ($FFCO_2$) emission inventories. Based on the FLAGG-MD aircraft observations, we estimate 1.9 ± 0.3 MtC of $FFCO_2$ from the Balt- Wash area during February 2015. The mean estimate of $FFCO_2$ from the four bottom-up models was 2.2 ± 0.3 MtC, which was in agreement to our top-down estimate within the 1σ uncertainty range. Chapter 2 was published on 14 April 2020 in the *Journal of Geophysical Research - Atmospheres* (Ahn et al., 2020).

In Chapter 3, the emissions of CO_2 and CO from the Balt-Wash area during COVID-19 period were quantified using aircraft data collected during February-May 2020. The aircraft-based mass balance approach, adopted and evaluated in Chapter 2, was used to quantify the reductions in the emissions of CO_2 and CO during the COVID-19 pandemic. Our mass balance estimates indicated that the emission rate of CO_2 over the Balt-Wash area declined by 32% in April and by 29% in May 2020, relative to the February 2020 mean (i.e., prior to COVID-19 social lockdowns). Our analysis indicates the emission rate of CO declined by 37% in April and 30% in May, relative to the February 2020 mean. Our source attribution analysis determined that the onroad transportation sector to be the largest contributor to reduced emission rates in April 2020. Next, we evaluated three bottom-up emission inventories (i.e., EDGAR, state of Maryland inventory, NEI), using our top-down estimates of the emissions of CO_2 and CO. For February 2020, prior to wide-spread of COVID-19 in the U.S., we found that EDGARv50's estimates of the CO_2 emissions were 18% lower than our aircraft top-down estimates, and that the state of Maryland bottom-up inventory estimated of the emission of CO_2 was 13% lower than our estimate. For the EDGARv50, we identified

the onroad sector as the major source of the underestimation of the emission of CO_2. For the state of Maryland inventory, we determined that the nonroad transportation sector is the major source of the underestimation of CO_2 emission. For the emissions of CO, we found that EDGARv50's estimates were 54% larger than our top-down estimates, and NEI's estimates were 66% larger than our top-down estimates in February 2020 (i.e., prior to COVID-19 social measures in the U.S.). We identified the onroad transportation sector as the largest contributor to the overestimation of the emission of CO by EDGAR, and the nonroad transportation sector as the largest contributor to the overestimate for the CO emission provided by the NEI bottom-up inventory during February 2020, prior to COVID-19 outbreak in the U.S. The results of Chapter 3 are being prepared for journal submission, which will occur soon after the dissertation defense.

In Chapter 4, the emissions of CO_2 and NO_x from the U.S. power sector during 2020 were investigated using power plant operation data from EPA and EIA. The impact of COVID-19 on U.S. electricity generation and emissions of CO_2 and NO_x were assessed by quantifying impacts of weather, weekends and holidays, and recent trends in fuel mix. A multivariate adaptive regression splines (MARS) model was used to account for the impacts of outdoor temperature and type of day. The emission of NO_x in April 2020 for power plants in the Contiguous U.S. (CONUS) was 42% (27.6 thousand metric tons) lower than the average emission during April 2015-2019. However, we showed that using prior years as a baseline will overestimate the impact of COVID-19 on power plant emissions, given the recent downward trend in the emissions of CO_2 and NO_x from the U.S. power sector due to changes in fuel-mix. The

daily operational status of 3,013 power units was analyzed to account for the fuel-mix change (i.e., switching from coal to natural gas). For the CONUS, we estimated the direct impacts of COVID-19 in April 2020 to be declines of 9±1% (24.6±2.6 billion kWh) on electricity generation, 18±4% (18.3±3.8 $MTCO_2$) on the emission of CO_2, and 22±5% (10.5±2.4 thousand metric tons) on the emission of NO_x. The results of Chapter 4 are being prepared for journal submission, which will occur soon after the dissertation defense.

5.2 Recommendations for Future Research

Throughout this body of work, considerable progress was made towards the quantification of the emissions of CO_2, CO, and NO_x from cities (Chapter 2, 3) and the U.S. power sector (Chapter 4). Even though this dissertation represents substantial progress, there nonetheless exist numerous opportunities to further extend these research topics.

In Chapter 2, I showed that the emissions of CO_2, computed using the aircraft-based mass balance method, are most sensitive to the following three parameters: 1) variability of wind speed and wind direction; 2) planetary boundary layer (PBL) height; 3) background mole fraction of CO_2. The precision of the top-down CO_2 emissions estimates can be significantly improved by conducting research flights when wind speed and wind direction are consistent throughout the day. Both the HYSPLIT run with the high-resolution meteorological model (i.e., HRRR) and the wind visualization website (i.e., https://earth.nullschool.net) are useful resources to assess wind conditions during the flight planning process. Regular calibrations of aircraft wind measurements,

using either the wind profiler or the modeled wind data, are recommended to ensure the accuracy the aircraft wind data (Ahn et al., 2020; Ren et al., 2019). As of 2021, three wind profiler sites exist in the Balt-Wash area (i.e., Horn Point on the Eastern Shore, the Howard University Beltsville site, and Piney Run in Western Maryland) and wind observation data from these sites are available upon request (MDE, 2021).

The uncertainty associated with the PBL height was the second important parameter for the mass balance calculation of CO_2 flux. The uncertainty in the PBL height estimate is often driven from the spatiotemporal variability of the PBL heights around the study domain. This uncertainty can be effectively reduced by conducting multiple vertical profiles during a research flight. Conducting the missed approach (i.e., sampling near-surface air masses) at least once during a flight is also recommended. Also, evaluating the aircraft-based PBL height estimate against independent platform estimates, such as Lidar remote sensing, can reduce the uncertainty in the top-down method. The Atmospheric Lidar Group at the University of Maryland, Baltimore County (UMBC) manages and provides the PBL height data measured by the Ceilometer network (Caicedo et al., 2017). Sampling through the boundary layer close to this lidar stating would provide an important check on the inference of the height of the PBL based upon airborne measurements of chemical tracers.

The uncertainty associated with the background mole fraction of CO_2 was the third important parameter for the mass balance calculation. The accuracy of background CO_2 determined using edge fitting method needs to be evaluated. The mole fraction of CO_2 measured upwind of the cities can be used to evaluate background CO_2, by pairing upwind and downwind measurements using the transport model (Ahn

et al., 2020). For this upwind-to-background CO_2 comparison, both upwind and downwind flight legs are recommended to be conducted during mid-afternoon hours so that the difference in PBL heights is at minimum. The simultaneous deployment of two aircraft would provide a great opportunity to better constrain background CO_2, and hence reduced the uncertainty in top-down determination of CO_2 flux. Also, we found that the edge fitting method could not be applied for some downwind flight legs, as distinctions between the urban plume and the rural background were not evident. To prevent such occurrences, extending downwind flight legs far from the urban center as much as resources allow is recommended, especially for cities such as the Balt-Wash area where the urban-to-rural gradient can be ambiguous.

In Chapter 3, I compared the top-down emissions of CO_2 and CO for February 2020 to the top-down emissions for February 2015. Our top-down estimate of the CO_2 emission rate for February 2020 was 13% lower than the top-down estimate for February 2015. Also, our top-down estimate of the CO emission rate for February 2020 was 7% lower than the top-down estimate for February 2015 (Ren et al., 2018). Even though these comparisons showed that both the emissions of CO_2 and CO from the Balt-Wash area decreased between 2015 and 2020, a detailed trend analysis for urban emissions was not conducted. The atmospheric chemistry group at the University of Maryland has conducted more than 70 aircraft research flights over the Balt-Wash area from 2015 to 2020. These aircraft measurements, spanning 6 years, can be analyzed using the top-down method presented in this dissertation to quantify trends of the urban emissions. Such top-down estimates of trends of the emissions of CO_2 and CO can be compared to the trends described in the followings: 1) the state of Maryland inventory

(i.e., the state inventory has been published every three year since 2011); 2) The Community Multiscale Air Quality Modeling (CMAC) output for CO over the Balt-Wash area. The research capability to estimate trends of urban GHG emissions using atmospheric measurements (i.e., the top-down method) will benefit policy makers and stakeholders by providing an independent means to: 1) evaluate the effectiveness of emission reduction policies from various sectors; 2) track progress toward GHG reduction targets for the state of Maryland, which are often set in relative terms.

Throughout this body of work, atmospheric measurement data obtained from aircraft research flights were extensively used to quantify emissions of CO_2 from the Balt-Wash area. Although the aircraft research platform was designed to study urban emissions, several limitations exist. One of the major challenges in analyzing aircraft data and relating to policy is the temporal intermittency of the flights, because emissions vary within a day (i.e., day vs night), a week (weekday vs weekends), and a year (winter vs summer). In this dissertation, diurnal and weekly temporal profiles of fossil fuel CO_2 driven from bottom-up models were used to relate our aircraft-based top-down estimate to bottom-up inventories. For future work, atmospheric measurements data obtained from other platforms (i.e., low-cost sensors, tall towers, or satellite remote sensing) could be synthesized with aircraft data to overcome data intermittency. Pisso et al. (2019) quantified the emissions of CO_2 from the Tokyo area for winters from 2005 to 2009 using the Bayesian inversion technique. In Pisso et al. (2019), in-situ measurements of CO_2 from the following three platforms were collectively used as an input to their inversion model: 1) the Comprehensive Observation Network for TRace gases by AIrLiner (CONTRAIL) aircraft flights; 2)

a tall tower with inlets located at 25, 100, and 200 m; 3) two surface sites hosted by the Japan Meteorological Agency. Also, Cusworth et al. (2020) combined atmospheric measurements of methane from the following three platforms over the Los Angeles basin: surface in-situ measurements sites, mountaintop retrievals from the CLARS-FTS instrument, and the space-based TROPOMI methane retrievals. By combining measurements of methane from multiple observing platforms into one framework, enhanced spatiotemporal sensitivity of the resulting emission of methane was achieved.

The Balt-Wash area is the urban test bed site designated by NIST to develop scientific methods for quantifying GHG emissions (Whetstone, 2018). As of 2021, a total of 12 ground towers in the Balt-Wash area are in operation, each measuring atmospheric mole fractions of CO_2 and CH_4 continuously (Karion et al., 2020). The NASA's OCO-2 satellite, which has revisit time of 16 days, has been measuring column-averaged dry-air mole fraction of CO_2 around the globe since 2015 (Crisp et al., 2017). The OCO-3 satellite, launched in 2019, is capable of scanning large areas (80×80 km^2) to measure column CO_2 on a single overpass (i.e., "snapshot" mode). Synthesizing atmospheric measurements from these platforms (i.e., ground towers, satellites) will provide better understanding for the CO_2 emissions from the Balt-Wash and their temporal variations (i.e., diurnal, weekly, and seasonal patterns).

Bibliography

van Ackooij, W., Danti Lopez, I., Frangioni, A., Lacalandra, F., & Tahanan, M. (2018). Large-scale unit commitment under uncertainty: an updated literature survey. *Annals of Operations Research*, *271*(1), 11–85. https://doi.org/10.1007/s10479-018-3003-z

Ahn, D. Y., Hansford, J. R., Howe, S. T., Ren, X. R., Salawitch, R. J., Zeng, N., et al. (2020). Fluxes of Atmospheric Greenhouse-Gases in Maryland (FLAGG-MD): Emissions of Carbon Dioxide in the Baltimore, MD-Washington, D.C. Area. *Journal of Geophysical Research: Atmospheres*, *125*(9), e2019JD032004. https://doi.org/https://doi.org/10.1029/2019JD032004

Almuhtady, A., Alshwawra, A., Alfaouri, M., Al-Kouz, W., & Al-Hinti, I. (2019). Investigation of the trends of electricity demands in Jordan and its susceptibility to the ambient air temperature towards sustainable electricity generation. *Energy, Sustainability and Society*, *9*(1), 39. https://doi.org/10.1186/s13705-019-0224-1

Alvarez, R. A., Zavala-Araiza, D., Lyon, D. R., Allen, D. T., Barkley, Z. R., Brandt, A. R., et al. (2018). Assessment of methane emissions from the U.S. oil and gas supply chain. *Science*, *361*(6398), 186–188. https://doi.org/10.1126/science.aar7204

American Veterinary Medical Association. (2012). U.S. Pet ownership statistics. Retrieved September 7, 2019, from https://www.avma.org/KB/Resources/Statistics/Pages/Market-research-statistics-US-pet-ownership.aspx

Ammoura, L., Xueref-Remy, I., Vogel, F., Gros, V., Baudic, A., Bonsang, B., et al. (2016). Exploiting stagnant conditions to derive robust emission ratio estimates for CO$_{2}$, CO and volatile organic compounds in Paris. *Atmospheric Chemistry and Physics*, *16*(24), 15653–15664. https://doi.org/10.5194/acp-16-15653-2016

Anderson, D. C., Loughner, C. P., Diskin, G., Weinheimer, A., Canty, T. P., Salawitch, R. J., et al. (2014). Measured and modeled CO and NOy in DISCOVER-AQ: An evaluation of emissions and chemistry over the eastern US. *Atmospheric Environment*, *96*, 78–87. https://doi.org/10.1016/j.atmosenv.2014.07.004

Andres, R. J., Boden, T. A., & Higdon, D. M. (2016). Gridded uncertainty in fossil fuel carbon dioxide emission maps, a CDIAC example. *Atmospheric Chemistry and Physics*, *16*(23). https://doi.org/10.5194/acp-16-14979-2016

Arrhenius, S. (1896). On the Influence of Carbonic Acid in the Air upon the Temperature of the Ground. Retrieved from https://www.rsc.org/images/Arrhenius1896_tcm18-173546.pdf

Asefi-Najafabady, S., Rayner, P. J., Gurney, K. R., McRobert, A., Song, Y., Coltin, K., et al. (2014). A multiyear, global gridded fossil fuel CO_2 emission data product: Evaluation and analysis of results. *Journal of Geophysical Research: Atmospheres*, *119*(17), 10,210-213,231. https://doi.org/10.1002/2013JD021296

Ashworth, K., Bucci, S., Gallimore, P. J., Lee, J., Nelson, B. S., Sanchez-Marroqu\'\in, A., et al. (2020). Megacity and local contributions to regional air

pollution: an aircraft case study over London. *Atmospheric Chemistry and Physics*, *20*(12), 7193–7216. https://doi.org/10.5194/acp-20-7193-2020

Balashov, N. V, Davis, K. J., Miles, N. L., Lauvaux, T., Richardson, S. J., Barkley, Z. R., & Bonin, T. A. (2020). Background heterogeneity and other uncertainties in estimating urban methane flux: results from the Indianapolis Flux Experiment (INFLUX). *Atmospheric Chemistry and Physics*, *20*(7), 4545–4559. https://doi.org/10.5194/acp-20-4545-2020

Beheshti, S., Sahebalam, A., & Nidoy, E. (2019). Structure dependent weather normalization. *Energy Science & Engineering*, *7*(2), 338–353. https://doi.org/10.1002/ese3.272

Bey, I., Jacob, D. J., Yantosca, R. M., Logan, J. A., Field, B. D., Fiore, A. M., et al. (2001). Global modeling of tropospheric chemistry with assimilated meteorology: Model description and evaluation. *Journal of Geophysical Research: Atmospheres*, *106*(D19), 23073–23095. https://doi.org/10.1029/2001JD000807

Borenstein, S., & Bushnell, J. (2015). The US Electricity Industry After 20 Years of Restructuring. *Annual Review of Economics*, *7*(1), 437–463. https://doi.org/10.1146/annurev-economics-080614-115630

Bréon, F. M., Broquet, G., Puygrenier, V., Chevallier, F., Xueref-Remy, I., Ramonet, M., et al. (2015). An attempt at estimating Paris area CO_2 emissions from atmospheric concentration measurements. *Atmos. Chem. Phys.*, *15*(4), 1707–1724. https://doi.org/10.5194/acp-15-1707-2015

C40. (2019). Defining Carbon Neutrality for cities and managing residual emissions. Cities perspective and guidance. Retrieved March 17, 2021, from https://c40-production-images.s3.amazonaws.com/researches/images/76_Carbon_neutrality_guidance_for_cities_20190422.original.pdf?1555946416

C40 Cities. (2020). *C40 Annual Report 2020*. Retrieved from https://c40-production-images.s3.amazonaws.com/other_uploads/images/2827_C40_annual_report_2020_16April2021.original.pdf?1618575743

Caicedo, V., Rappenglück, B., Lefer, B., Morris, G., Toledo, D., & Delgado, R. (2017). Comparison of aerosol lidar retrieval methods for boundary layer height detection using ceilometer aerosol backscatter data. *Atmospheric Measurement Techniques*, *10*(4), 1609–1622. https://doi.org/10.5194/amt-10-1609-2017

Cambaliza, M. O. L., Shepson, P. B., Caulton, D. R., Stirm, B., Samarov, D., Gurney, K. R., et al. (2014). Assessment of uncertainties of an aircraft-based mass balance approach for quantifying urban greenhouse gas emissions. *Atmospheric Chemistry and Physics*, *14*(17), 9029–9050. https://doi.org/10.5194/acp-14-9029-2014

Census (U.S. Census Bureau). (2019). Population, Population Change, and Estimated Components of Population Change: April 1, 2010 to July 1, 2019 (NST-EST2019-alldata). Retrieved January 30, 2021, from https://www2.census.gov/programs-surveys/popest/datasets/2010-2019/national/totals/nst-est2019-alldata.csv

de Chalendar, J. A., Taggart, J., & Benson, S. M. (2019). Tracking emissions in the US electricity system. *Proceedings of the National Academy of Sciences*,

116(51), 25497 LP – 25502. https://doi.org/10.1073/pnas.1912950116
Chang, Y., Kim, C. S., Miller, J. I., Park, J. Y., & Park, S. (2016). A new approach to modeling the effects of temperature fluctuations on monthly electricity demand. *Energy Economics*, *60*, 206–216. https://doi.org/https://doi.org/10.1016/j.eneco.2016.09.016
Chevallier, F., Viovy, N., Reichstein, M., & Ciais, P. (2006). On the assignment of prior errors in Bayesian inversions of CO2 surface fluxes. *Geophysical Research Letters*, *33*(13). https://doi.org/10.1029/2006GL026496
CIESIN (Center for International Earth Science Information Network), C. U. (2018). Gridded population of the world, version 4 (GPWv4): Population count, revision 11. https://doi.org/10.7927/H4JW8BX5
Comptroller of Maryland. (2020). Motor Fuel Tax And Motor Carrier Tax (IFTA) Annual Report: Fiscal Year 2020.
Conley, S. A., Faloona, I. C., Lenschow, D. H., Karion, A., & Sweeney, C. (2014). A Low-Cost System for Measuring Horizontal Winds from Single-Engine Aircraft. *Journal of Atmospheric and Oceanic Technology*, *31*(6), 1312–1320. https://doi.org/10.1175/JTECH-D-13-00143.1
Crippa, M, Guizzardi, D., Muntean, M., Schaaf, E., Dentener, F., van Aardenne, J. A., et al. (2018). Gridded emissions of air pollutants for the period 1970--2012 within EDGAR v4.3.2. *Earth System Science Data*, *10*(4), 1987–2013. https://doi.org/10.5194/essd-10-1987-2018
Crippa, Monica, Solazzo, E., Huang, G., Guizzardi, D., Koffi, E., Muntean, M., et al. (2020). High resolution temporal profiles in the Emissions Database for Global Atmospheric Research. *Scientific Data*, *7*(1), 121. https://doi.org/10.1038/s41597-020-0462-2
Crippa, Monica, Guizzardi, D., Muntean, M., & Schaaf, E. (2021). EDGAR v5.0 Global Air Pollutant Emissions. Retrieved April 1, 2021, from https://ec.europa.eu/jrc/en/publication/edgar-v50-global-air-pollutant-emissions
Crisp, D., Pollock, H. R., Rosenberg, R., Chapsky, L., Lee, R. A. M., Oyafuso, F. A., et al. (2017). The on-orbit performance of the Orbiting Carbon Observatory-2 (OCO-2) instrument and its radiometrically calibrated products. *Atmospheric Measurement Techniques*, *10*(1), 59–81. https://doi.org/10.5194/amt-10-59-2017
Crowell, S., Baker, D., Schuh, A., Basu, S., Jacobson, A. R., Chevallier, F., et al. (2019). The 2015-2016 Carbon Cycle As Seen from OCO-2 and the Global In Situ Network. *Atmos. Chem. Phys. Discuss.*, *2019*, 1–79. https://doi.org/10.5194/acp-2019-87
Cusworth, D. H., Duren, R. M., Yadav, V., Thorpe, A. K., Verhulst, K., Sander, S., et al. (2020). Synthesis of Methane Observations Across Scales: Strategies for Deploying a Multitiered Observing Network. *Geophysical Research Letters*, *47*(7), e2020GL087869. https://doi.org/https://doi.org/10.1029/2020GL087869
Davis, K. J., Deng, A., Lauvaux, T., Miles, N. L., Richardson, S. J., Sarmiento, D. P., et al. (2017). The Indianapolis Flux Experiment (INFLUX): A test-bed for developing urban greenhouse gas emission measurements. *Elem Sci Anth*, *5*(0), 21. https://doi.org/10.1525/elementa.188
Deng, A., Lauvaux, T., Davis, K. J., Gaudet, B. J., Miles, N., Richardson, S. J., et al. (2017). Toward reduced transport errors in a high resolution urban CO 2

inversion system. *Elem Sci Anth*, *5*.
DOEE (Department of Energy & Environment). (2018). Clean Energy DC. Retrieved April 10, 2019, from https://doee.dc.gov/cleanenergydc
Draxler, R., Hess, G. D., & Air Resources Laboratory (U.S.). (1997). Description of the HYSPLIT_4 modeling system. Retrieved January 17, 2019, from https://www.arl.noaa.gov/documents/reports/arl-224.pdf
Draxler, R., Stunder, B., Rolph, G., Stein, A., & Taylor, A. (2014). HYSPLIT4 user 's guide version 4 - Last revision: September 2014. NOAA. Retrieved from https://www.arl.noaa.gov/data/web/models/hysplit4/win95/user_guide.pdf
Duren, R. M., & Miller, C. E. (2012). Measuring the carbon emissions of megacities. *Nature Climate Change*, *2*(8), 560–562. https://doi.org/10.1038/nclimate1629
EEA (European Environment Agency). (2019). EMEP/EEA air pollutant emission inventory guidebook 2019: Technical guidance to prepare national emission inventories. Retrieved April 20, 2010, from http://www.eea.europa.eu/publications/emep-eea-guidebook-2013
EIA (U.S. Energy Information Administration). (2020a). *Daily electricity demand impacts from COVID-19 mitigation efforts differ by region*. Retrieved from https://www.eia.gov/todayinenergy/detail.php?id=43636#tab2
EIA (U.S. Energy Information Administration). (2020b). *Daily electricity demand in New York falls about 13% after COVID-19 mitigation efforts*. Retrieved from https://www.eia.gov/todayinenergy/detail.php?id=43635
EIA (U.S. Energy Information Administration). (2020c). Electric Power Annual, Table 3.1.A. Net generation by energy source: Total (all sectors).
EIA (U.S. Energy Information Administration). (2020d). Electric Power Monthly, Appendix C. Technical notes, (September), 1–31. Retrieved from https://www.eia.gov/electricity/monthly/pdf/technotes.pdf
EIA (U.S. Energy Information Administration). (2020e). Electric Power Monthly, Net Generation by State by Type of Producer by Energy Source (Source: EIA-923 Report). Retrieved December 21, 2020, from https://www.eia.gov/electricity/data/state/generation_monthly.xlsx
EIA (U.S. Energy Information Administration). (2020f). Hourly Electric Grid Monitor, Balancing Authority/Region Files: CAL, CAR, CENT, FLA, MIDA, MIDW, NE, NY, NW, SE, SW, TEN, TEX.
EIA (U.S. Energy Information Administration). (2020g). November 2020 Monthly Energy Review, Table 11.1-6. Carbon Dioxide Emissions From Energy Consumption. Retrieved from https://www.eia.gov/totalenergy/data/monthly/index.php#environment
EIA (U.S. Energy Information Administration). (2020h). Table WF01. Average Consumer Prices and Expenditure for Heating Fuels During the Winter. Number of households by primary space heating fuel (thousands). Retrieved January 11, 2021, from https://www.eia.gov/outlooks/steo/pdf/wf01.pdf
EIA (U.S. Energy Information Administration). (2021a). Natural Gas Consumption by End Use, Maryland, Monthly. Retrieved March 31, 2021, from https://www.eia.gov/dnav/ng/NG_CONS_SUM_DCU_SMD_M.htm
EIA (U.S. Energy Information Administration). (2021b). Power plant operating data, Form EIA-923 detailed data with previous form data (EIA-906/920). Retrieved

March 15, 2021, from https://www.eia.gov/electricity/data/eia923/
EPA (U.S. Environmental Protection Agency). (2010). U.S. EPA. Integrated Science Assessment (ISA) for Carbon Monoxide. Retrieved October 15, 2020, from https://cfpub.epa.gov/ncea/risk/recordisplay.cfm?deid=218686&CFID=78776911&CFTOKEN=81884369
EPA (U.S. Environmental Protection Agency). (2017). CAMD' s Power Sector Emissions Data Guide. Retrieved November 10, 2020, from https://www.epa.gov/airmarkets/camds-power-sector-emission-data-guide
EPA (U.S. Environmental Protection Agency). (2020a). "Air Markets Program Data." Washington, DC: Office of Atmospheric Programs, Clean Air Markets Division. Retrieved October 1, 2020, from https://ampd.epa.gov/ampd/
EPA (U.S. Environmental Protection Agency). (2020b). National Annual Emissions Trend: Criteria pollutants National Tier 1 for 1970-2019. Air Pollutant Emissions Trends Data. Retrieved December 15, 2020, from https://www.epa.gov/air-emissions-inventories/air-pollutant-emissions-trends-data
EPA (U.S. Environmental Protection Agency). (2021). 2017 National Emissions Inventory (NEI) Data. Retrieved March 17, 2021, from https://www.epa.gov/air-emissions-inventories/2017-national-emissions-inventory-nei-data
Fell, H., & Kaffine, D. T. (2018). The Fall of Coal: Joint Impacts of Fuel Prices and Renewables on Generation and Emissions. *American Economic Journal: Economic Policy*, *10*(2), 90–116. https://doi.org/10.1257/pol.20150321
Feng, S., Lauvaux, T., Newman, S., Rao, P., Ahmadov, R., Deng, A., et al. (2016). Los Angeles megacity: a high-resolution land–atmosphere modelling system for urban CO_2 emissions. *Atmos. Chem. Phys.*, *16*(14), 9019–9045. https://doi.org/10.5194/acp-16-9019-2016
FERC (Federal Energy Regulatory Commission). (2020). Electric Power Markets: National Overview. Retrieved December 21, 2020, from https://www.ferc.gov/industries-data/market-assessments/electric-power-markets
Friedman, J. H. (1991). Multivariate Adaptive Regression Splines. *Ann. Statist.*, *19*(1), 1–67. https://doi.org/10.1214/aos/1176347963
Friedman, J. H., & Roosen, C. B. (1995). An introduction to multivariate adaptive regression splines. *Statistical Methods in Medical Research*, *4*(3), 197–217. https://doi.org/10.1177/096228029500400303
Gately, C., & Hutyra, L. (2017). Large uncertainties in urban-scale carbon emissions. *Journal of Geophysical Research: Atmospheres*, *122*(20). https://doi.org/10.1002/2017JD027359
Gately, C., & Hutyra, L. (2018). CMS: CO2 Emissions from Fossil Fuels Combustion, ACES Inventory for Northeastern USA. ORNL DAAC, Oak Ridge, Tennessee, USA. ORNL Distributed Active Archive Center. https://doi.org/10.3334/ornldaac/1501
Gately, C. K., Hutyra, L. R., Wing, I. S., & Brondfield, M. N. (2013). A bottom up approach to on-road CO_2 emissions estimates: Improved spatial accuracy and applications for regional planning. *Environmental Science & Technology*, *47*(5), 2423–2430. https://doi.org/10.1021/es304238v
Gately, C. K., Hutyra, L. R., & Wing, I. S. (2015). Cities, traffic, and CO2: A

multidecadal assessment of trends, drivers, and scaling relationships. *Proceedings of the National Academy of Sciences of the United States of America*, *112*(16), 4999–5004. https://doi.org/DOI 10.1073/pnas.1421723112

Giannakopoulos, C., & Psiloglou, B. (2006). Trends in energy load demand for Athens, Greece: Weather and non-weather related factors. *Climate Research - CLIMATE RES*, *31*, 97–108. https://doi.org/10.3354/cr031097

Goldberg, D. L., Lu, Z., Oda, T., Lamsal, L. N., Liu, F., Griffin, D., et al. (2019). Exploiting OMI NO2 satellite observations to infer fossil-fuel CO2 emissions from US megacities. *Science of the Total Environment*, *695*, 133805.

Goldberg, D. L., Anenberg, S. C., Griffin, D., McLinden, C. A., Lu, Z., & Streets, D. G. (2020). Disentangling the Impact of the COVID-19 Lockdowns on Urban NO2 From Natural Variability. *Geophysical Research Letters*, *47*(17), e2020GL089269. https://doi.org/https://doi.org/10.1029/2020GL089269

Google. (2020). COVID-19 Community Mobility Reports. Retrieved March 30, 2021, from https://www.google.com/covid19/mobility/

de Gouw, J. A., Parrish, D. D., Frost, G. J., & Trainer, M. (2014). Reduced emissions of CO2, NOx, and SO2 from U.S. power plants owing to switch from coal to natural gas with combined cycle technology. *Earth's Future*, *2*(2), 75–82. https://doi.org/https://doi.org/10.1002/2013EF000196

Gratani, L., & Varone, L. (2005). Daily and seasonal variation of CO_2 in the city of Rome in relationship with the traffic volume. *Atmospheric Environment*, *39*(14), 2619–2624. https://doi.org/10.1016/j.atmosenv.2005.01.013

Grell, G. A., Peckham, S. E., Schmitz, R., McKeen, S. A., Frost, G., Skamarock, W. C., & Eder, B. (2005). Fully coupled "online" chemistry within the WRF model. *Atmospheric Environment*, *39*(37), 6957–6975. https://doi.org/10.1016/j.atmosenv.2005.04.027

Guan, D., Liu, Z., Geng, Y., Lindner, S., & Hubacek, K. (2012). The gigatonne gap in China's carbon dioxide inventories. *Nature Climate Change*, *2*(9), 672.

Gurney, K. (2018). Read me file of Hestia fossil fuel farbon dioxide (FFCO2) data product - Salt lake county, version 2.2, 0.002 degree grid. Retrieved May 10, 2019, from https://data.nist.gov/od/ds/696FD547910012A0E0532457068160E41910/readme.002deg.SLC.v2.2.txt

Gurney, K., Liang, J., Patarasuk, R., O'Keeffe, D., Huang, J., Hutchins, M., et al. (2017). Reconciling the differences between a bottom-up and inverse-estimated $FFCO_2$ emissions estimate in a large US urban area. *Elem Sci Anth*, *5*. https://doi.org/10.1525/elementa.137

Gurney, Kevin R, Huang, J., & Coltin, K. (2016). Bias present in US federal agency power plant CO_2 emissions data and implications for the US clean power plan. *Environmental Research Letters*, *11*(6), 64005. https://doi.org/10.1088/1748-9326/11/6/064005

Gurney, Kevin R, Liang, J., O'Keeffe, D., Patarasuk, R., Hutchins, M., Huang, J., et al. (2019). Comparison of global downscaled versus bottom-up fossil fuel CO_2 emissions at the urban scale in four US urban areas. *Journal of Geophysical Research: Atmospheres*, *124*(5), 2823–2840. https://doi.org/10.1029/2018JD028859

Gurney, Kevin Robert, Liang, J., Roest, G., Song, Y., Mueller, K., & Lauvaux, T. (2021). Under-reporting of greenhouse gas emissions in U.S. cities. *Nature Communications*, *12*(1), 553. https://doi.org/10.1038/s41467-020-20871-0

Hall, D. L., Anderson, D. C., Martin, C. R., Ren, X., Salawitch, R. J., He, H., et al. (2020). Using near-road observations of CO, NOy, and CO2 to investigate emissions from vehicles: Evidence for an impact of ambient temperature and specific humidity. *Atmospheric Environment*, *232*, 117558. https://doi.org/10.1016/j.atmosenv.2020.117558

Hardiman, B. S., Wang, J. A., Hutyra, L. R., Gately, C. K., Getson, J. M., & Friedl, M. A. (2017). Accounting for urban biogenic fluxes in regional carbon budgets. *Science of the Total Environment*, *592*, 366–372. https://doi.org/10.1016/j.scitotenv.2017.03.028

Harvey, L. D. D. (2020). Using modified multiple heating-degree-day (HDD) and cooling-degree-day (CDD) indices to estimate building heating and cooling loads. *Energy and Buildings*, *229*, 110475. https://doi.org/https://doi.org/10.1016/j.enbuild.2020.110475

Heimburger, A. M. F., Harvey, R. M., Shepson, P. B., Stirm, B. H., Gore, C., Turnbull, J., et al. (2017). Assessing the optimized precision of the aircraft mass balance method for measurement of urban greenhouse gas emission rates through averaging. *Elem Sci Anth*, *5*. https://doi.org/10.1525/elementa.134

Huang, Y., Kort, E. A., Gourdji, S., Karion, A., Mueller, K., & Ware, J. (2019). Seasonally resolved excess urban methane emissions from the Baltimore/Washington, DC metropolitan region. *Environmental Science & Technology*, *53*(19), 11285–11293.

Hutyra, L. R., Duren, R., Gurney, K. R., Grimm, N., Kort, E. A., Larson, E., & Shrestha, G. (2014). Urbanization and the carbon cycle: Current capabilities and research outlook from the natural sciences perspective. *Earths Future*, *2*(10), 473–495. https://doi.org/10.1002/2014ef000255

Ibarra-Espinosa, S., & Ynoue, R. (2016, May 24). REMI model: Bottom-up emissions inventories for cities with lack of data. Retrieved April 24, 2021, from http://www.scienpress.com/Upload/GEO/Vol 7_1_19.pdf

Idso, C. D., Idso, S. B., & Balling Jr, R. C. (2001). An intensive two-week study of an urban CO_2 dome in Phoenix, Arizona, USA. *Atmospheric Environment*, *35*(6), 995–1000. https://doi.org/10.1016/S1352-2310(00)00412-X

IEA (International Energy Agency). (2019). The Role of Gas in Today's Energy Transitions. *IEA, Paris*. https://doi.org/10.1071/aj18300

Jackson, R. B., Down, A., Phillips, N. G., Ackley, R. C., Cook, C. W., Plata, D. L., & Zhao, K. (2014). Natural gas pipeline leaks across Washington, DC. *Environ Sci Technol*, *48*(3), 2051–2058. https://doi.org/10.1021/es404474x

Jacob, D. J. (1999). Introduction to Atmospheric Chemistry: Chapter 7. The Greenhouse Effect. Retrieved April 15, 2021, from http://acmg.seas.harvard.edu/publications/jacobbook/index.html

Janssens-Maenhout, G., Crippa, M., Guizzardi, D., Muntean, M., Schaaf, E., Dentener, F., et al. (2017). EDGAR v4.3.2 Global atlas of the three major greenhouse gas emissions for the period 1970-2012. *Earth Syst. Sci. Data Discuss.*, *2017*, 1–55. https://doi.org/10.5194/essd-2017-79

Kalthoff, N., Corsmeier, U., Schmidt, K., Kottmeier, C., Fiedler, F., Habram, M., & Slemr, F. (2002). Emissions of the city of Augsburg determined using the mass balance method. *Atmospheric Environment*, *36*, S19–S31. https://doi.org/10.1016/S1352-2310(02)00215-7

Karion, A., Sweeney, C., Kort, E. A., Shepson, P. B., Brewer, A., Cambaliza, M., et al. (2015). Aircraft-based estimate of total methane emissions from the Barnett shale region. *Environmental Science & Technology*, *49*(13), 8124–8131. https://doi.org/10.1021/acs.est.5b00217

Karion, A., Callahan, W., Stock, M., Prinzivalli, S., Verhulst, K. R., Kim, J., et al. (2019). Greenhouse gas observations from the Northeast Corridor tower network. *Earth Syst. Sci. Data Discuss.*, *2019*, 1–29. https://doi.org/10.5194/essd-2019-206

Karion, A., Callahan, W., Stock, M., Prinzivalli, S., Verhulst, K. R., Kim, J., et al. (2020). Greenhouse gas observations from the Northeast Corridor tower network. *Earth Syst. Sci. Data*, *12*(1), 699–717. https://doi.org/10.5194/essd-12-699-2020

Keeling, C. D. (1973). Industrial production of carbon dioxide from fossil fuels and limestone. *Tellus*, *25*(2), 174–198. https://doi.org/10.3402/tellusa.v25i2.9652

Keller, C. A., Evans, M. J., Knowland, K. E., Hasenkopf, C. A., Modekurty, S., Lucchesi, R. A., et al. (2020). Global Impact of COVID-19 Restrictions on the Surface Concentrations of Nitrogen Dioxide and Ozone. *Atmospheric Chemistry and Physics Discussions*, *2020*, 1–32. https://doi.org/10.5194/acp-2020-685

Kim, S. Y., Millet, D. B., Hu, L., Mohr, M. J., Griffis, T. J., Wen, D., et al. (2013). Constraints on Carbon Monoxide Emissions Based on Tall Tower Measurements in the U.S. Upper Midwest. *Environmental Science & Technology*, *47*(15), 8316–8324. https://doi.org/10.1021/es4009486

Klausner, T., Mertens, M., Huntrieser, H., Galkowski, M., Kuhlmann, G., Baumann, R., et al. (2020). Urban greenhouse gas emissions from the Berlin area: A case study using airborne CO2 and CH4 in situ observations in summer 2018. *Elementa: Science of the Anthropocene*, *8*. https://doi.org/10.1525/elementa.411

Kort, E. A., Angevine, W. M., Duren, R., & Miller, C. E. (2013). Surface observations for monitoring urban fossil fuel CO2 emissions: Minimum site location requirements for the Los Angeles megacity. *Journal of Geophysical Research-Atmospheres*, *118*(3), 1–8. https://doi.org/DOI 10.1002/jgrd.50135

Kort, E. A., Frankenberg, C., Costigan, K. R., Lindenmaier, R., Dubey, M. K., & Wunch, D. (2014). Four corners: The largest US methane anomaly viewed from space. *Geophys. Res. Lett.*, 2014GL061503. https://doi.org/10.1002/2014GL061503

Krautwurst, S., Gerilowski, K., Jonsson, H. H., Thompson, D. R., Kolyer, R. W., Thorpe, A. K., et al. (2016). Methane emissions from a Californian landfill, determined from airborne remote sensing and in-situ measurements. *Atmos. Meas. Tech. Discuss.*, *2016*, 1–33. https://doi.org/10.5194/amt-2016-391

Laughner, J. L., Neu, J. L., Schimel, D., Wennberg, P. O., Barsanti, K., Bowman, K., et al. (2020). The 2020 COVID-19 pandemic and atmospheric composition: back to the future. https://doi.org/10.1002/essoar.10506081.1

Lauvaux, T., Miles, N. L., Deng, A., Richardson, S. J., Cambaliza, M. O., Davis, K.

J., et al. (2016). High-resolution atmospheric inversion of urban CO_2 emissions during the dormant season of the Indianapolis Flux Experiment (INFLUX). *Journal of Geophysical Research: Atmospheres*, *121*(10), 5213–5236. https://doi.org/10.1002/2015JD024473

Lin, J. C., Gerbig, C., Wofsy, S. C., Andrews, A. E., Daube, B. C., Davis, K. J., & Grainger, C. A. (2003). A near-field tool for simulating the upstream influence of atmospheric observations: The Stochastic Time-Inverted Lagrangian Transport (STILT) model. *Journal of Geophysical Research: Atmospheres*, *108*(D16).

Liu, Z., Guan, D., Wei, W., Davis, S. J., Ciais, P., Bai, J., et al. (2015). Reduced carbon emission estimates from fossil fuel combustion and cement production in China. *Nature*, *524*(7565), 335.

Liu, Z., Ciais, P., Deng, Z., Lei, R., Davis, S. J., Feng, S., et al. (2020). Near-real-time monitoring of global CO2 emissions reveals the effects of the COVID-19 pandemic. *Nature Communications*, *11*(1), 5172. https://doi.org/10.1038/s41467-020-18922-7

Lopez-Coto, I., Ghosh, S., Prasad, K., & Whetstone, J. (2017). Tower-based greenhouse gas measurement network design—The National Institute of Standards and Technology North East Corridor Testbed. *Advances in Atmospheric Sciences*, *34*(9), 1095–1105. https://doi.org/10.1007/s00376-017-6094-6

Lopez-Coto, I., Ren, X., Salmon, O. E., Karion, A., Shepson, P. B., Dickerson, R. R., et al. (2020). Wintertime CO2, CH4 and CO emissions estimation for the Washington DC/Baltimore metropolitan area using an inverse modeling technique. *Environmental Science & Technology*. https://doi.org/10.1021/acs.est.9b06619

Lu, X., Salovaara, J., & McElroy, M. B. (2012). Implications of the Recent Reductions in Natural Gas Prices for Emissions of CO2 from the US Power Sector. *Environmental Science & Technology*, *46*(5), 3014–3021. https://doi.org/10.1021/es203750k

Maasakkers, J. D., Jacob, D. J., Sulprizio, M. P., Scarpelli, T. R., Nesser, H., Sheng, J., et al. (2021). 2010--2015 North American methane emissions, sectoral contributions, and trends: a high-resolution inversion of GOSAT observations of atmospheric methane. *Atmospheric Chemistry and Physics*, *21*(6), 4339–4356. https://doi.org/10.5194/acp-21-4339-2021

Martin, C. R., Zeng, N., Karion, A., Dickerson, R. R., Ren, X., Turpie, B. N., & Weber, K. J. (2017). Evaluation and enhancement of a low-cost NDIR CO_2 sensor. *Atmos. Meas. Tech. Discuss.*, *2017*, 1–25. https://doi.org/10.5194/amt-2016-396

Martin, C. R., Zeng, N., Karion, A., Mueller, K., Ghosh, S., Lopez-Coto, I., et al. (2019). Investigating sources of variability and error in simulations of carbon dioxide in an urban region. *Atmospheric Environment*, *199*, 55–69. https://doi.org/10.1016/j.atmosenv.2018.11.013

Mays, K. L., Shepson, P. B., Stirm, B. H., Karion, A., Sweeney, C., & Gurney, K. R. (2009). Aircraft-Based Measurements of the Carbon Footprint of Indianapolis. *Environmental Science & Technology*, *43*(20), 7816–7823.

McDonald, B. C., McBride, Z. C., Martin, E. W., & Harley, R. A. (2014). High-resolution mapping of motor vehicle carbon dioxide emissions. *Journal of Geophysical Research: Atmospheres*, *119*(9), 5283–5298. https://doi.org/10.1002/2013JD021219

McDonald, B. C., McKeen, S. A., Cui, Y. Y., Ahmadov, R., Kim, S.-W., Frost, G. J., et al. (2018). Modeling Ozone in the Eastern U.S. using a Fuel-Based Mobile Source Emissions Inventory. *Environmental Science & Technology*, *52*(13), 7360–7370. https://doi.org/10.1021/acs.est.8b00778

McKain, K., Wofsy, S. C., Nehrkorn, T., Eluszkiewicz, J., Ehleringer, J. R., & Stephens, B. B. (2012). Assessment of ground-based atmospheric observations for verification of greenhouse gas emissions from an urban region. *Proceedings of the National Academy of Sciences of the United States of America*, *109*(22), 8423–8428. https://doi.org/10.1073/pnas.1116645109

McKain, K., Down, A., Raciti, S. M., Budney, J., Hutyra, L. R., Floerchinger, C., et al. (2015). Methane emissions from natural gas infrastructure and use in the urban region of Boston, Massachusetts. *Proceedings of the National Academy of Sciences of the United States of America*, *112*(7), 1941–1946. https://doi.org/DOI 10.1073/pnas.1416261112

MDE (Maryalnd Department of the Environment). (2021). The Greenhouse Gas Emissions Reduction Act: 2030 GGRA Plan. Retrieved April 2, 2021, from https://mde.maryland.gov/programs/Air/ClimateChange/Pages/Greenhouse-Gas-Emissions-Reduction-Act-(GGRA)-Plan.aspx

MDE (Maryland Department of the Environment). (2015). The Greenhouse Gas Emissions Reduction Act Plan Update 2015. Retrieved March 17, 2019, from https://mde.maryland.gov/programs/marylander/documents/mccc/publications/2015ggraplanupdate/climateupdate2015.pdf

MDE (Maryland Department of the Environment). (2016). Maryland 2014 Periodic GHG Emissions Inventory. Retrieved August 1, 2018, from https://mde.state.md.us/programs/Air/ClimateChange/Pages/GreenhouseGasInventory.aspx

MDE (Maryland Department of the Environment). (2017). MD 2017 Periodic GHG Emissions Inventory. Retrieved March 17, 2021, from https://mde.maryland.gov/programs/Air/ClimateChange/Pages/GreenhouseGasInventory.aspx

MDE (Maryland Department of the Environment). (2021). Linking Weather and Air Quality Using Radar.

MDOT (Maryland Department of Transportation), & MDE (Maryland Department of the Environment). (2016). Charting the Path Forward: A Transportation Strategy for Meeting Long-term Air Quality and Greenhouse Gas Emissions Goals and Enhancing Maryland's Economy and Quality of Life. Retrieved December 21, 2020, from https://mde.maryland.gov/programs/Air/MobileSources/SiteAssets/Pages/index/Charting the Path Forward - A Transportation Strategy for Meetin Long-term Air Quality and Green House Gas Emission Goals.pdf

MDOT (Maryland Department of Transportation) Data Services Division. Office of Planning and Preliminary Engineering. (2020). Weekly Changes at Permanent

Counters (ATR).
Memmott, J., & Young, P. (2008). Seasonal Variation in Traffic Congestion: A Study of Three U.S. Cities. *BTS Technical Report, U.S. Department of Transportation, Research and Innovative Technology Administration*, 5. Retrieved from https://www.bts.gov/sites/bts.dot.gov/files/legacy/publications/bts_technical_report/august_2008/pdf/entire.pdf
Merrin, Z., & Francisco, P. W. (2019). Unburned Methane Emissions from Residential Natural Gas Appliances. *Environmental Science & Technology*, *53*(9), 5473–5482. https://doi.org/10.1021/acs.est.8b05323
Michalak, A. M., Randazzo, N. A., & Chevallier, F. (2017). Diagnostic methods for atmospheric inversions of long-lived greenhouse gases. *Atmospheric Chemistry and Physics*, *17*(12), 7405–7421. https://doi.org/10.5194/acp-17-7405-2017
Miller, S M, Matross, D. M., Andrews, A. E., Millet, D. B., Longo, M., Gottlieb, E. W., et al. (2008). Sources of carbon monoxide and formaldehyde in North America determined from high-resolution atmospheric data. *Atmospheric Chemistry and Physics*, *8*(24), 7673–7696. https://doi.org/10.5194/acp-8-7673-2008
Miller, Scot M, & Michalak, A. M. (2017). Constraining sector-specific CO2 and CH4 emissions in the US. *Atmospheric Chemistry and Physics*, *17*(6), 3963–3985.
Mitchell, L. E., Crosman, E. T., Jacques, A. A., Fasoli, B., Leclair-Marzolf, L., Horel, J., et al. (2018). Monitoring of greenhouse gases and pollutants across an urban area using a light-rail public transit platform. *Atmospheric Environment*, *187*, 9–23.
Moran, D., Kanemoto, K., Jiborn, M., Wood, R., Többen, J., & Seto, K. C. (2018). Carbon footprints of 13 000 cities. *Environmental Research Letters*, *13*(6), 64041.
Mueller, K., Yadav, V., Lopez-Coto, I., Karion, A., Gourdji, S., Martin, C., & Whetstone, J. (2018). Siting background towers to characterize incoming air for urban greenhouse gas estimation: A case study in the Washington, DC/Baltimore area. *Journal of Geophysical Research: Atmospheres*, *123*(5), 2910–2926. https://doi.org/10.1002/2017JD027364
Nassar, R., Napier-Linton, L., Gurney, K. R., Andres, R. J., Oda, T., Vogel, F. R., & Deng, F. (2013). Improving the temporal and spatial distribution of CO_2 emissions from global fossil fuel emission data sets. *Journal of Geophysical Research: Atmospheres*, *118*(2), 917–933. https://doi.org/10.1029/2012JD018196
Nassar, R., Hill, T. G., McLinden, C. A., Wunch, D., Jones, D. B. A., & Crisp, D. (2017). Quantifying CO2 emissions from individual power plants from space. *Geophysical Research Letters*, *44*(19), 10–45.
NCSL (National Conference on State Legislatures). (2021). Greenhouse Gas Emissions Reduction Targets and Market-based Policies. Retrieved April 20, 2021, from https://www.ncsl.org/research/energy/greenhouse-gas-emissions-reduction-targets-and-market-based-policies.aspx
Newman, S., Xu, X. M., Gurney, K. R., Hsu, Y. K., Li, K. F., Jiang, X., et al. (2016). Toward consistency between trends in bottom-up CO_2 emissions and top-down

atmospheric measurements in the Los Angeles megacity. *Atmospheric Chemistry and Physics*, *16*(6), 3843–3863. https://doi.org/10.5194/acp-16-3843-2016

NGA (National Governors Association). (2020). Coronavirus State Actions. Retrieved December 15, 2020, from https://www.nga.org/coronavirus-state-actions-all/

Nice, R. (2015). ANSI and IEEE Standards for Metering. Retrieved January 15, 2021, from https://www.pjm.com/-/media/committees-groups/task-forces/mtf/20151113/20151113-item-08-ansi-and-ieee-standards.ashx

NOAA (National Oceanic and Atmospheric Administration). (2020a). High Resolution Rapid Refresh (HRRR) model, HRRR 3 km (pressure). Retrieved October 1, 2020, from https://www.ready.noaa.gov/READYmetdata.php

NOAA (National Oceanic and Atmospheric Administration). (2020b). THE NOAA Annual Greenhouse Gas Index (AGGI). Retrieved March 12, 2021, from https://www.esrl.noaa.gov/gmd/aggi/aggi.html

NOAA CPC (National Oceanic and Atmospheric Administration Climate Prediction Center). (2020). Degree Days Statistics, States and Cities, Daily Degree Days. Retrieved October 9, 2020, from https://www.cpc.ncep.noaa.gov/products/analysis_monitoring/cdus/degree_days/

O'Shaughnessy, E., Heeter, J., Keyser, D., Gagnon, P., & Aznar, A. (2016). Estimating the National Carbon Abatement Potential of City Policies : A Data-Driven Approach Estimating the National Carbon Abatement Potential of City Policies : A Data- Driven Approach. Retrieved February 15, 2021, from https://www.nrel.gov/docs/fy17osti/67101.pdf

O'Shea, S. J., Allen, G., Fleming, Z. L., Bauguitte, S. J. B., Percival, C. J., Gallagher, M. W., et al. (2014). Area fluxes of carbon dioxide, methane, and carbon monoxide derived from airborne measurements around Greater London: A case study during summer 2012. *Journal of Geophysical Research-Atmospheres*, *119*(8), 4940–4952. https://doi.org/10.1002/2013JD021269

Oda, T, & Maksyutov, S. (2011). A very high-resolution (1 km×1 km) global fossil fuel CO_2 emission inventory derived using a point source database and satellite observations of nighttime lights. *Atmos. Chem. Phys.*, *11*(2), 543–556. https://doi.org/10.5194/acp-11-543-2011

Oda, T, & Maksyutov, S. (2015). ODIAC fossil fuel CO_2 emissions dataset, Center for Global Environmental Research, National Institute for Environmental Studies. https://doi.org/10.17595/20170411.001 (Access date: 2019/03/27).

Oda, T, Maksyutov, S., & Andres, R. J. (2018). The open-source data inventory for anthropogenic CO_2, version 2016 (ODIAC2016): a global monthly fossil fuel CO_2 gridded emissions data product for tracer transport simulations and surface flux inversions. *Earth System Science Data*, *10*(1), 87–107. https://doi.org/10.5194/essd-10-87-2018

Oda, Tomohiro, & Maksyutov, S. (2020). ODIAC Fossil Fuel CO2 Emissions Dataset (Version ODIAC2020), Center for Global Environmental Research, National Institute for Environmental Studies. https://doi.org/10.17595/20170411.001

Oda, Tomohiro, Bun, R., Kinakh, V., Topylko, P., Halushchak, M., Marland, G., et al. (2019). Errors and uncertainties in a gridded carbon dioxide emissions inventory. *Mitigation and Adaptation Strategies for Global Change*, *24*(6),

1007–1050. https://doi.org/10.1007/s11027-019-09877-2
Parrish, D. D. (2006). Critical evaluation of US on-road vehicle emission inventories. *Atmospheric Environment*, *40*(13), 2288–2300. https://doi.org/https://doi.org/10.1016/j.atmosenv.2005.11.033
Patarasuk, R., Gurney, K. R., O'Keeffe, D., Song, Y., Huang, J., Rao, P., et al. (2016). Urban high-resolution fossil fuel CO_2 emissions quantification and exploration of emission drivers for potential policy applications. *Urban Ecosystems*, *19*(3), 1013–1039. https://doi.org/10.1007/s11252-016-0553-1
Peischl, J., Karion, A., Sweeney, C., Kort, E. A., Smith, M. L., Brandt, A. R., et al. (2016). Quantifying atmospheric methane emissions from oil and natural gas production in the Bakken shale region of North Dakota. *Journal of Geophysical Research-Atmospheres*, *121*(10), 6101–6111. https://doi.org/10.1002/2015JD024631
Peters, W., Jacobson, A. R., Sweeney, C., Andrews, A. E., Conway, T. J., Masarie, K., et al. (2007). An atmospheric perspective on North American carbon dioxide exchange: CarbonTracker. *Proceedings of the National Academy of Sciences*, *104*(48), 18925–18930. https://doi.org/10.1073/pnas.0708986104
Pisso, I., Patra, P., Takigawa, M., Machida, T., Matsueda, H., & Sawa, Y. (2019). Assessing Lagrangian inverse modelling of urban anthropogenic CO2 fluxes using in situ aircraft and ground-based measurements in the Tokyo area. *Carbon Balance and Management*, *14*(1), 6. https://doi.org/10.1186/s13021-019-0118-8
Pitt, J. R., Allen, G., Bauguitte, S. J.-B., Gallagher, M. W., Lee, J. D., Drysdale, W., et al. (2019). Assessing London \chem{CO_{2}}, \chem{CH_{4}} and CO emissions using aircraft measurements and dispersion modelling. *Atmospheric Chemistry and Physics*, *19*(13), 8931–8945. https://doi.org/10.5194/acp-19-8931-2019
Plant, G., Kort, E. A., Floerchinger, C., Gvakharia, A., Vimont, I., & Sweeney, C. (2019). Large fugitive methane emissions from urban centers along the US East Coast. *Geophysical Research Letters*, *46*(14), 8500–8507. https://doi.org/10.1029/2019GL082635
Prairie, Y. T., & Duarte, C. M. (2007). Direct and indirect metabolic CO_2 release by humanity. *Biogeosciences*, *4*(2), 215–217. https://doi.org/10.5194/bg-4-215-2007
Le Quéré, C., Jackson, R. B., Jones, M. W., Smith, A. J. P., Abernethy, S., Andrew, R. M., et al. (2020). Temporary reduction in daily global CO2 emissions during the COVID-19 forced confinement. *Nature Climate Change*, *10*(7), 647–653. https://doi.org/10.1038/s41558-020-0797-x
Quick, J. C., & Marland, E. (2019). Systematic error and uncertain carbon dioxide emissions from US power plants. *Journal of the Air & Waste Management Association*, 1–13. https://doi.org/10.1080/10962247.2019.1578702
Rayner, P. J., Raupach, M. R., Paget, M., Peylin, P., & Koffi, E. (2010). A new global gridded data set of CO_2 emissions from fossil fuel combustion: Methodology and evaluation. *Journal of Geophysical Research-Atmospheres*, *115*. https://doi.org/10.1029/2009jd013439
Ren, X., Salmon, O. E., Hansford, J. R., Ahn, D., Hall, D., Benish, S. E., et al. (2018). Methane Emissions From the Baltimore-Washington Area Based on Airborne

Observations: Comparison to Emissions Inventories. *Journal of Geophysical Research: Atmospheres*, *123*(16). https://doi.org/10.1029/2018JD028851

Ren, Xinrong, Hall, D. L., Vinciguerra, T., Benish, S. E., Stratton, P. R., Ahn, D., et al. (2019). Methane emissions from the Marcellus shale in southwestern Pennsylvania and northern west Virginia based on airborne measurements. *Journal of Geophysical Research: Atmospheres*. https://doi.org/10.1029/2018JD029690

Rudy, J., Cherti, M., Lewis, M., Leon, A., Carroll, C., & Kolpakov, I. (2020). py-earth. Retrieved January 30, 2021, from https://github.com/scikit-learn-contrib/py-earth

Ryoo, J.-M., Iraci, L. T., Tanaka, T., Marrero, J. E., Yates, E. L., Fung, I., et al. (2019). Quantification of CO 2 and CH 4 emissions over Sacramento, California, based on divergence theorem using aircraft measurements. *Atmospheric Measurement Techniques*, *12*(5), 2949–2966.

Salawitch, R. J., Canty, T. P., Hope, A. P., Tribett, W. R., & Bennett, B. F. (2017). *Paris climate agreement: Beacon of hope*. Springer International Publishing. https://doi.org/10.1007/978-3-319-46939-3

Salmon, O. E., Shepson, P. B., Ren, X., Collow, M., Allison, B., Miller, M. A., et al. (2017). Urban emissions of water vapor in winter. *Journal of Geophysical Research: Atmospheres*, *122*(17), 9467–9484. https://doi.org/10.1002/2016JD026074

Salmon, O. E., Shepson, P. B., Ren, X., He, H., Hall, D. L., Dickerson, R. R., et al. (2018). Top-down estimates of NO_x and CO emissions from Washington, DC-Baltimore during the WINTER campaign. *Journal of Geophysical Research: Atmospheres*. https://doi.org/10.1029/2018JD028539

Sargent, M., Barrera, Y., Nehrkorn, T., Hutyra, L. R., Gately, C. K., Jones, T., et al. (2018). Anthropogenic and biogenic CO_2 fluxes in the Boston urban region. *Proceedings of the National Academy of Sciences*, *115*(29), 7491–7496. https://doi.org/10.1073/pnas.1803715115

Schivley, G., Azevedo, I., & Samaras, C. (2018). Assessing the evolution of power sector carbon intensity in the United States. *Environmental Research Letters*, *13*(6), 64018. https://doi.org/10.1088/1748-9326/aabe9d

Schneising, O., Burrows, J. P., Dickerson, R. R., Buchwitz, M., Reuter, M., & Bovensmann, H. (2014). Remote sensing of fugitive methane emissions from oil and gas production in North American tight geologic formations. *Earths Future*, *2*(10), 548–558.

Siler-Evans, K., Azevedo, I. L., & Morgan, M. G. (2012). Marginal Emissions Factors for the U.S. Electricity System. *Environmental Science & Technology*, *46*(9), 4742–4748. https://doi.org/10.1021/es300145v

Slowik, P., & Lutsey, N. (2018). The continued transition to electric vehicles in U.S. cities. Retrieved May 1, 2021, from https://theicct.org/sites/default/files/publications/Transition_EV_US_Cities_20180724.pdf

Smith, I. A., Hutyra, L. R., Reinmann, A. B., Thompson, J. R., & Allen, D. W. (2019). Evidence for edge enhancements of soil respiration in temperate forests. *Geophysical Research Letters*, *46*(8), 4278–4287.

https://doi.org/10.1029/2019GL082459
Solazzo, E., Crippa, M., Guizzardi, D., Muntean, M., Choulga, M., & Janssens-Maenhout, G. (2021). Uncertainties in the Emissions Database for Global Atmospheric Research (EDGAR) emission inventory of greenhouse gases. *Atmospheric Chemistry and Physics*, *21*(7), 5655–5683. https://doi.org/10.5194/acp-21-5655-2021
Staufer, J., Broquet, G., Bréon, F.-M., Puygrenier, V., Chevallier, F., Xueref-Rémy, I., et al. (2016). The first 1-year-long estimate of the Paris region fossil fuel CO 2 emissions based on atmospheric inversion. *Atmospheric Chemistry and Physics*, *16*(22), 14703–14726.
Stein, A. F., Draxler, R. R., Rolph, G. D., Stunder, B. J. B., Cohen, M. D., & Ngan, F. (2015). NOAA's HYSPLIT atmospheric transport and dispersion modeling system. *Bulletin of the American Meteorological Society*, *96*(12), 2059–2077. https://doi.org/10.1175/BAMS-D-14-00110.1
Stocker, T. F., D. Qin, Plattner, G.-K., Tignor, M., Allen, S. K., Boschung, J., et al. (2013). IPCC, 2013: Climate Change 2013: The Physical Science Basis. Contribution of Working Group I to the Fifth Assessment Report of the Intergovernmental Panel on Climate Change. Retrieved November 28, 2018, from https://www.ipcc.ch/report/ar5/wg1/
Strong, C., Stwertka, C., Bowling, D. R., Stephens, B. B., & Ehleringer, J. R. (2011). Urban carbon dioxide cycles within the Salt Lake Valley: A multiple-box model validated by observations. *Journal of Geophysical Research: Atmospheres*, *116*(D15). https://doi.org/10.1029/2011JD015693
Takriti, S., Birge, J. R., & Long, E. (1996). A stochastic model for the unit commitment problem. *IEEE Transactions on Power Systems*, *11*(3), 1497–1508. https://doi.org/10.1109/59.535691
Tans, P., & Keeling, R. (2021). Mauna Loa CO2 annual mean data.
Trainer, M., Ridley, B. A., Buhr, M. P., Kok, G., Walega, J., Hubler, G., et al. (1995). Regional ozone and urban plumes in the southeastern United-States - Birmingham, a case-study. *Journal of Geophysical Research-Atmospheres*, *100*(D9), 18823–18834. https://doi.org/10.1029/95JD01641
Tribett, W. R., Salawitch, R. J., Hope, A. P., Canty, T. P., & Bennett, B. F. (2017). *Chapter 3 Paris INDCs, Paris Climate Agreement: Beacon of Hope* (1st ed.). Springer International Publishing. https://doi.org/10.1007/978-3-319-46939-3
Turnbull, J., Sweeney, C., Karion, A., Newberger, T., Lehman, S. J., Tans, P. P., et al. (2015). Toward quantification and source sector identification of fossil fuel CO_2 emissions from an urban area: Results from the INFLUX experiment. *Journal of Geophysical Research: Atmospheres*, *120*(1), 292–312. https://doi.org/10.1002/2014JD022555
Turnbull, J., Karion, A., Davis, K. J., Lauvaux, T., Miles, N. L., Richardson, S. J., et al. (2018). Synthesis of urban CO2 emission estimates from multiple methods from the Indianapolis Flux Project (INFLUX). *Environmental Science & Technology*, *53*(1), 287–295. https://doi.org/10.1021/acs.est.8b05552
Turnbull, J C, Karion, A., Fischer, M. L., Faloona, I., Guilderson, T., Lehman, S. J., et al. (2011). Assessment of fossil fuel carbon dioxide and other anthropogenic trace gas emissions from airborne measurements over Sacramento, California in

spring 2009. *Atmospheric Chemistry and Physics*, *11*(2), 705–721. https://doi.org/10.5194/acp-11-705-2011

Turnbull, Jocelyn C, Tans, P. P., Lehman, S. J., Baker, D., Conway, T. J., Chung, Y. S., et al. (2011). Atmospheric observations of carbon monoxide and fossil fuel CO2 emissions from East Asia. *Journal of Geophysical Research: Atmospheres*, *116*(D24). https://doi.org/https://doi.org/10.1029/2011JD016691

Turner, A J, Köhler, P., Magney, T. S., Frankenberg, C., Fung, I., & Cohen, R. C. (2020). A double peak in the seasonality of California's photosynthesis as observed from space. *Biogeosciences*, *17*(2), 405–422. https://doi.org/10.5194/bg-17-405-2020

Turner, Alexander J, Kim, J., Fitzmaurice, H., Newman, C., Worthington, K., Chan, K., et al. (2020). Observed Impacts of COVID-19 on Urban CO2 Emissions. *Geophysical Research Letters*, *47*(22), e2020GL090037. https://doi.org/https://doi.org/10.1029/2020GL090037

U.S. Office of Personnel Management. (2020). Pay & Leave: Federal Holidays. Retrieved July 10, 2020, from https://www.opm.gov/policy-data-oversight/pay-leave/federal-holidays/#url=Overview

UN-Habitat (United Nations Human Settlements Programme). (2011). *Cities and climate change: Global report on human settlements 2011* (illustrate). Earthscan. Retrieved from https://books.google.com/books?id=dzJhJny37h8C

UN (United Nations). (2017). Reference: C.N.464.2017.TREATIES-XXVII.7.d (Depositary Notification). Retrieved May 10, 2019, from https://treaties.un.org/doc/Publication/CN/2017/CN.464.2017-Eng.pdf

UN (United Nations) Department of Economic and Sociarl Affairs. (2018). World Urbanization Prospects: The 2018 Revision. Retrieved May 10, 2020, from https://population.un.org/wup/Publications/Files/WUP2018-Report.pdf

UNFCCC (United Nations Framework Convention on Climate Change). (2015). Paris Agreement. In Report of the Conference of the Parties to the United Nations Framework Convention on Climate Change (21st Session, 2015: Paris). Retrieved April 10, 2021, from https://unfccc.int/sites/default/files/english_paris_agreement.pdf

USEIA (US Energy Information Administration). (2016). Layer Information for Interactive State Maps: Power Plants. Retrieved March 1, 2016, from https://www.eia.gov/maps/layer_info-m.php

USEPA (U.S. Environmental Protection Agency). (2009). Plain English Guide to the Part 75 Rule. Retrieved May 10, 2019, from https://www.epa.gov/sites/production/files/2015-05/documents/plain_english_guide_to_the_part_75_rule.pdf

USEPA AMPD (U.S. Environmental Protection Agency). (2015). Air Markets Program Data (AMPD). Retrieved August 1, 2015, from https://ampd.epa.gov/ampd/

USEPA GHGRP (U.S. Environmental Protection Agency). (2019). Greenhouse Gas Reporting Program (GHGRP). Retrieved March 1, 2017, from https://www.epa.gov/ghgreporting

Viatte, C., Lauvaux, T., Hedelius, J. K., Parker, H., Chen, J., Jones, T., et al. (2017). Methane emissions from dairies in the Los Angeles Basin. *Atmospheric*

Chemistry and Physics, *17*(12), 7509–7528. https://doi.org/10.5194/acp-17-7509-2017

Whetstone, J. R. (2018). Advances in urban greenhouse gas flux quantification: The Indianapolis Flux Experiment (INFLUX). *Elem Sci Anth*, *6*(1). https://doi.org/10.1525/elementa.282

White, W. H., Patterson, D. E., & Wilson, W. E. (1983). Urban exports to the nonurban troposphere: Results from Project MISTT. *Journal of Geophysical Research: Oceans*. https://doi.org/10.1029/JC088iC15p10745

WHO (World Health Organization). (2020). COVID-19 Weekly Epidemiological Update, (November), 1;4. Retrieved from https://www.who.int/docs/default-source/coronaviruse/situation-reports/20201012-weekly-epi-update-9.pdf

Wong, C. K., Pongetti, T. J., Oda, T., Rao, P., Gurney, K. R., Newman, S., et al. (2016). Monthly trends of methane emissions in Los Angeles from 2011 to 2015 inferred by CLARS-FTS observations. *Atmospheric Chemistry and Physics*, *16*(20), 13121–13130. https://doi.org/10.5194/acp-16-13121-2016

Yu, Y., Wang, Y., Li, J., Fu, M., Shah, A. N., & He, C. (2021). A Novel Deep Learning Approach to Predict the Instantaneous NO_x Emissions From Diesel Engine. *IEEE Access*, *9*, 11002–11013. https://doi.org/10.1109/ACCESS.2021.3050165

Zeng, N., Qian, H., Munoz, E., & Iacono, R. (2004). How strong is carbon cycle-climate feedback under global warming? *Geophysical Research Letters*, *31*(20). https://doi.org/10.1029/2004GL020904

Zeng, N., Mariotti, A., & Wetzel, P. (2005). Terrestrial mechanisms of interannual CO_2 variability. *Global Biogeochemical Cycles*, *19*(1). https://doi.org/10.1029/2004GB002273

Zhang, R., Zhang, Y., Lin, H., Feng, X., Fu, T.-M., & Wang, Y. (2020). NOx Emission Reduction and Recovery during COVID-19 in East China. *Atmosphere*, *11*(4), 433. https://doi.org/10.3390/atmos11040433

Zhao, Y., Nielsen, C. P., Lei, Y., McElroy, M. B., & Hao, J. (2011). Quantifying the uncertainties of a bottom-up emission inventory of anthropogenic atmospheric pollutants in China. *Atmospheric Chemistry and Physics*, *11*(5), 2295–2308. https://doi.org/10.5194/acp-11-2295-2011